UNIVERSIDADE FEDERAL DE UBERLÂNDIA

Faculdade de Engenharia Mecânica

LUIZ GUSTAVO FREITAS PEREIRA

Numerical simulation of a non-reactive turbulent flow inside a cyclonic industrial boiler using LES and URANS

Uberlândia

2021

LUIZ GUSTAVO FREITAS PEREIRA

Numerical simulation of a non-reactive turbulent flow inside a cyclonic industrial boiler using LES and URANS

Dissertação apresentada ao Programa de Pós-graduação em Engenharia Mecânica da Universidade Federal de Uberlândia como parte dos requisitos exigidos para a obtenção do título de **MESTRE EM ENGENHARIA MECÂNICA**.

Área de concentração: Transferência de Calor e Mecânica dos Fluidos

Orientador: Prof. Dr. João Marcelo Vedovotto

Uberlândia

2021

Ficha Catalográfica Online do Sistema de Bibliotecas da UFU
com dados informados pelo(a) próprio(a) autor(a).

P436
2021

Pereira, Luiz Gustavo Freitas, 1995-
Numerical simulation of a non-reactive turbulent flow inside a cyclonic industrial boiler using LES and URANS [recurso eletrônico] / Luiz Gustavo Freitas Pereira. - 2021.

Orientador: João Marcelo Vedovotto.
Dissertação (Mestrado) - Universidade Federal de Uberlândia, Pós-graduação em Engenharia Mecânica.
Modo de acesso: Internet.
Disponível em: http://doi.org/10.14393/ufu.di.2021.444
Inclui bibliografia.
Inclui ilustrações.

1. Engenharia mecânica. I. Vedovotto, João Marcelo, 1981-, (Orient.). II. Universidade Federal de Uberlândia. Pós-graduação em Engenharia Mecânica. III. Título.

CDU: 621

Bibliotecários responsáveis pela estrutura de acordo com o AACR2:

Gizele Cristine Nunes do Couto - CRB6/2091

UNIVERSIDADE FEDERAL DE UBERLÂNDIA
Coordenação do Programa de Pós-Graduação em Engenharia Mecânica
Av. João Naves de Ávila, nº 2121, Bloco 1M, Sala 212 - Bairro Santa Mônica, Uberlândia-MG, CEP 38400-902
Telefone: (34) 3239-4282 - www.posgrad.mecanica.ufu.br - secposmec@mecanica.ufu.br

ATA DE DEFESA - PÓS-GRADUAÇÃO

Programa de Pós-Graduação em:	Engenharia Mecânica				
Defesa de:	Dissertação de Mestrado Acadêmico, nº 594, COPEM				
Data:	06/08/2021	Hora de início:	09:30	Hora de encerramento:	12:00
Matrícula do Discente:	11912EMC015				
Nome do Discente:	Luiz Gustavo Freitas Pereira				
Título do Trabalho:	Numerical simulation of a non-reactive turbulent flow inside a cyclonic industrial boiler using LES and URANS				
Área de concentração:	Transferência de Calor e Mecânica dos Fluidos				
Linha de pesquisa:	Dinâmica dos Fluidos e Transferência de Calor				
Projeto de Pesquisa de vinculação:					

Reuniu-se por meio de webconferência a Banca Examinadora, designada pelo Colegiado do Programa de Pós-graduação em Engenharia Mecânica, assim composta: Professores Doutores: Francisco José de Souza- FEMEC/UFU; Henry França Meier - FURB; Ricardo Serfaty - PETROBRAS e João Marcelo Vedovotto - FEMEC/UFU , orientador do candidato. Ressalta-se que os Prof. Francisco José de Souza, João Marcelo Vedovotto e o Discente participaram da defesa por meio de webconferência desde a cidade de Uberlândia/MG, Prof. Henry França Meier desde a cidade de Blumenau/SC, Dr. Ricardo Serfaty desde a cidade de Rio de Janeiro/RJ, em atendimento a Portaria nº 36, de 19 de março de 2020, da Coordenação de Aperfeiçoamento de Pessoal de Nível Superior - CAPES.

Iniciando os trabalhos o presidente da mesa, Dr. João Marcelo Vedovotto, apresentou a Comissão Examinadora e o candidato, agradeceu a presença do público, e concedeu ao Discente a palavra para a exposição do seu trabalho. A duração da apresentação do Discente e o tempo de arguição e resposta foram conforme as normas do Programa.

A seguir o senhor(a) presidente concedeu a palavra, pela ordem sucessivamente, aos(às) examinadores(as), que passaram a arguir o(a) candidato(a). Ultimada a arguição, que se desenvolveu dentro dos termos regimentais, a Banca, em sessão secreta, atribuiu o resultado final, considerando o(a) candidato(a):

Aprovado.

Esta defesa faz parte dos requisitos necessários à obtenção do título de Mestre.

O competente diploma será expedido após cumprimento dos demais requisitos, conforme as normas do Programa, a legislação pertinente e a regulamentação interna da UFU.

Nada mais havendo a tratar foram encerrados os trabalhos. Foi lavrada a presente ata que após lida e achada conforme foi assinada pela Banca Examinadora.

Documento assinado eletronicamente por **João Marcelo Vedovotto**, **Professor(a) do Magistério Superior**, em 06/08/2021, às 12:05, conforme horário oficial de Brasília, com fundamento no art. 6º, § 1º, do Decreto nº 8.539, de 8 de outubro de 2015.

Documento assinado eletronicamente por **Francisco José de Souza**, **Professor(a) do Magistério Superior**, em 06/08/2021, às 12:06, conforme horário oficial de Brasília, com fundamento no art. 6º, § 1º, do Decreto nº 8.539, de 8 de outubro de 2015.

Documento assinado eletronicamente por **ricardo serfaty**, **Usuário Externo**, em 06/08/2021, às 12:11, conforme horário oficial de Brasília, com fundamento no art. 6º, § 1º, do Decreto nº 8.539, de 8 de outubro de 2015.

Documento assinado eletronicamente por **Henry França Meier**, **Usuário Externo**, em 10/08/2021, às 12:38, conforme horário oficial de Brasília, com fundamento no art. 6º, § 1º, do Decreto nº 8.539, de 8 de outubro de 2015.

A autenticidade deste documento pode ser conferida no site https://www.sei.ufu.br/sei/controlador_externo.php?acao=documento_conferir&id_orgao_acesso_externo=0, informando o código verificador **2938842** e o código CRC **B4A5E525**.

À minha família, pela confiança e incentivo.

Agradecimentos

Agradeço e presto homenagem, inicialmente, ao meu avô que foi um dos homens mais inteligentes, disciplinados e engenhosos com quem tive o privilégio de conviver. Foi ele o grande responsável por despertar o meu interesse pela ciência e pela física, além de ter me incentivado a buscar cada vez mais conhecimento.

Agradeço à minha mãe, Shirley, pelo carinho e por ser o meu grande alicerce e incentivadora em minha jornada em busca de desenvolvimento profissional e, principalmente, felicidade. Também agradeço ao meu irmão, Gabriel, por todos os momentos de descontração e tentativas de explicação de meu trabalho em casa durante a pandemia. Agradeço à minha namorada, Thaís, pelo seu amor, cumplicidade e por ter sido tão incentivadora e paciente, sempre com pensamentos positivos e interessada em meu trabalho.

Agradeço, com profunda admiração, ao Gabriel, doutorando do MFLab e grande amigo, que foi um dos responsáveis pela concretização deste trabalho por meio de suas ideias e ajudas, sempre disposto a me aconselhar com paciência, clareza e profissionalismo.

Agradeço ao meu orientador, Prof. Dr. João Marcelo Vedovotto, pelos ensimentos, conselhos e acolhimento ao laboratório MFLab. Agradeço também ao Prof. Dr. Aristeu da Silveira Neto, por sua disponibilidade a sanar dúvidas relacionadas à Mecânica dos Fluidos.

Agradeço a todos os meus amigos do MFLab que contribuíram direta e indiretamente para a concretização desta pesquisa. Em especial, ao Kaissar, pelo incentivo a estudar simulação computacional e companheirismo e ao Gustavo e Valdson, por todos os conselhos relacionados a CFD, ao código e aos momentos de descontração e amizade.

Por fim, agradeço à Coordenação de Aperfeiçoamento de Pessoal de Nível Superior

(CAPES) pelo suporte financeiro e à Faculdade de Engenharia Mecânica da Universidade Federal de Uberlândia (professores, técnicos e colaboradores), pela assistência e material de estudo fornecido.

"One, remember to look up at the stars and not down at your feet. Two, never give up work. Work gives you meaning and purpose and life is empty without it. Three, if you are lucky enough to find love, remember it is there and don't throw it away."

Stephen Hawking

Abstract

A numerical simulation of a non-reactive turbulent flow inside a cyclonic industrial CO boiler was investigated in order to understand the swirling formation, the fluid behavior in different locations inside the domain and the distribution of chemical species. As 80% of the energy matrix in Brazil is generated by combustion processes and government regulations about NOx emissions are becoming more restrict, enhancing combustion efficiency in a CO boiler with a turbulent swirling flow to reduce pollutant emissions has become an engineering research topic. Enhancing mixing processes through turbulent swirling flows might reduce thermal NOx formation. Computational fluid dynamics simulations were realized using the in-house MFSim code with the turbulent closure models LES, URANS Standard $k - \varepsilon$, URANS Standard $k - \varepsilon$ Modified and URANS Realizable $k - \varepsilon$. A theoretical basis about turbulence, LES and URANS closure models, mixing and swirling flows was provided. A state of art comprising different authors pointed out that some works with URANS Standard $k - \varepsilon$ demonstrated a premature solid-body rotation formation due to its eddy viscosity assumption and that swirling flows may reduce pollutant emissions by improving mixing of reactants and decreasing flame temperature. Validations concerning multi-component mixing flows and Immersed Boundary method were presented. From the results, LES and URANS Standard $k - \varepsilon$ presented similar velocity field results, capable of capturing the swirling formation. When analyzing three URANS closure models, a turbulent kinetic energy graph illustrated that it is relevant to observe the modeled part and the value obtained from velocity field fluctuations. The modified model presented low turbulent viscosity values and an LES-like behavior, with similar results to the standard model. The realizable model presented distant results comparing to the other models studied and there was no reverse flow in its swirling core. Adding different chemical species did not modify the velocity field and the highest mixing level was obtained in the most intense turbulent swirling region, close to the inlets. The data provided may assist in the comprehension of swirling formation, mixture processes inside a boiler and temperature control to reduce pollutant emissions.

Keywords: CFD. Turbulence. Swirling flow. URANS. LES. NOx emissions

Resumo

Uma simulação numérica de um escoamento turbulento não reativo em uma caldeira industrial ciclônica de CO foi investigada a fim de se compreender a formação de um escoamento rotativo, o comportamento do fluido em diferentes locais dentro do domínio e a distribuição de espécies químicas. Como 80% da matriz energética no Brasil é gerada por processos de combustão e as regulamentações governamentais sobre as emissões de NOx estão se tornando mais restritas, o aumento da eficiência da combustão em uma caldeira de CO com escoamento turbulento ciclônico para reduzir as emissões de poluentes tornou-se um tema de pesquisa de engenharia. Melhorar os processos de mistura por meio de escoamentos turbulentos rotativos pode reduzir a formação térmica de NOx. Simulações de dinâmica dos fluidos computacional foram realizadas usando o código MFSim com os modelos de fechamento turbulento LES, URANS Standard $k-\varepsilon$, URANS Standard $k-\varepsilon$ Modificado e URANS Realizable $k-\varepsilon$. Foi fornecida uma base teórica sobre turbulência, modelos de fechamento LES e URANS, escoamentos com mistura e escoamentos rotativos. Um estado da arte compreendendo diferentes autores apontou que alguns trabalhos com URANS Standard $k-\varepsilon$ demonstraram uma formação de rotação de corpo sólido prematura devido à sua suposição de viscosidade turbulenta e que escoamentos rotativos podem reduzir as emissões de poluentes, melhorando a mistura de reagentes e diminuindo a temperatura da chama. Foram apresentadas as validações relativas aos escoamentos com mistura de multicomponentes e ao método da Fronteira Imersa. Dos resultados, LES e URANS Standard $k-\varepsilon$ apresentaram campos de velocidade semelhantes, capazes de capturar a formação de escoamento rotativo. Ao analisar três modelos de fechamento URANS, um gráfico de energia cinética turbulenta ilustrou que é relevante observar a parte modelada e o valor obtido a partir das flutuações do campo de velocidade. O modelo modificado apresentou baixos valores de viscosidade turbulenta e comportamento semelhante a LES, com resultados similares ao modelo Standard. O modelo realizável apresentou resultados distantes em comparação com os outros modelos estudados e não houve escoamento reverso em seu núcleo giratório. A adição de diferentes espécies químicas não modificou o campo de velocidade e o maior nível de mistura foi obtido na região de turbulência mais intensa, próxima às entradas. Os dados fornecidos podem

auxiliar na compreensão da formação de escoamento rotativo, processos de mistura dentro de uma caldeira e controle de temperatura para reduzir as emissões de poluentes.

Keywords: CFD. Turbulência. Escoamento rotativo. URANS. LES. Emissões de NOx

Résumé

Une simulation numérique d'un écoulement turbulent non réactif à l'intérieur d'une chaudière cyclonique industrielle au CO a été étudiée afin de comprendre la formation tournante, le comportement des fluides à différents endroits à l'intérieur du domaine et la distribution des espèces chimiques. Comme 80% de la matrice énergétique au Brésil est générée par des processus de combustion et que les réglementations gouvernementales sur les émissions de NOx sont de plus en plus restrictives, l'amélioration de l'efficacité de la combustion dans une chaudière au CO avec un écoulement tournant turbulent pour réduire les émissions de polluants est devenue une sujet de recherche en ingénierie. L'amélioration des processus de mélange par des écoulements tournants turbulents pourrait réduire la formation de NOx thermique. Des simulations de dynamique des fluides informatiques ont été réalisées en utilisant le code MFSim avec les modèles de fermeture de turbulence LES, URANS Standard $k - \varepsilon$, URANS Standard $k - \varepsilon$ Modified et URANS Realizable $k - \varepsilon$. Une base théorique sur la turbulence, les modèles de fermeture LES et URANS, le mélange et les écoulements tournants a été fournie. Un état de l'art comprenant différents auteurs a souligné que certains travaux avec URANS Standard $k - \varepsilon$ ont démontré une formation prématurée de rotation de corps solide en raison de son hypothèse de viscosité turbulente et que les écoulements tournants peuvent réduire les émissions de polluants en améliorant le mélange des réactifs et en diminuant la température de la flamme. Des validations concernant les flux de mélange multi-composants et la méthode de la frontière immergée ont été présentées. D'après les résultats, LES et URANS Standard $k - \varepsilon$ ont présenté des résultats de champ de vitesse similaires, capables de capturer la formation tourbillonnante. Lors de l'analyse des trois modèles de fermeture URANS, un graphique d'énergie cinétique turbulente a montré qu'il est pertinent d'observer la partie modélisée et la valeur obtenue à partir des fluctuations du champ de vitesse. Le modèle modifié présentait de faibles valeurs de viscosité turbulente et un comportement de type LES, avec des résultats similaires à ceux du modèle standard. Le modèle réalisable a présenté des résultats éloignés par rapport aux autres modèles étudiés et il n'y avait pas d'écoulement inversé dans son noyau tournant. L'ajout de différentes espèces chimiques n'a pas modifié le champ de vitesse et le niveau de mélange le plus élevé a été

obtenu dans la région tournante turbulente la plus intense, à proximité des entrées. Les données fournies peuvent aider à la compréhension de la formation tourbillonnante, aux processus de mélange à l'intérieur d'une chaudière et au contrôle de la température pour réduire les émissions de polluants.

Mots-clés : CFD. Turbulence. Ecoulement tournant. URANS. LES. Emissions de NOx

List of Figures

List of Tables

List of abbreviations and acronyms

CDS	Central Differencing Scheme
CFD	Computational Fuid Dynamics
CFL	Courant-Friedrichs-Lewy
CUBISTA	Convergent and Universally Bounded Interpolation Scheme for the Treatment of Advection
DES	Detached-Eddy Simulation
DDES	Delayed Detached-Eddy Simulation
DNS	Direct Numerical Simulations
FCC	Fluid Catalytic Cracking
FCCU	Fluid Catalytic Cracking Unit
FOU	First Order Upwind
IMEX	IMplicit EXplicit
LES	Large Eddy Simulations
LPG	Liquefied Petroleum Gas
MFLab	Fluid Mechanics Laboratory
NDF	Number of Degrees of Freedom

RANS	Reynolds Averaged Navier-Stokes
Re	Reynolds number
RNG	Re-normalization group
SA	Spallart-Allmaras
SAS	Scale-Adaptive Simulation
SBDF	Semi-implicit Backward Differentiation Formula
Sc	Schmidt number
SGS	Subgrid Scale
SOU	Second Order Upwind
SST	Shear Stress Transport
UV	Ultraviolet

List of symbols

Operators

$\cdot$	Scalar product
$\int_\Omega$	Volume integral
$\int_S$	Surface integral
$\int_{S_k}$	Surface of a control volume integral
∇	Gradient
$\nabla\cdot$	Divergent
d	Derivative
∂	Partial derivative

Underscripts

P	Center of a finite volume
E	Center of the East face of a finite volume
e	Center of the east surface of a finite volume

w	Center of the west surface of a finite volume
n	Center of the north surface of a finite volume
s	Center of the south surface of a finite volume
t	Center of the top surface of a finite volume
b	Center of the bottom surface of a finite volume
U	Upstream cell
U	Downstream cell
f	Face of a cell
i	Index
Δt	Temporal difference
c_{avg}	Cumulative average

Superscripts

$n+1$	Actual time
n	A previous time step
$n-1$	Two previous time steps

Greek letters

$\dot{\omega}_k$	Reaction rate for species k

α_i	Parameters for temporal term in IMEX method
β_i	Parameters for temporal term in IMEX method
δ_{ij}	Kronecker delta
ε	Turbulence dissipation rate
μ	Dynamic viscosity
ν	Kinematic viscosity
ν_t	Turbulent kinematic viscosity
ρ	Density
τ_{ij}	Viscous stress tensor
$\underline{\underline{\tau}}$	Viscous stress tensor
ϕ	Transported variable
$\hat{\phi}$	Normalized transported variable
λ	Linear interpolation factor
ξ	Normalized coordinate
γ	Constant in SBDF method
Γ	Lagrangian domain
Ω	Eulerian domain
δ_x	Eulerian element dimension
ρ_0	Coflow density
ρ_1	Main jet density
μ_0	Coflow viscosity

μ_1	Main jet viscosity
τ_η	Kolmogorov time scale
η	Kolmogorov length scale
ω	Specific rate of dissipation
θ	Scalar concentration
ω_K	Kolmogorov frequency scale
Ω_{ij}	Rotation rate tensor
Δ	Spatial filter length scale

Latin letters

$\vec{b}$	Force field vector
$\vec{n}$	Vector normal to the surface where the fluid enters/exits
$\vec{V}$	Velocity vector
$\bar{u'}$	Fluctuation component of the filtered velocity vector in x-direction
$\bar{u}$	Component of the filtered velocity vector in x-direction
$\underline{\underline{I}}$	Unitary tensor
$\underline{\underline{T}}$	Total stress tensor
D_k	Diffusivity of species k in mixture
k	Turbulence kinetic energy
k^*	Estimated turbulent kinetic energy

L_{ij}	Leonard tensor
C_{ij}	Crossed tensor
m	Mass
p	Pressure
S_{ij}	Strain rate tensor
t	Time
m_k	Mass of species k
Y_k	Mass fraction of species k
V_k	Diffusion velocity of species k
D_k	Diffusion coefficient of species k
Sc_{kt}	Turbulent Schmidt number of species k
f	Component of a flux vector in the normal direction to the face of a control volume
f_k	Information at the center of a control volume surface
S_k	Area of a control volume surface
q	Product fo the field force and density
u	Component of velocity vector in x-direction
v	Component of velocity vector in y-direction
w	Component of velocity vector in z-direction
C	Courant-Friedrichs-Lewy condition
t_{adv}	Advective time

c	Constant in SBDF method
$\tilde{u}$	Favre's averaged velocity field in x-direction
$\tilde{u_k}$	Favre's averaged velocity field in x-direction for species k
$\tilde{u_k''}$	Favre's averaged velocity field fluctuation in x-direction for species k
$\tilde{Y_k}$	Favre's averaged mass fraction for species k
$\tilde{Y_k''}$	Favre's averaged mass fraction fluctuation for species k
u^*	Estimated velocity field
$\vec{x}$	Position of any point in eulerian mesh
$\vec{X}$	Position of any point in Lagrangian mesh
F_i	Force in Lagrangian points
U_i	Velocity field in Lagrangian points
RHS	Right Hand Side of Navier-Stokes equation
f_i	Force in eulerian mesh cells
U_i^*	Estimated velocity field in Lagrangian mesh elements
D_h	Interpolation function
D	Diameter
r_0	Nozzle jet radius
v_0	Coflow velocity
v_1	Main jet velocity
z	Mixture fraction
s	Mass stoichiometric ratio

Y_F	Fuel mass fraction
Y_F^0	Initial value of fuel mass fraction
Y_O	Oxygen mass fraction
Y_O^0	Initial value of oxygen mass fraction
C_D	Drag coefficient
A	Area
$\dot{m}$	Mass flow rate
v_{ar}	Velocity of airflow
v_{CO}	Velocity of CO gas
K	Wave number
u_ν	Kolmogorov velocity scale
$\mathcal{D}$	Molecular diffusion coefficient
S	Swirl number
W	Tangential velocity
a_{ij}	Reynolds stress anisotropy tensor
$u_i u_j$	Reynolds stress tensor
$u_i' u_j'$	Boussinesq-Reynolds tensor
$\overline{u_i' u_j'}$	Boussinesq-Reynolds sub-mesh tensor
$\bar{a}_{ij}$	Normalized anisotropy
u_r, u_θ, u_z	Radial, tangential and axial velocity components
f_i	Force term in Navier-Stokes equation

l_I	Integral length scale of turbulence
f_c	Cutoff frequency
k_c	Cutoff wave number
k_{sgs}	Sub-grid characteristic velocity scale

Contents

Chapter 1

INTRODUCTION

Innovation, infrastructure enhancement, and the creation of new technologies are related to the role of Engineering, as it uses scientific and technical knowledge to bring solutions to society.

Concerning Mechanical Engineering, especially in the Fluid Mechanics field, it consists of the study of the behavior and flow properties involving gases and/or liquids. Phenomena related to fluid flows can be very complex, depending on the fluid properties, the Reynolds number, the geometrical obstacles within the flow, the presence of structures that may interact with the fluid, or even some chemical reactions that could happen when involving combustion, for example.

Theoretical analysis, only, still cannot describe these phenomena in a proper and detailed way, especially those flows encountered in engineering applications. For this reason, experimental methods are used, sometimes as the only available tool for reaching a certain level of detail in a flow. Since the advent of the digital computer, a new alternative to analyze fluid movement has arisen: numerical simulation. This area of knowledge, which complements the theoretical analysis and experimental techniques, is called Computational Fluid Dynamics (CFD). With CFD, it is possible to test various operation conditions, different values for the variables of interest and explore different modifications of industrial systems. The auxiliary of a virtual experiment might save money and time in the industry for a certain application, as no change in industrial systems is needed.

Even though CFD is a new area of study, it is being developed and expanded by researchers in some areas like medicine, meteorology, aeronautical, civil and mechanical engineering, among others.

In a great part of industrial applications, the flows are considered turbulent. This characteristic might be beneficial and interesting when looking for an improved mixing process or it is inevitable, due to aspects related to the fluid velocity, its physical properties, and geometries in the domain where the fluid flows. The concern of multi-component turbulent flows is centered in the mixing process of the substances involved, especially for combustion purpose. The basis of a turbulent combustion simulation is to understand the interaction between turbulence and chemical reactions.

The union between combustion and turbulence can be easily found in industrial systems. Considering that almost 80% of the energy matrix in Brazil is generated by processes involving combustion, figure (1.1) (MME, 2020), this represents a motivation for scientific research to achieve greater efficiency for combustion processes and, therefore, guarantee a lower emission of pollutants.

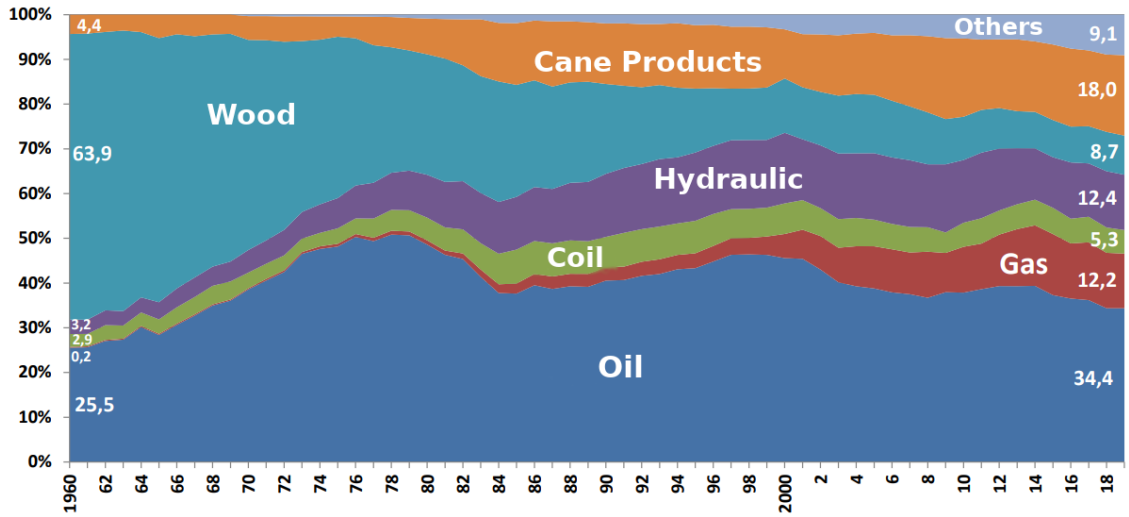

Figure 1.1 – Evolution of the Structure of the Internal Energy Supply Matrix (%). Source: (MME, 2020).

The study of these turbulent phenomena is divided into three main methodologies: the Large Eddy Simulations (LES), the Reynolds Averaged Navier-Stokes (RANS), and the Direct Numerical Simulations (DNS). In terms of the prediction of turbulent flows characteristics, the

first one is located between RANS, in which all turbulence scales are modeled, and DNS, in which all turbulence scales are resolved numerically.

In LES, the largest eddy structures, which carry the greatest amount of energy, are calculated numerically. The sub-mesh scales, in turn, as well as their interaction with the large scales, are modeled. The largest scales, responsible for the behavior and statistical properties of turbulent flows, tend to be dependent on the geometry of the problem, while the smallest structures are more universal and, consequently, easier to model. On the other hand, RANS methodology is capable of simulating a flow with a more elevated Reynolds number and a coarser mesh refinement, which is interesting for the industry when computational time and cost are relevant parameters.

The attainment of homogeneity at the molecular level is the ultimate measure of the effectiveness of mixing. Chemical reaction, which is essentially a molecular level process, can only occur where the fluids are molecularly mixed (MURTHY, 2013).

Concerning non-reactive turbulent mixing flows, a usual study application would be unsteady jets with density variations, which are found to be fundamental in applications in combustion systems. To control the ignition of fuel/air mixtures besides the chemical interaction, the knowledge of the mixing process and the mixture fractions are important prerequisites. The advantage of numerical simulations is to provide the opportunity for detailed studies on mixing and interaction problems. However, depending on the turbulence models applied, the results may be yielded different (LINDNER; MARKUS; MODEL, 2010).

For turbulent swirling flows, as cyclone separators or combustion burners, streamline curvature still poses a challenge for turbulence models, as strong anisotropy of the turbulence field is present, which cannot be captured by all turbulence models. Currently, most industrial flow simulations are based on two-equation turbulence models, like the widely known $k - \varepsilon$ model. However, it presents some deficiencies as a result of the eddy-viscosity assumption, which is the inaccurate or erroneous calculus of streamline curvature, system rotation and stagnation points, among others (GROTJANS, 1999). A possible remedy would be the use of Reynolds Stress Models (RSM) or even a $k - \varepsilon$ model with curvature correction.

Therefore, taking into account the importance of result predictions by virtual means in industry and the necessity for optimized turbulent mixing swirling flows using diverse turbulence methodologies, the motivations of this work are justified in the next section.

1.1 Motivation

The combustion process, a phenomenon of breaking chemical bonds with the release of thermal energy, used in different sectors of society, is necessary for social, technological, and economic development. In Brazil, almost 80% of the energy supply is converted using combustion processes, 2/3 of which are from fossil fuels and 1/3, from renewable sources. From this total, 40% is used in industry and 30% in transportation. Therefore, combustion is present in industrial sectors relevant to the economy and infrastructure, which demand a large amount of energy, such as the chemical and petrochemical sectors of iron, steel, cement, metals, and food (TURNS et al., 1996).

The study of combustion allows the engineer to help increasing efficiency in systems and processes and the design and construction of more sustainable equipment, aiming at the protection of the environment and human health. Besides, it is an intellectually stimulating study, as it involves several disciplines, such as the study of chemical reactions, flows, energy and mass transfer, computational simulation, materials, the environment, among others.

Despite the benefits provided by combustion, there is a disadvantage of the environmental pollution associated with it. The main pollutants generated in combustion processes are partially burned/unburned hydrocarbons, nitrogen oxides (NO and NO_2), carbon monoxide (CO), sulfur oxides (SO_2 and SO_3), and particulates. The consequences of pollution derived from the emission of these pollutants involve health problems, acid rain, global warming, ozone layer reduction, among others (TURNS et al., 1996).

In hydrocarbon processing industries, a Fluid Catalytic Cracking Unit, figure (1.2), produces gases rich in carbon monoxide. For the removal of energy from these gases and the consequent reduction of their emissions, a boiler is used to burn residual CO from catalytic cracking processes for steam generation and energy.

The Fluid Catalytic Cracking (FCC) has as the main characteristic the conversion of heavy fractions of oil into more noble products and, consequently, with greater added value (NÓBREGA, 2014).

A typical example of cracking in the oil refining industry is the production of gasoline (iso-octane) and LPG (cooking gas) (propane + butane) from catalytic cracking of gasoils.

Carbon monoxide (CO) is a product of incomplete combustion that occurs in the regenerator of the Fluid Catalytic Cracking Unit. Its emissions are controlled for environmental and regulation reasons. CO boilers are added to FCC units to recover the available energy from CO oxidation, using carbon monoxide as fuel gas. CO reacts to form CO_2 and releases a large amount of heat. The high-temperature flue gas is used to produce superheated steam, which can be used in other refinery equipment (YEH; LIANG, 2013).

One of the problems with the use of CO boilers is the emission of NO_x pollutants, which are generally formed by oxidation of N_2 and nitride in fuels, which can result in acid rain, cause damage to the atmospheric ozone layer, form ozone and smog, harmful to the respiratory system (ANDRADE, 2009). Besides, NO_x has been recognized as one of the main causes of excessive concentration of peroxide N_2O_4 in the atmosphere, which is considered toxic and corrosive, formed by the spontaneous reaction between nitrogen monoxide and oxygen (YEH; LIANG, 2013).

Nitrates formed in the atmosphere from NO_x compounds are captured as small particles or as acid dissolved in the rain. The nitrates deposited in the soil can affect its pH and the absorption of nutrients. Those that reach water surfaces, such as rivers and lakes, increase the nitrogen content of the water, which causes a nitrification process and the consequent growth of algae and other organisms capable of affecting aquatic life. Also, compounds related to NO_x emissions, such as N_2O, can reach the stratosphere, where they take part in chemical reactions that result in depletion of the stratospheric ozone layer, responsible for minimizing the penetration of UV rays on Earth's surface (RICHARDS, 2000).

Due to society's awareness of the climate changes caused by the emission of polluting gases into the atmosphere, governments have regulated the level of permitted emissions, with

their gradual tendency of reduction.

In a CO boiler, theoretically, as a fuel with nitrogen in its molecular structure is not used, the formation of NO_x occurs through the thermal process. In this mechanism, NO_x is formed by the reaction of nitrogen and oxygen and, although the oxygen concentration and its residence time influence the thermal formation of NO_x, the temperature is the most relevant parameter for this process.

According to Richards (2000), the thermal formation of NO_x has its peak between 1900 °C and 2000 °C and, as this is the temperature range in which combustion stationary mechanisms operate, it is understandable that the thermal formation of NO_x is the main mechanism of its formation. The main factors that affect the amount of NO_x formed by the thermal process are the flame temperature, the residence time of the flue gas on the peak of the flame temperature range and, in a slightly lesser extent, the amount of oxygen present on the peak zone of the flame temperature (RICHARDS, 2000).

Thus, to maximize the conversion rate of reagents to products during combustion and, consequently, to reduce the formation of NO_x, turbulent mixing flows within the CO boiler are used, which justifies the computational study of this technique for a better understanding of the phenomenon and how it can help to improve the energy efficiency of the equipment and in reducing the emission of pollutant gases.

In this aspect, the study of computational fluid dynamics is relevant in the industrial field, since it allows a detailed understanding of fluid dynamics inside a burner and the possibility of improvements without having a relevant time and high cost that would be spent for a detailed experimental analysis with modifications or other equipment for testing. Thus, it is necessary to understand the behavior of cyclonic mixing turbulent flow, as well as the turbulence closure models that best describe the problem.

Combustion requires that the fuel and the oxidizer be mixed at the molecular level. The consensus is that after a range of vortex of different sizes develops, the stress and shear at the interface between the eddies improve the mixture. During the breaking process of turbulent structures and the reduced dimensions vortex formation, the stress and shear increase and, thus,

the concentration gradients at the interface between the reagents are amplified, which, in turn, increases their molecular diffusion. The molecular mixture of fuel and oxidizer, as a prerequisite for combustion, occurs, therefore, at the interface between small vortex and is favored by a turbulent flow regime (PETERS, 2010).

The formation of certain pollutants, such as NO_x and soot, is hampered when working temperatures are sufficiently low due to significant dilution, which can be achieved with the use of a cyclonic turbulent flow (SORRENTINO et al., 2017).

Thus, due to the turbulent flow intensity during combustion, there is a better mixture between the gases and the decay of the peak temperature in the combustion zone. In addition, the residence time of gases in high-temperature areas is reduced, which decreases the rate of formation of NO species.

Lima, Nogueira and Guerra (2017) investigated the computational modeling of a horizontal cyclone combustion chamber for burning biomass. The main mechanism of formation of NO_x identified was the thermal and its formation is directly related to the increase in the residence time of the gases produced by combustion at high temperatures.

Therefore, the motivation of this work is to provide knowledge and data of a turbulent mixing nonreactive swirling flow inside an industrial combustion burner to guide future combustion researches about the flow behavior inside these systems. Thus, understanding the fluid dynamics, the mixing processes, and, in future researches, combustion processes, combustion burners may be optimized to reduce the NOx production rate.

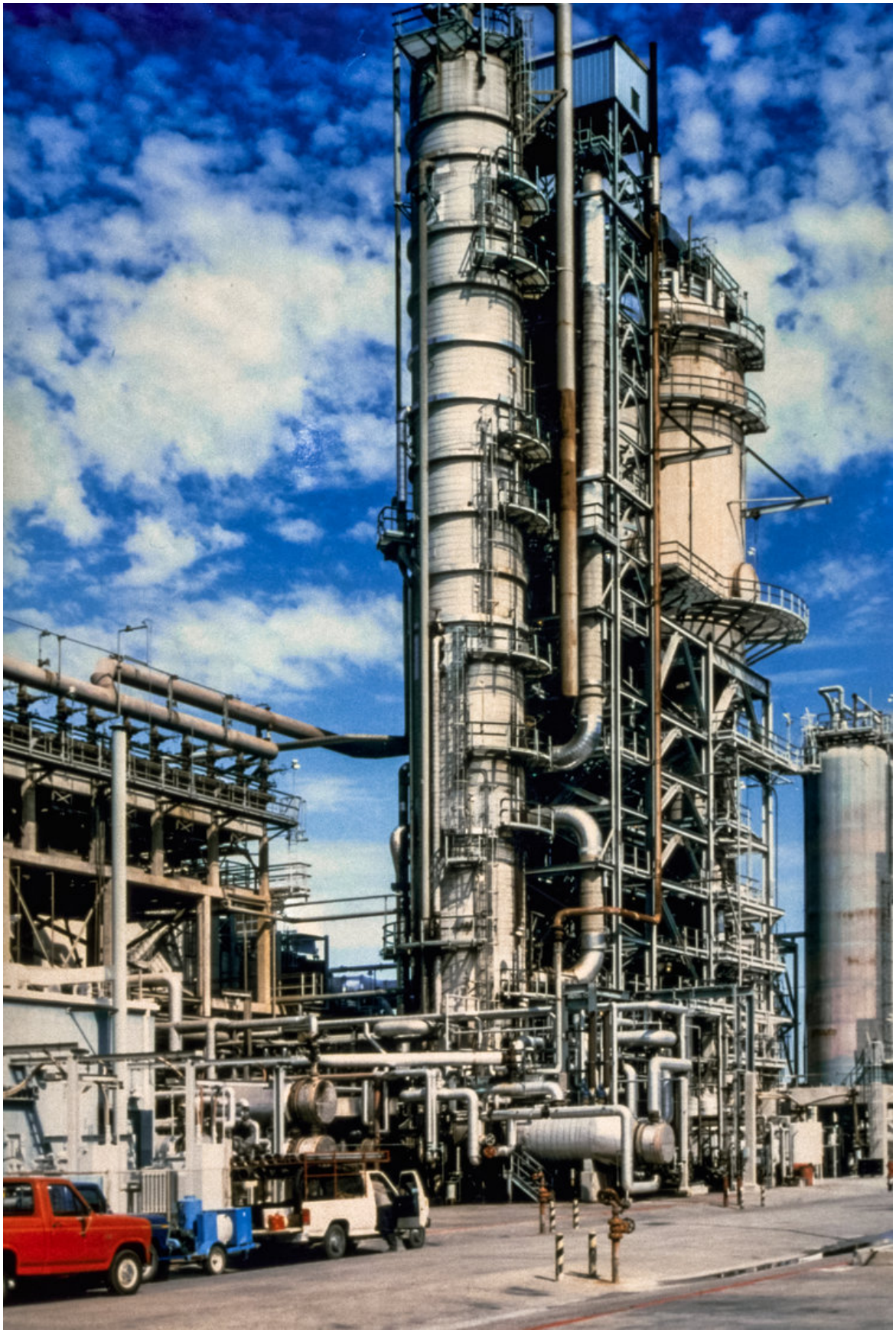

Figure 1.2 – Illustration of a Fluid Catalytic Cracking Unit. Source: www.revamps.com/fccu.

1.2 Objectives

The main objectives of this work are the study of turbulent mixing cyclonic flows with different turbulence closure approaches and the use of different substances in a non-reactive environment. The target of this research is the simulation of an inert turbulent mixing cyclonic flow inside a CO boiler with the use of adaptive refinement meshing and immersed boundaries inside the eulerian domain, in order to obtain data about the flow behavior inside the equipment. In a more specific way, the objectives are:

1. Perform a bibliographic review about turbulence and its methodologies for closure models, turbulent mixing flows, cyclonic turbulent flows and its impact in multi-component flows;
2. Study of mathematical and numerical approaches involved in the simulation of a turbulent non-reactive cyclonic flow with different substances;
3. Analysis of validations concerning Immersed Boundary Method and URANS models implemented in MFSim;
4. Validation of a mixing process involving different substances in a propane jet flow;
5. Investigate results of a non-reactive turbulent swirling flow with different turbulence closure models inside a combustion chamber;
6. Investigate results of a turbulent mixing swirling flow inside a combustion chamber in regard to velocity, mass fractions and other data.

1.3 Methodology

The CFD code used, known as MFSim, came up with the work of (VILLAR, 2007) on multi-phase flows and has been developed at the Fluid Mechanics Laboratory at the Federal University of Uberlândia in partnership with Petrobras. The code is written, predominantly, in FORTRAN language with some parts implemented in C and C++.

Nowadays, the code allows the user to simulate a diversity of three-dimensional problems with the application of different turbulence closure models, the use of immersed boundaries with the direct forcing method to represent geometrical obstacles, and the possibility of using a block-structured mesh with adaptive refinement.

1.4 Structure

The present dissertation is divided into six chapters, this being the first one, which presented a brief introduction of the subject. Chapter 2 presents the state of the art of the main topics of this research, such as turbulence methodologies and closure models, turbulent mixing, and swirling flows. In chapter 3, the methodology is presented, which includes mathematical modeling of the equations for continuity, Navier-Stokes and turbulence closure models, besides the equation of mass conservation of species. In the same chapter, numerical modeling is covered, focusing on the finite volume method, time and space discretizations, pressure-velocity coupling and the multi-direct forcing method. In chapter 4, some validations are discussed, such as a work responsible for presenting the efficiency of the MFSim code to represent immersed boundaries in an eulerian domain with the multi-direct forcing method. Besides that, a simulation of a propane main jet and a co-flow air was used to validate some turbulence closure models in a multi-component flow. Concerning chapter 5, results are obtained and discussed in respect to the simulations of a turbulent swirling flow inside a CO boiler with different substances for the final simulation. Finally, the last chapter presents a conclusion of the obtained results and the topics covered throughout the text.

Chapter 2

STATE OF ART

In this part of the dissertation, the necessary theoretical background about turbulent flows, turbulence closure models, swirling flows, and mixing flows are provided. Also, researches concerning the use of different turbulence closure models for the applications in this work are cited to provide a database of results and comparisons.

2.1 Turbulent flows: a brief history

The first records of studies considered related to turbulence might be dated from the XVI century. Leonardo da Vinci's drawing *la turbolenza*, figure (2.1), was described by the author as a water surface with "scale movements, one due to its main current and the other caused by random and reverse movement".

The mathematical study about turbulent flows was promoted by Claude Louis Marie Henrie Navier (1785 - 1836), who made the first deduction of the equations of movement of a viscous fluid in 1822, in his work *Sur les lois de mouvement des fluides* (NAVIER, 1823).

Seven years after Navier's death, Saint-Venant (1797 - 1886) introduced, for the first time, the concept of viscous internal stresses. George Gabriel Stokes (1819 - 1903) published in 1845 his article *On the theory of internal friction of fluids in motion*, where he deduced the equations of movement in a fluid, taking into account the internal friction.

Boussinesq (1877) proposed the hypothesis of the existence of proportionality between

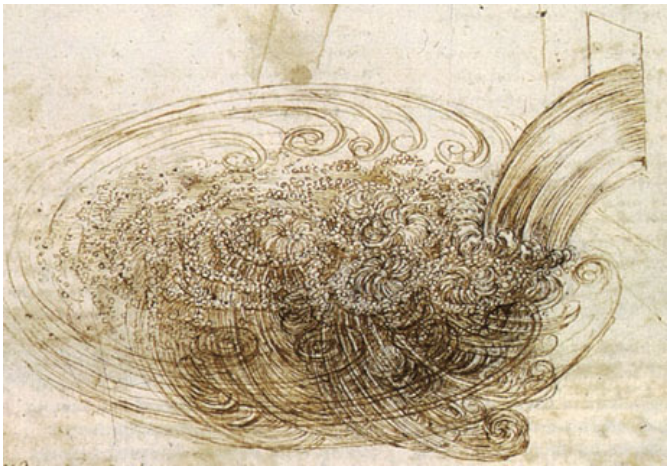

Figure 2.1 – Da Vinci's drawing capturing a turbulent flow. Source: Leonardo da Vinci, Studies of Turbulent Water, Royal Collection Trust/© Her Majesty Queen Elizabeth II 2019

the turbulent stresses and the average deformation rates. Unlike Navier and Stokes, Boussinesq deduced that viscosity did not depend only on the fluid, but also on the position within the flow and its "degree of turbulence". He also elaborated the concept of average and fluctuating quantities.

After more than a decade, Reynolds (1895) confirmed that turbulence is characterized as a random phenomenon and the velocity of fluid could be separated into two parts: mean and fluctuation, entitled by the author as "Mean and Relative Motions of Matter". His experiments provided results that led him to find a dimensionless number (Reynolds Number, *Re*), responsible for being of the main parameters involved in the transition from laminar to turbulent flows.

Ludwig Prandtl (1875 - 1953) brought the contribution of the boundary layer theory. Before his discoveries, the majority of the researches involving fluid mechanics were related exclusively to potential flows. The problem of neglecting the boundary layer is that, although the mathematical formulations seemed correct, the results were inaccurate when compared to real situations, such as potential flows resulting in null drag (ELIAS, 2018).

Prandtl noticed that the potential flow theory could be applied to a vast amount of flows as long as they don't present small regions next to walls (PRANDTL, 1904). In these zones, the viscous effects should be taken into consideration. Among his main contributions, it might be highlighted the mixing length theory, the logarithmic velocity distribution, the friction law, among others (FREIRE, 2002).

Taylor (1935) was one of the first researchers to consider a greater mathematical rigor to turbulence and to introduce statistical methods, such as Fourier Transforms and spectra study. He assumed that turbulence is a random phenomenon and applied statistics to analyze isotropic and homogeneous turbulence.

Some of the most important documents about turbulence were published by Kolmogorov (1941b) and (1941c), who introduced the most known theory about isotropic turbulence. Its theory is based on dimensional analysis and in the equilibrium hypothesis, in which, to have a steady-state, all the energy injected must be transformed by viscous effects. According to the author, he named the smallest scales in a turbulent flow as Kolmogorov Scales and, at this scale, viscosity dominates and the turbulent kinetic energy is transformed into heat. The Kolmogorov length scale is defined as: $\eta = \left(\frac{\nu^3}{\varepsilon}\right)^{1/4}$, in which ε is the turbulent dissipation rate per unit mass and ν is the kinematic viscosity of the fluid. In his theory, he introduced the idea that the smallest scales of turbulence are universal and that they depend only on ε and ν. Since the dimension of kinematic viscosity is $length^2/time$ and the dimension of the energy dissipation rate per unit mass is $length^2/time^3$, the unique combination that could result in a dimension of time is $\tau_\eta = \left(\frac{\nu}{\varepsilon}\right)^{1/2}$, known as the Kolmogorov time scale. Similarly, the Kolmogorov length scale and velocity scale, $u_\nu = (\nu\varepsilon)^{1/4}$, can be obtained by this dimensional analysis. The Kolmogorov length scale can also be obtained as the scale at which the Reynolds number is equal to 1, $Re = UL/\nu = (\eta/\tau_\eta)\eta/\nu = 1$. Even though the energy dissipation rate fluctuates in time and space, the theory uses a mean-field concept, considering that it represents the typical values of the smallest scales in a turbulent flow. The Kolmogorov Phenomenology is a theory that says that a flow field always has an energy-containing scale, which corresponds to the large eddies. The figure (2.2) illustrates a sketch of the Kolmogorov energy spectrum for all turbulent flows.

The contributions to the energy spectrum, $E(k)$, from the energy-containing scale, are located in the vicinity of the low wavenumbers. At the end of the energy spectrum is the dissipative scale, where $E(k)$ decreases exponentially as a result of the viscous action. Kolmogorov also predicted that, if the Reynolds number is sufficiently large, the energy-containing scale will be separated from the dissipation scale by an inertial range in which $E(k)$ scales as $k^{-5/3}$. The larger the Reynolds number, the wider the inertial range will be.

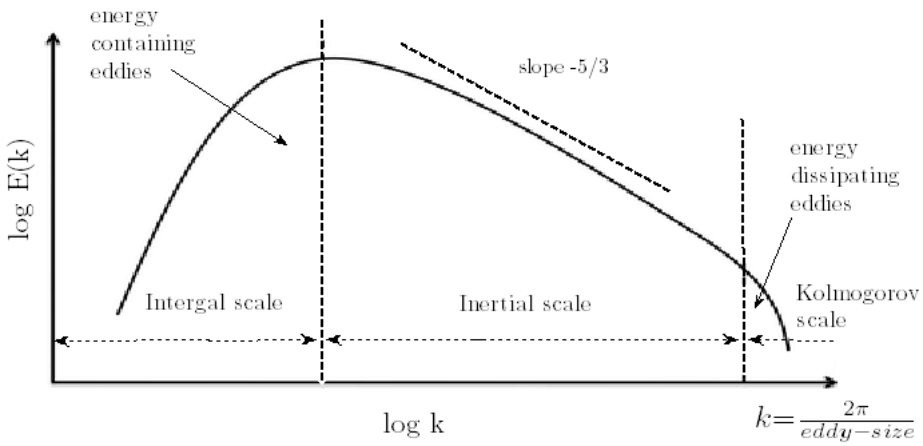

Figure 2.2 – Sketch of a Kolmogorov Energy Spectrum. (SINHA, 2013)

According to the phenomenology theory, some assumptions are made, such as the fact that turbulence is locally isotropic (at small scales, turbulence statistics are invariant under translation and rotation). Also, turbulence might be considered in "equilibrium", as the energy injection $\mathcal{F}$, responsible for driving the turbulence, is approximately matched by the rate, ε, which represents the energy dissipation by viscous effects. Also, the cascade process is local, which means that the transfer through wavenumber k depends on the dynamics of the neighborhood near k.

In the intermediate range of scale or Inertial subrange, Kolmogorov's hypothesis led to the universal form of the energy spectrum, in which $E(k)$ may be expressed as:

$$E(k) = C_K \varepsilon^{2/3} k^{-5/3}, \tag{2.1}$$

where C_K is the Kolmogorov constant, which is approximately 1.5.

During the 40's, many other contributions were realized in the turbulence field, mainly statistical treatments, such as Townsend (1947), Batchelor (1948), Burgers (1948), Heisenberg (1948) among others. Karman (1948) also contributed to the turbulence study with a dimensionless constant named von Kármán constant, which is involved in the logarithmic law describing the distribution of a longitudinal velocity in the wall-normal direction of a turbulent fluid flow near a boundary with no-slip condition. It is often used in turbulence modeling, for example, in boundary-layer meteorology to calculate fluxes of momentum, heat, and moisture from the

atmosphere to the land surface (HÖGSTRÖM, 1996). He also studied the nature of vortex emissions in flows downstream of a bluff body.

Despite the development of experimental instrumentation and its use in turbulence researches during the 50's and 60's, the advances that would change the direction of understanding turbulence were obtained with the advent of digital computers (DAMASCENO, 2012).

During the 70s and 80s, the most relevant advances were related to computational techniques and hardware. Deardorff et al. (1970) explored the Large Eddy Simulations (LES) technique, while the Direct Numerical Simulations (DNS) were studied by Orszag and Patterson (1972). The approximations of the Reynolds-Averaged Navier-Stokes (RANS) were studied and well-known at that time by Launder and Spalding (1972) and Launder, Reece and Rodi (1975). The RANS methodology gained attention at that time because the other approaches didn't seem to be viable, which was emphasized by Ferziger (1985), who mentioned DNS and LES for being impracticable for engineering applications.

In the mid 90s, with the advances of computational resources, the LES methodology gained notoriety for engineering applications with simple geometries involved. Interesting works and reviews were published, such as those by Lesieur and Metais (1996) and Meneveau and Katz (2000).

Chapman and Tobak (1985) proposed a point of view about the turbulence study evolution, named as Modern Scientific Study of Turbulence dated from the late 1800s with the work of Osborne Reynolds. These periods are: statistical, structural, and deterministic.

The statistical is motivated by the belief that turbulence presents random characteristics, even though, some researchers accepted the deterministic approach of using Navier-Stokes equations to represent turbulent flows (DAMASCENO, 2012). Some important names of this movement are Reynolds, Boussinesq, Pradtl, Taylor, Kolmogorov, Lauder, Wilcox, Spalart.

The structural movement was characterized by the analysis of the influence of coherent structures on turbulent flows, started by the observations of Schubauer and Skramstad (1947) about the Tollmien-Schlichting waves, which are important names for this movement.

According to Chapman and Tobak (1985), the deterministic movement started with the work of Lorenz (1963). The author said that lack of periodicity is a common characteristic in turbulent flows and, because instantaneous turbulent flow patterns are irregular, attention is directed to statistics of turbulence, which behave in a regular well-organized manner though. As an example, Lorenz (1963) cite the weather forecaster, which presents large-scale turbulent eddies (cyclones) and is continually in random rearrangement, evidencing that there are occasions that a statistical approach of irregular flows cannot be enough. Therefore, the author studied systems with non-periodic solutions, where all approximate repetitions are of finite solution and never repeat their history. Dissipative processes, added to the inclusion of external mechanical forces and/or thermal forces, preventing the system from achieving a state of rest. If not constant in time, these forcing functions might vary according to a deterministic rule.

Turbulence has been a problem of great complexity and has been attracting the attention of renowned scientists over the years. One example is the Nobel Prize winner in physics in 1965, Richard Feynman (1918 - 1988), who described turbulence as "*the most important unsolved problem of classical physics*". Another researcher, the mathematician Horace Lamb (1849 - 1934) once said: "*I am an old man now, and when I die and go to heaven there are two matters on which I hope for enlightenment. One is quantum electrodynamics, and the other is the turbulent motion of fluids. About the former, I am rather optimistic*".

Nowadays, even after so many studies and conclusions, there is so much to understand about this chaotic, intriguing, and important phenomenon.

2.2 Turbulence origins

In laminar flows, usually, turbulence develops from the amplification of instabilities with high Reynolds numbers.

The Reynolds number might be understood as a ratio between inertia forces and viscous forces. When this dimensionless number is low, viscous forces are more relevant than inertia forces, which characterizes a situation with an important viscous damper inside the flow and, consequently, oscillations disappear rapidly. In this manner, small disturbances in the velocity

field created by small regions of surface roughness or disturbances in the pressure field, originated by external sources such as surface vibrations or sound waves, will be dampened and, therefore, not amplified.

This is the case for flows in ducts with a Reynolds number of approximately 2300 (based on the pipe diameter and mean velocity), as well as for boundary layers with a Reynolds number below 200,000 (based on the layer thickness and the free current velocity). As the Reynolds number increases, the viscous damping becomes comparatively lower and, at some point, it becomes possible for small disturbances to grow. Then, the flow becomes unstable and experiences a transition to a turbulent regime where large variations in the velocity field can be maintained.

If disturbances are really small, as the ones generated by very smooth surfaces, the transition to turbulence might be delayed to higher Reynolds numbers.

It is interesting to note that, once the amplification process has started, turbulence needs energy to maintain itself. One of those responsible for maintaining velocity fluctuations is the shear stresses. Turbulent flows are generally shear flows. If the flow reaches a region where there is no shear or another mechanism that transfers energy to maintain turbulence, it decays. In this case, the number of local Reynolds decreases, and the flow tends to be laminar again. There are other ways to make a turbulent flow turn laminar or even prevent a laminar flow to become turbulent, such as the presence of a magnetic field or flows with stable stratifications, for example, (TENNEKES; LUMLEY, 2018).

2.3 Characteristics of turbulent flows

Concerning the turbulence characteristics, it presents a large range of scales. The bigger structures in a flow are defined by the characteristic flow geometry, such as the diameter of a jet, cylinder or a sphere, the dimension of a channel, an airfoil, among other examples. Otherwise, the smallest structures are determined by the Reynolds Number, presenting a universal behavior independently on the characteristic geometry. These structures evidence the importance of molecular diffusion and viscous energy transformation.

Another turbulent characteristic is the elevated diffusion levels. There is a great presence of fluctuations of some quantities transported, such as mass, internal energy, linear *momentum*, among others, and, due to the strong local gradients, the molecular diffusion process becomes more efficient.

The irregularity is another characteristic present in turbulent flows. It is a phenomenon of hard deterministic prediction, which contains large structures with coherent statistical behavior, while the small structures are known to be random.

Turbulence is a phenomenon that highly depends on the ratio between advective and diffusive effects of linear *momentum*, known as Reynolds Number, Re. The advective effects (non-linear) are responsible for generating instabilities, while the diffusive effects work as dampers or even avoid perturbations. That is why the value of this dimensionless relation is always more than the unity, as the advective terms might excel over the diffusive ones.

Another feature of turbulence is that the flow is three-dimensional and has fluctuations of vorticity, so being characterized as three-dimensional and rotational.

Turbulence is also a highly dissipative phenomenon. The viscous dissipation of the turbulent kinetic energy happens in the high frequencies, which is responsible for the enhancement of the internal energy. In a fully developed turbulent regime, all the energy injected into the flow must be transferred through the spectrum of swirling structures to the dissipative frequencies. A continuous energy supply to the flow is required, otherwise, there will be a decay of the turbulence level.

Turbulence can also be considered a continuous phenomenon. The Navier-Stokes equations are only valid as long as the representative physical length scale of the system is much larger than the mean free path of the molecules that make up the fluid. Knowing that these equations are valid to describe any sort of flow, turbulent or not since their Mach number is inferior to 15, a turbulent flow might be considered in a *continuum* context as the smallest turbulent length scales are bigger than the mean free path of the molecules.

Ultimately, this type of flow presents a chaotic property, being impossible to realize two identical experiments in laboratory, due to the difficulty of the exact reproduction of initial and

boundary conditions. Owing to non-linear effects, instabilities can be easily amplified, which produces different results.

2.4 The mathematical modeling of turbulence

The Navier-Stokes equations can model laminar or turbulent flows in a detailed and precise way. When in a turbulent context, it is harder to describe all the velocity and pressure fields from the biggest to the smallest length and time scales, since the amount of information is vast and, for practical purposes, impossible. Thereby, three main resolution methodologies are used: Direct Numerical Simulation (DNS), Large Eddy Simulations (LES), and Reynolds Averaged Navier-Stokes (RANS).

The DNS methodology calculates all turbulence scales with the resolutions of the Navier-Stokes equations without the use of any turbulence closure model. For this reason, a mesh refinement with low time steps capable of analyzing all spectrum of frequencies is required, from the biggest structures to the Kolmogorov scale, otherwise, there will be a spatial filter without a closure model and the results will be inaccurate. This method is complex to be used in industrial applications but very useful in low Reynolds number situations, such as laminar flows and academic experiments. Knowing the constraints imposed by the available technology in calculating the equations with the DNS approach, the other methodologies arose to make turbulent flow analysis possible.

The RANS methodology is based on time averages with the decomposition of velocity in an average and fluctuating portion and the complete modeling of the energy spectrum. As a statistical description, it suffers from the curse of closure with the necessity of calculating the Reynolds Stress Tensor, an additional term that arises from the averaging operations applied to the Navier-Stokes equations. The RANS methodology requires a lower level of refinement compared to the others. Therefore, it might be preferable for calculating flows with high Reynolds numbers, which is the majority of cases in industrial applications. However, a large amount of information is lost due to the approximations and modelings of the entire energy spectrum.

Knowing that a coarser mesh is used for RANS modeling, the structures present in the

flow are not resolved. Hence, it is apparent that a mechanism is needed to contemplate the physics of these uncalculated structures, mainly the viscous dissipation. Boussinesq (1877) proposed, then, the use of an additional variable named turbulent viscosity (ν_t) to model the Reynolds stress tensor represented by the equation (2.2). This variable aims to intensify the diffusion process, since it is added to the molecular viscosity of the fluid, composing what is called effective viscosity.

$$\tau_{ij} = \overline{u_i' u_j'} = -\nu_t \left(\frac{\partial u_i}{\partial x_j} + \frac{\partial u_j}{\partial x_i} \right) + \frac{2}{3} \left(k + \nu_t \frac{\partial u_k}{\partial x_k} \right) \delta_{ij}, \tag{2.2}$$

where ν_t is the turbulent viscosity, k is the turbulent kinetic energy, δ_{ij}, the Kronecker delta and the term $\partial u_k / \partial x_k = 0$ if the flow is incompressible.

The ways of obtaining the turbulent viscosity may vary, depending on the closure model used. According to the nomenclature used by Wilcox (2006), the closure models may be classified as:

- **Algebraic models or zero transport equations:** no additional transport equations are solved in this case. The Prandtl mixing length theory is used with Boussinesq's hypothesis. The turbulent viscosity may be modeled using an analogy for the molecular viscosity with the kinetic theory of gases. The molecular kinetic viscosity is modeled by the product of the speed of sound in a gaseous medium with the free molecular average path. This means that the turbulent kinematic viscosity can be modeled as the product of a length by a velocity, both characteristic quantities of a turbulent flow. Some examples are: Smith and Cebeci (1967) and Baldwin and Lomax (1978).

- **One equation models**: one additional transport equation is solved to assess the turbulent viscosity. The first model of this kind was postulated by Prandtl (1945), who proposed the calculation of turbulent viscosity from the solution of a transport equation for turbulent kinetic energy. Some examples: Baldwin and Barth (1991) and Spalart and Allmaras (1992).

- **Two equations models:** two transport equations are solved to obtain turbulent viscosity. Kolmogorov (1941a) proposed the first model of this kind, named $k - \omega$ model. Other models were disseminated, such as the standard $k - \varepsilon$ model (JONES; LAUNDER, 1972; LAUNDER; SHARMA, 1974), the realizable $k - \varepsilon$ model (SHIH et al., 1995), a more advanced $k - \omega$ model (WILCOX, 1988; WILCOX, 2006), the SST model (MENTER, 1994), among others.

- **Reynolds Stress Models:** additional transport equations are solved for the Reynolds stress tensor components. Although they still use Boussinesq's hypothesis for closure, they present a superior performance in flows with strong anisotropy owing to the more detailed way of analyzing the Reynolds tensor. However, they present a higher computational cost when compared to the other closure models, besides presenting a high numerical instability, since a higher value of viscosity is a known numerical stabilizer and RSM does not increase this property. In these models, the turbulent viscosity approach is avoided and the individual components of the Reynolds stress tensor are directly computed, which makes it possible to account for complex interactions in turbulent flow fields. This modeling originates from the works by Chou (1945) and Rotta (1951).

Although they are sufficient for most engineering problems, average flow information is incomplete or inaccurate when studying situations as, for example, vortex-induced vibrations which depend on the analysis of a certain detailed level of the detachment of swirling structures.

Another problem is related to meteorological studies, in which a DNS approach would be impracticable due to computational cost, while RANS is not able to obtain essential information about the fluctuations of the velocity and pressure fields.

That is why Smagorinsky (1963) sought an alternative, known as Large Eddy Simulations (LES). With this modeling, only a part of the spectrum is resolved, limited by the mesh resolution. In this way, the part of the spectrum with large structures is resolved, which carries most of the flow energy. The interaction of these resolved structures with those not captured by the resolution is modeled. Smagorinsky (1963) himself proposed a model that bears his name, using

Boussinesq's hypothesis. Subsequently, improvements were made by Germano (1986) and Lilly (1992).

Even though URANS and LES were briefly presented in this chapter, a more detailed explanation will be given in Mathematical Modeling section.

2.5 Turbulent mixing flows

The ability of turbulent flows to effectively mix entrained fluids to a molecular scale is a vital part of the dynamics of such flows, with wide-ranging consequences in nature and engineering.

A simple example is the mixing of scalars (substances with no identifying labels other than their concentrations) that are chemically neutral with initially flat and stationary interfaces separating them and absent forces, such as surface tension and gravity. Molecular diffusion induces the separating interface to increasingly encroach with both substances over time, reducing the concentration gradients. A way to maintain the concentration gradients and the effectiveness of diffusion is to use an external flow to constantly push the substances toward each other. Thus, the flow destabilizes, distorts, and sharpens an interface while increasing its surface area and enhancing diffusion effects. In the simple case, the mixing of scalar does not affect the flow itself, which is called passive scalar mixing. In practice, there are some complications, such as the presence of external forces, chemical reactions, multiple species, density differences, but the essence of mixing is the relation of the flow of substances and their capacity to diffuse and mix molecularly Sreenivasan (2019).

To illustrate a mixing of passive scalars, Sreenivasan (2019) gives the following example: the deposition of a blob such as a neutral dye within a tank of stirred fluid. The blob will be stretched, folded, fragmented, and dispersed in the fluid volume. The interface area and scalar gradients across it are enhanced due to fragmentation and stretching of the blob, the role of diffusion being secondary at this stage. However, two thin fragments of the stretched pieces of scalar with opposing gradients often come together and coalesce into a single entity, in which diffusion plays more than a secondary role. The figure (2.3) illustrates a mixing process of a blob

in which the scalar gradient is prescribed initially as a Gaussian distribution. the timescales on the bottom left corners are multiple of the Kolmogorov timescales.

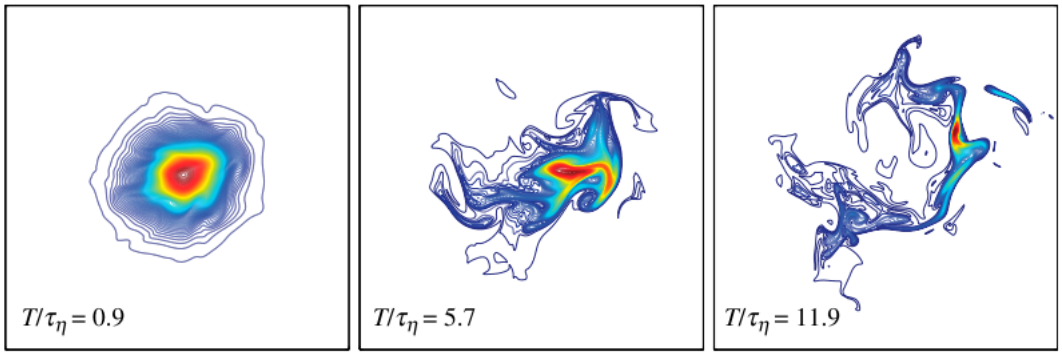

Figure 2.3 – Mixing of a Gaussian blob in a homogeneous isotropic statistically stationary turbulent flow. Just one blob was introduced at t = 0. (SREENIVASAN, 2019)

If a probability density function of the scalar concentration is measured in a completely unmixed state, there will be visible two delta functions, one which corresponds to zero of the background fluid with no scalar and the second corresponding to 1 of the unmixed scalar blob. The blob may be contorted and stretched by the flow, but the PDF will only change when diffusivity takes place. Then, an intermediate peak between 0 and 1 is developed, corresponding to the mixed fluid, and the two peaks at 0 and 1 gradually diminish as the middle peak becomes dominant. Therefore, the fraction of the mixed fluid is represented by the area under the middle peak.

Small perturbations in a multifluid system grow due to buoyancy and shear-driven instabilities at the interface between two distinct fluids. These instabilities produce turbulent mixing and there are three major types that take place in mixing processes. The first one is called Rayleigh-Taylor (RT) instability, which happens when a fluid accelerates another fluid of higher density. The second instability is called Richtmyer-Meshkov (RM) instability, which occurs when a shock wave accelerates a perturbed interface between two fluids of different densities. The last type is the Kelvin-Helmholtz (KH) instability, which takes place when a non-zero tangential velocity gradient exists between the two fluids. These instabilities are usual in technological applications, such as laser ablation, combustion, pharmaceutical procedures, supernova explosions, atmospheric flows, among others (CHENG, 2009).

The entrained flow, or otherwise introduced in a turbulent region, is transported and dispersed across it by motions induced from the largest to the smallest eddies, where molecular diffusion happens. Also, that is where a high Reynolds number turbulent flow generates a large interfacial surface area that permits the otherwise slow molecular mixing to take place efficiently (DIMOTAKIS, 2005).

According to Eckart (1948), turbulent mixing can be seen as a three-stage process of entrainment, dispersion (or stirring), and diffusion. In the simplest case, labeled as Level-1 mixing, it is configured as a passive process, as occurs among passive scalars. Some examples are density-matched gases, the dispersion, and mixing of non-reacting trace markers, such as small temperature differences, pollutants, small particle cloud, low concentrations of particles in a fluid, among others. This sort of mixing is not coupled back on the flow dynamics, so a correct accounting of mixing is not required to describe the flow dynamics (DIMOTAKIS, 2005).

The Level-2 mixing is coupled to the dynamics, such as what happens in different-density fluids submitted to a gravitational, acceleration field, as in Rayleigh-Taylor instability flow (when a lighter fluid pushes a heavier fluid).

The Level-3 mixing causes changes to the fluid(s) as, for example, in composition, density, enthalpy conversion/release, pressure increase, and is coupled to the dynamics. Some examples are combustion phenomena, detonations, among others.

According to Dimotakis (2005), progress in the study of turbulent mixing has been mostly concentrated to Level 1, with results for high Reynolds number flows limited to a few canonical cases, such as free shear layers and jets, pipe flows, isotropic turbulence, among others. Level 2 and 3 mixings are less well developed and are considered as an open research topic.

2.5.1 Passive-scalar mixing

The classical equation for studying passive-scalar mixing is the advection-diffusion equation:

$$\frac{\partial \theta}{\partial t} + (\mathbf{u} \cdot \nabla)\theta = \mathcal{D}\nabla^2\theta, \tag{2.3}$$

where θ is the scalar concentration,$\mathcal{D}$ is the molecular diffusion coefficient, and **u** is the velocity advecting θ. Knowing that the scalar is passive, **u** defines, along with L and ν, the Reynolds number of the flow. Besides, the Schmidt number, Sc, that is indicated by the ratio $\nu/\mathcal{D}$, also matters. This dimensionless number could be as small as 10^{-6} in the Sun's interior, of order unity when the scalar is a modest amount of heat in air and 10^3 for a water-soluble dye in water. The equation (2.3) presents some limitations as a model for mixing (LANDAU; LIFSHITZ, 1987), but it is still good for some applications, such as in technology, oceans and atmosphere.

2.5.2 Modeling and Simulation

According to Dimotakis (2005), the approach that has, perhaps, shown the most promising results for mixing simulations is based on Large Eddy Simulations (LES), augmented by Sub-Grid Scale (SGS) modeling (LESIEUR; METAIS, 1996).

This modeling can rely on extrapolations of velocity/scalar behavior to the smaller, sub-grid scales. One SGS model that specifically addresses mixing with promising results is described in Pullin (2000) and Voelkl, Pullin and Chan (2000). Pullin (2000) compared this model with an LES with no model and a DNS, using an imposed mean gradient for Sc = 0.7 and found out that the SGS model is in accord with the DNS results.

Wegner, Huai and Sadiki (2004) researched a turbulent mixing in a cross-flow with three different angles of jet injection using LES simulations. According to them, many experimental and numerical studies have shown that three-dimensional and unsteady vortical structures provide a very efficient mechanism for the mixing process between the jet and the cross-flow. Despite the micromixing behavior being considered as anisotropic by some experimental works (WARHAFT, 2000), the majority of simulations use an eddy diffusivity model in which the unresolved scalar flux terms are aligned with the resolved-scale scalar gradient and are assumed to be proportional to an isotropic sub-grid viscosity, giving acceptable results. Their work used an eddy diffusivity model of a constant Schmidt number ($Sc_t = 0.7$), a relationship between the turbulent diffusion coefficient and the turbulent viscosity.

According to Wegner, Huai and Sadiki (2004), the LES approach was able to represent

the mixture fraction quite well for all the injection angles investigated. Also, the mixing process was affected by the imposed perturbations or even the vortex formations. As an example, it was found that an injection of 120° against the cross-flow direction turns the mixing process more efficient than an injection of 60° at the same direction of the cross-flow, evidenced by the probability density function of mixture fraction. Also, the 60° case showed the highest levels of fluctuations, while the 120° presented the lowest levels. Besides, the presence of counter-rotating vortices increases the spreading rate of the jet and, thus, the entrained fluid into the jet, enhancing the mixing event.

Considering the energy spectra, Wegner, Huai and Sadiki (2004) noted that, for complex flows involving scalar transport, an additional sub-range exists next to the $k^{-5/3}$ sub-range with a steep dependence on k according to k^{-m}, with generally $m > 5/3$. Interested in global mixing, the authors analyzed a quantity named "mixedness parameter", proposed by Fric (1996) which varies from 0 to 1, with 0 indicating completely separated fluids and 1 standing for mixed fluids.

Ivanova, Noll and Aigner (2010) studied a turbulent mixing of a jet in a crossflow with the approaches: RANS, URANS (SST $k - \omega$ turbulence model) and SST-SAS model.

According to Ivanova, Noll and Aigner (2010), to account for the scalar transport, the turbulent Schmidt number hypothesis is applied due to its simplicity, even though not satisfying the physical reality. Concerning the results, the steady-state RANS is not accurate, which violates the physical due to the presence of large-scale coherent structures, which are unsteady and asymmetric about the jet center plane. Using URANS, the velocity field can be well predicted and grid independence can be achieved earlier compared to the SAS method. However, URANS presents a small amount of resolved kinetic energy and the turbulent Schmidt number approach is not accurate to achieve satisfactory mixing predictions in the entire flow field.

Using the SST-SAS model, it showed a good potential for a correct prediction of the mean and fluctuating velocities and scalar fields in the simulations of Ivanova, Noll and Aigner (2010). However, the accuracy of SAS predictions is not quite satisfactory. Concerning the turbulent kinetic energy, in the SAS simulations, more than 80% of this quantity is resolved, which causes an additional production of the term $Q_{SST-SAS}$, while in the URANS simulations,

the modeled part prevails. The level of ν_t using SAS downstream of the jet injection is lower than for URANS, which causes a large amount of energy-containing eddies to be resolved in SAS simulations. The turbulent fluctuating quantities are better predicted by methods that allow a deeper level of resolution of the turbulent kinetic energy. The authors believe that the lack of accuracy might be due to the transition from "URANS" to a "scale-resolving" mode, knowing that turbulent fluctuations are only resolved at some distance from the jet exit. Therefore, the reason might be due to the term $Q_{SST-SAS}$ that does not come into effect in the jet tube since the flow instabilities there are not strong enough. Additional forcing of this term in the jet exit or fluctuating inlet boundary conditions would help to reduce this issue. It is shown in the experiments of MI, NOBES and NATHAN (2001) that the turbulent jet exit conditions can affect the scalar mixing processes even much more than they affect the jet velocity field (IVANOVA; NOLL; AIGNER, 2010).

2.6 Swirling Flows

Swirling flows occur in a wide range of applications, such as cyclone separators, whirlpools, tornadoes, reactors, agricultural spraying machines, among others. In combustion systems, such as gasoline engines, industrial boilers, gas turbines, it is used as an aid for stabilization of the high-intensity combustion processes and efficient clean combustion (GUPTA; LILLEY; SYRED, 1984).

There are several ways to generate the rotation of a flow. One of them is to use propellers tangentially deflecting the axial flow, which are simple devices used in industrial systems but may introduce head losses and the intensity of the swirl is limited. Another way is to use rotating mechanical devices to employ rotational movement to the fluid passing through them (BOUSHAKI, 2019). At last, tangential injection of fluid by ducts with some differences in their angles might cause a swirl generation at the center of equipment, such as the industrial boiler studied in this research.

Swirl flows result from the application of a tangential velocity component imparted to the flow by swirl vanes, by the use of axial-plus-tangential entry swirl generators, or by direct

tangential entry. Experiments show that jet growth, entrainment, flame size, shape, stability, and combustion intensity are affected by the degree of swirl present in the flow (GUPTA; LILLEY; SYRED, 1984). This degree of swirl is characterized by the swirl number S, a nondimensional number represented by:

$$S = \frac{G_\theta}{G_x d/2}, \tag{2.4}$$

$$G_\theta = \int_0^\infty (\rho uw + \rho\overline{u'w'})r^2 dr, \tag{2.5}$$

$$G_x = \int_0^\infty (\rho u^2 + \rho\overline{u'^2} + (p - p_\infty))r dr, \tag{2.6}$$

where G_θ is the axial flux of swirl momentum, including the turbulent shear stress term and G_x is the axial flux of axial momentum, including the turbulent normal stress term and a pressure term. $d/2$ is the nozzle radius and u, v, w are velocity components in X, Y and Z directions.

Knowing that this characterization might be difficult to be measured with certainty, a useful deduction for a solid body rotation plug flow can be assumed:

$$S = \frac{G/2}{1 - (G/2)^2} \tag{2.7}$$

where $G = w_{mo}/u_{mo}$ represents the ratio of maximum velocities at the exit plane. For furnaces, a modified swirl number might be used, based on furnace radius instead of inlet nozzle radius.

In terms of the generation of swirl flows, commercial burners tend to adopt the *guided vane system*, where vanes are so positioned that they deflect the flow direction.

Considering a jet flow from a nozzle, at high swirl degrees, strong radial and axial pressure gradients are set up near the nozzle exit, which generates an axial recirculation in the form of a central toroidal recirculation zone, figure (2.4), which is not seen for weaker degrees of swirl.

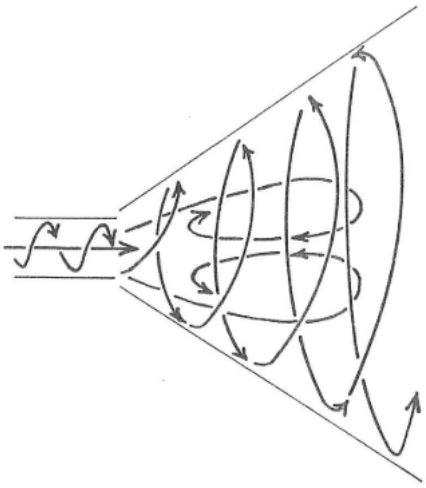

Figure 2.4 – Central Toroidal Recirculation Zone in a swirling jet flow. (GUPTA; LILLEY; SYRED, 1984)

A swirling flow can be cast as two types according to the radial distribution of their tangential velocities. The *free vortex* can be described by the swirling jet flow ejected from a nozzle into a stagnant fluid. When the jet emerges from the nozzle, the tendency of the body to continue in a straight line causes the jet to spread radially outwards, producing a conical shape as the distance of the fluid from the nozzle is increased. The tangential velocity is reduced with radius due to the dissipation of the kinetic energy of the jet into the stationary fluid. This reduction is described by the relation:

$$W = \frac{C}{r}, \tag{2.8}$$

where W is the tangential velocity, C is the maximum tangential velocity, and r, the radial distance from the center of the jet Gupta, Lilley and Syred (1984).

The *forced vortex* or *solid body rotation* is described by the generation of swirl via wall friction in an axially rotating cylinder. The velocity obtained at the wall decays radially towards the axis of the cylinder, vanishing in an axisymmetric flow. It is governed by:

$$W = C_{\Omega} r, \tag{2.9}$$

where C_{Ω} is the angular velocity at the pipe wall.

The axial vortex core of the free vortex must have a small forced vortex about the axis where equation (2.8) does not hold. At first, an undefined tangential velocity would appear at zero radii and, secondly, the sign of the tangential velocity must change at the axis of symmetry, which can only be described by the forced vortex flow. The free vortex flow has its maximum velocity close to the central axis, while the forced vortex presents its maximum velocity near the radial extremities. A combination of the two types of vortex flows leads to the Rankine vortex, where the inner part is governed by the forced vortex, while the outer part is represented by the free vortex type (JONES, 2004).

In real swirling flows, the tangential velocity distribution is intermediate between forced and free vortex flow. Concerning the pressure over a fluid element, a gradient in static pressure is responsible for balancing the centrifugal force. This pressure gradient acts over the surface of the particle and toward the axis of rotation, keeping the element in its path. The pressure in a swirling flow increases with the distance from the axis of rotation (KRISHNA, 2009). A real swirling flow normally has a Rankine vortex behavior, with a core of near solid-body rotation surrounded by a near loss-free rotation region, as shown in the figure (2.5).

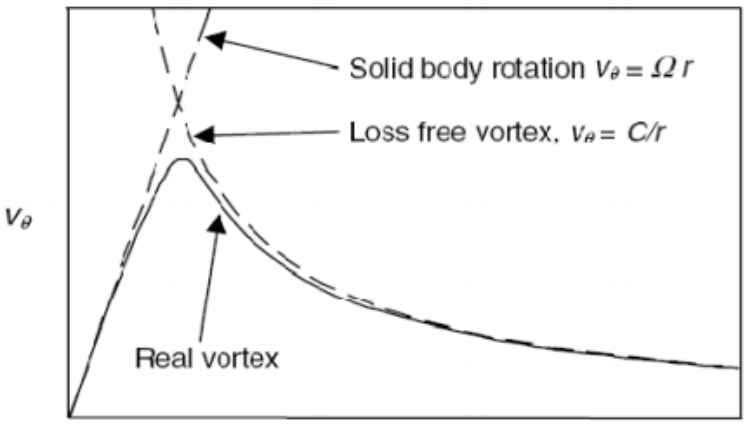

Figure 2.5 – Sketch representing the tangential velocity distribution in a Rankine vortex.(HOFFMANN; HOFFMANN; STEIN, 2002)

According to Jones (2004), the addition of swirl to a flow can modify the flow field in such a way that recirculation is produced, like a toroidal recirculation zone, relevant for combustion applications .

A swirl can produce a vortex breakdown which refers to a disturbance characterized by

the formation of an internal stagnation point on the vortex axis and by a reversed flow in a region of limited axial extent (LEIBOVICH, 1978).

2.6.1 Turbulence and swirling flow

Turbulence is often produced in wall-bounded or in shear flows due to the shear produced by the difference of speed of some flow layers, causing vortex roll-up and shedding. Swirl introduces a tangential component to the strain field, opposed to the usual axial and radial components, making the strain field more complex. To understand how swirl affects turbulence, it might be interesting to compare the rotation vector of the whole flow, Ω, to the local vorticity of a small fluid element, ω.

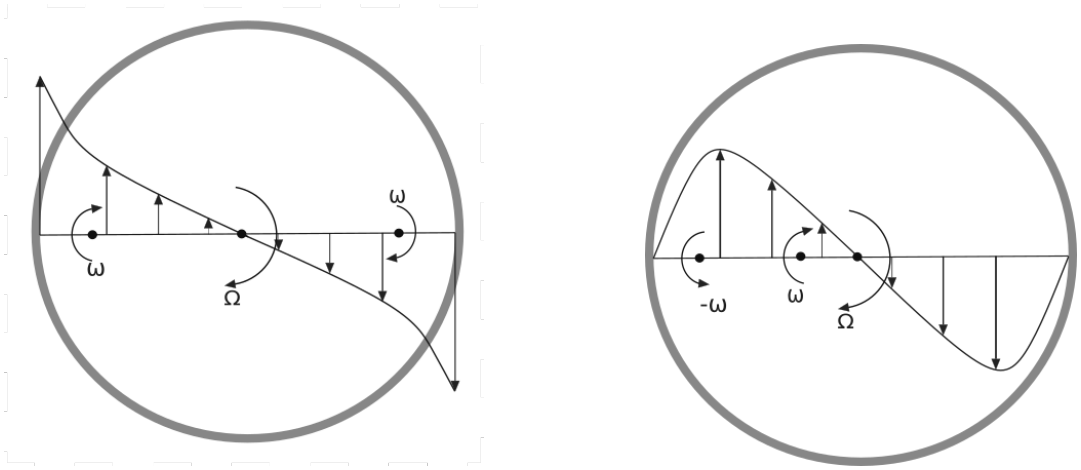

(a) Rotating pipe (b) Stationary pipe

Figure 2.6 – Effect of swirl on turbulence. Based on Jones (2004)

When the local vorticity is aligned with the rotation of the bulk flow, as in figure (2.6a), considering a rotating pipe flow, local shear is reduced, so small turbulence is produced. The flow might even become laminar, depending on the rotation speed, if the turbulent dissipation outweighs its production. For a stationary pipe, the reverse radial gradient of the tangential velocity makes the local vorticity ω have an opposing sign to that of Ω. This increases turbulent production due to the enhancement of shear stresses. At the core of the vortex, however, both the local and bulk rotation are aligned, reducing the production of turbulence (JONES, 2004).

It is known that an internal recirculation zone or vortex breakdown often appears when the strength of the swirl is high enough. In a combustion context, this zone can promote a

more efficient component mixing and a higher intensity of combustion (WANG, 2005). Internal swirling flows with high intensity and the presence of vortex breakdown may be characterized by their anisotropy for the Reynolds stresses. This anisotropy can be described following the equation (2.10), where the first term refers to the Reynolds stress contribution and the second term is the dissipation of turbulence (HERNANDEZ et al., 2018).

$$a_{ij} = \langle u_i u_j \rangle - \frac{2}{3} k \delta_{ij}. \tag{2.10}$$

The normalized anisotropy, cited by Hernandez et al. (2018), is demonstrated by the equation (2.11).

$$\bar{a}_{ij} = \frac{\bar{u}_r \bar{u}_z^2 + \bar{u}_r \bar{u}_\theta^2}{2k}, \tag{2.11}$$

where k is the turbulent kinetic energy and u_r, u_θ and u_z are radial, tangential and axial velocities, respectively.

To predict the turbulent contribution to swirling flows, it would be necessary to solve the time-dependent Navier-Stokes equations on a numerical mesh fine enough to capture the smallest turbulent motions (Kolmogorov scales). Knowing that this is impracticable in terms of computational cost, turbulence models can be applied to provide some information.

One of the most popular models are the two equation $k - \varepsilon$ and $k - \omega$ models. They have been tested with some variants like the *Shear Stress Transport* (SST) model (CHEN; LIN, 1999; YARAS; GROSVENOR, 2003), but they are unable to capture free vortex motion, exhibiting a premature solid-body rotation. Also, $k - \varepsilon$ models are based on an isotropic approach and are unable to catch the anisotropy of strong swirling flows.

Reynolds Stress Models showed improved performance compared to the two equation models for flows such as the turbulent free jet by Younis, Gatski and Speziale (1996). It was also successful to calculate free vortex flow in a cylinder by Chen and Lin (1999). Lu and Semião (2003) showed successful results of confined swirling flows with the use of an improved RSM model, in which an anisotropic dissipation rate model was used to calculate the turbulent kinetic

energy.

Grotjans (1999) simulated a strong Rankine-type vortex flow in a hydrocyclone using an eddy-viscosity model, a modification of this model for streamline curvature and two Reynolds stress models. The streamline curvature and the strong anisotropy of the turbulent field pose some challenges for the turbulence models. According to the author, the $k - \varepsilon$ models have some deficiencies, which are caused by the eddy viscosity assumption. The flow phenomena that might be calculated inaccurately or erroneously by this sort of model are: streamline curvature, stagnation point flows, adverse pressure gradient flows, and separation. As stated by Grotjans (1999), a potential remedy would be the application of Reynolds Stress Models (RSM), which solve a transport equation for each stress component, being sensitive to the anisotropies in the flow field. Besides that, the production term in these equations is important for streamline curvature effects, impingement and rotation.

The Reynolds stress tensor equation (2.2) indicates that the stresses depend linearly on the strain and this is valid only for one-main strain flow. Thus, the anisotropy in a swirling flow cannot be accounted for, since this proportionality is not true for all components (GROTJANS, 1999). However, a curvature correction method can be a way of improvement of this model to consider sensitivity to streamline curvature.

From the results, Grotjans (1999) demonstrates that the quadratic model SSG of RSM methodology is more appropriate to represent the Rankine-vortex. Also, a small but not satisfactory improvement could be obtained by applying the curvature correction method. The $k - \varepsilon$ models show a tendency of a typical solid-body rotation where there should be a potential vortex, due to the eddy viscosity hypothesis, which causes the overestimation of turbulent stresses. After a turbulent kinetic energy analysis, it could be seen that the high turbulence increases the momentum transport, which results in the tendency of solid body-rotation behavior. The values of this parameter were much higher for the $k - \varepsilon$ compared to the RSM model, the $k - \varepsilon$ with curvature correction situated between them.

Mare, Jones and Menzies (2004) used LES to research confined non-reacting turbulent swirling flows in a model dump combustor. It could be analyzed that LES can provide an accurate

solution as well as capturing the vortex breakdown, the recirculation zones, and anisotropic structures for the swirling flow.

Orbay et al. (2013) investigated a swirling turbulent flow in a combustion chamber experimentally and numerically using the LES approach. The aim was to characterize flow structures and turbulence in a combustor that is important to gas turbines. It was found that LES simulations presented a consistent agreement on the flow field and velocity variance results.

A numerical investigation of turbulent swirling flows in a circular pipe in the wake behind an axial fan was conducted by ĆOĆIĆ et al. (2013). The URANS approach with $k-\varepsilon$ and $k-\omega$ SST models was used together with LES computations and MILES approach for subgrid-scale modeling. It was found that for URANS simulations, the $k-\varepsilon$ model gives better prediction for mean axial velocity than $k-\omega$ SST model, while both give similar underprediction of mean circumferential velocity. LES computations gave better predictions, with trendlines captured accurately.

Javadi and Nilsson (2015) studied a series of numerical simulations in a highly swirling turbulent flow generated by a rotor-stator interaction in a swirl-generator. A diversity of URANS and URANS-LES turbulence models were used. In this situation, the RNG $k-\varepsilon$ and the standard $k-\varepsilon$ models were able to predict the recirculation region more realistic than the other models. However, the eddy-viscosity models predict the on-axis recirculation region longer and narrower than what is suggested by experimental results. The hybrid URANS-LES models predict the time-averaged velocity of the flow quite well.

Sorrentino et al. (2017) realized an experimental study and simulated a cyclonic lab-scale burner in a prismatic chamber shape operating with a high level of internal recirculation. The swirl is generated by two pairs of oxidant/fuel jets which feed the system in an anti-symmetric configuration, thus realizing a centripetal cyclonic flow. Inside the chamber, for numerical purposes, one can consider the configuration of the flow as co-flowing jets. For resolving the equations of transport, the RNG $k-\varepsilon$ turbulence model with swirl-dominated flow corrections was employed to account for high swirling degrees inside the combustor. Experimental results have demonstrated that a high dilution of the fresh mixture together with

large internal recirculation degrees may help reduce temperature increases. Also, the numerical model has shown a certain capability of predicting very similar trends of temperature and species production.

Ilie (2018) studied a turbulent swirling reacting flow with URANS (SST model) and LES (dynamic subgrid-scale model) approaches, using the same grid size for both. It could be concluded that the URANS method was quite dissipative and could not capture all the flow and combustion physics as well as LES does.

To account for swirl effects on passive scalar transport and turbulent mixing, Kadu et al. (2019) studied passive scalar mixing in coaxial jets under the influence of swirl using the Direct Numerical Simulation approach and compared to a non-swirling case. Concerning coaxial jets, the recirculation region that occurs by a strong degree of swirl decelerates the inner jet flow and recirculates the outer region fluid. Besides that, swirl increases the turbulence level and a higher turbulence intensity can be attributed to improved mixing and the promotion of entrainment of surrounding ambient fluid into the flow. This may be seen as a favorable characteristic for non-premixed confined combustion, since the entrained fluid, composed of heat products and unburned reactants, will improve combustion efficiency.

About mixing information, the mean and RMS fluctuations and turbulent fluxes of passive scalars all provide the necessary data. Johnson and Roback (1983) used these statistics to analyze the effects of swirl in a coaxial flow by introducing passive scalars through inner jet only and found that the spreading rate of scalars increases with an increase in swirling strength. Entropy may be also a parameter to analyze the diffusion of scalars Kadu et al. (2019).

For the results of the work of Kadu et al. (2019), the DNS simulations showed a good agreement for mean streamwise velocity and RMS streamwise velocity compared to experimental results. The case with intermediate swirling strength case exhibited a faster centerline decay and radial spread in the mean streamwise velocity in the downstream region compared to the non-swirling case. For the strong swirling case, an internal recirculation zone was formed. The mean scalar distribution presented a better spreading rate of scalars in the intermediate swirling case in the far downstream region, while the strong swirling case exhibited a maximum spread

far upstream. Furthermore, the introduction of swirl resulted in an increase in the entrainment rate, which made it easier for the ambient fluid to reach the centerline.

Rahman, Asrar and Khan (2019) investigated a stabilized isothermal turbulent swirling flow for a gas turbine combustion chamber which presents complex flow features such as bluff-body induced recirculation zone and vortex breakdown bubble. Among the standard, realizable, and RNG $k-\varepsilon$ model, the standard $k-\omega$ model, the Transition SST model, and a 7-equation stress-ω Reynolds Stress Model, the only model capable of predicting all flow features and meeting the convergence criteria was the standard $k-\varepsilon$.

2.6.2 Swirl effects on pollutant emissions

One of the main roles of applying swirling flow generation into combustion systems is the attempt to reduce pollutant emissions. Seeking to restrict emission requirements without affecting combustion efficiency, scientists and technologists are in a difficult situation, since enhancing combustion efficiency might conflict with approaches of decreasing pollutant emissions (LEFEBVRE, 1995).

The control of NO and CO emissions is an example of the difficulty faced by researchers. One of the most common ways of NO formation is the thermal mechanism, which is strongly dependent on temperature (it is unimportant below 1850 K) and is a slow process (LEFEBVRE, 1995). Important measures to decrease NO emission would be to reduce the temperature of the flame and to decrease the residence time. On the contrary, the production of CO is high at too low flame temperature, because the oxidation rate is low at low combustion temperatures (LEFEBVRE, 1995).

From the figure (2.7), to obtain low levels of CO and NO_x at the same time, the combustion temperature should be controlled in a strict zone, for example, between 1680 K and 1800 K.

The combustion conditions may also be controlled by the level of mixedness of the reactants. In a non-premixed flame, the fuel and the oxidizer are initially separated and the burning takes place only in the interface between those fluids, where mixing and reaction happen

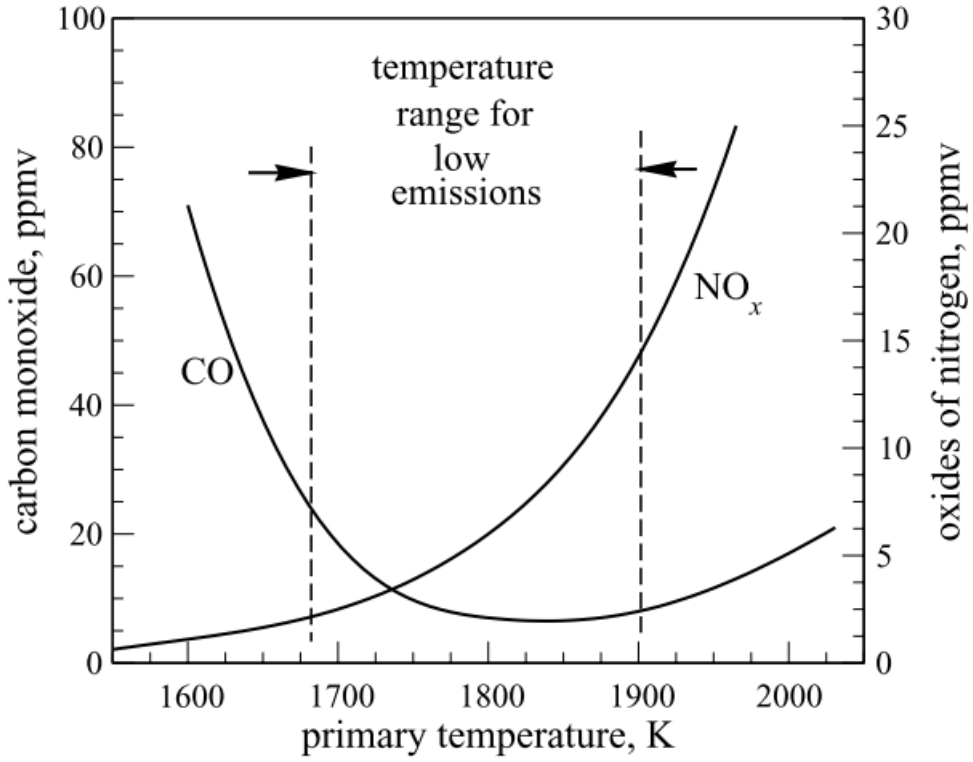

Figure 2.7 – Influence of temperature on NO_x and CO emissions. (LEFEBVRE, 1995)

at the same time. Before the reaction occurs, the fuel and oxidizer must be mixed on a macro scale by turbulent convection and then, mixed by molecular diffusion at a small scale. Since the entire mixing process demands time, it is considered a slow process compared to the premixed combustion. Therefore, it is more stable (WANG, 2005). One characteristic of non-premixed combustion is that the reaction always occurs around the stoichiometric surface, which makes the local peak temperature closed to the adiabatic one. This local temperature is generally higher than the threshold temperature, in which the NO_x production is high. Hence, non-premixed combustion might not be preferable for low emissions combustors (LEFEBVRE, 1995).

In a premixed flame, the fuel and the oxidizer are mixed at the molecular level before reaction and, thus, it is possible to control the equivalence ratio, reducing the temperature of flame below the threshold temperature. However, this configuration might present a flashback, when the flame propagates through the reactant mixture supply and enters the mixture tank, which may cause an explosion. This situation happens when the local flow velocity is lower than the local flame speed, for example, when the fuel flow is decreased or turned off Wang (2005).

Schmittel et al. (2000) investigated turbulent swirling flames in non-premixed combustion and discovered that swirl can reduce pollutant emissions, particularly that of nitrogen oxides. Under the swirl effect and, consequently, the mixing improvement of reactants, the flame temperature decreases, leading to a reduction of NO_x production. Besides that, when there is enough swirl intensity, increasing swirl number induces a reduction of residence time in hot areas, which limits the NO_x formation. Nevertheless, the swirl intensity must be in a compromise between the reduction of pollutant emission on one hand and the distance flame burner to prevent the flashback on the other hand.

The work of Coghe, Solero and Scribano (2004) on a lean natural gas burner demonstrated that NO_x reduction can achieve 30% for a swirl number between 0.7 and 0.82. Burguette and Costa (2006) analyzed the influence of the swirl intensity on NO_x emissions through the angles of the blades that constitute the swirler studied. It was found that the most important NO_x rate occurs at an angle of 45°; however, at a lower or higher value, NO_x emissions decrease. The authors explain that at 45° the recirculation zone appears, thus increasing the residence time close to the burner. Therefore, the intensity of combustion is increased, and consequently the temperature and NO_x formation.

From the study of NO_x emissions on a coaxial swirled natural gas flame by Cozzi and Coghe (2012), it was reported that the swirl intensity has a strong effect on non-premixed flames in which very low levels of NO_x emissions can be achieved at higher swirl levels.

From Boushaki et al. (2017) and Merlo et al. (2013), it was noted that swirl intensity might tend to enhance the mixing and to increase the residence time inside the reaction zone, which promotes the CO conversion to CO_2. It is also said that increasing the swirl number tends to reduce the NO_x formation in particular for oxygen rate up to 27%, which can be an effect of the flame temperature reduction by the swirl.

Therefore, to investigate the behavior of a non-reactive turbulent cyclonic flow inside a conceptual boiler using different closure models, a mathematical modeling is proposed in the next chapter, involving LES and URANS methodologies, besides mass fraction equations when different chemical species are present in the simulation.

Chapter 3

MATHEMATICAL MODELING

The numerical simulation of a CO boiler uses equations from the fluid mechanics to represent the physical phenomena inside the eulerian domain. When turbulence is involved, some closure methodologies are needed to solve the equations. In this chapter, these mathematical methodologies are discussed.

3.1 Direct Numerical Simulation to solve Turbulence

For a Newtonian fluid, the equations that constitute a turbulence model are the continuity and Navier-Stokes, represented by:

$$\frac{\partial \rho}{\partial t} + \frac{\partial u_i}{\partial x_i} = 0, \tag{3.1}$$

$$\frac{\partial \rho u_i}{\partial t} + \frac{\partial}{\partial x_j}\left(\rho u_i u_j\right) = -\frac{\partial p}{\partial x_i} + \frac{\partial}{\partial x_j}\left[\mu\left(\frac{\partial u_i}{\partial x_j} + \frac{\partial u_j}{\partial x_i} - \frac{2}{3}\frac{\partial u_k}{\partial x_k}\delta_{ij}\right)\right] + f_i, \tag{3.2}$$

in which ρ is the density, u the velocity, p the pressure, μ the dynamic viscosity, δ_{ij} the Kronecker delta and f_i, the force term.

From the equation (3.2), the term *diffusion of momentum* after the pressure gradient, which refers to kinematic viscosity $\nu = \mu/\rho$, came about due to the need to model molecular effects at the level of the continuum, by means of *Stokes closure model*. Despite being the best

model, at the level of the continuum, capable of solving turbulent flows, its use requires elevated mesh refinement and numerical-computational methods appropriate to the Direct Simulation Methodology (*DNS*).

This is because one of the main characteristics of turbulence is the multiplicity of turbulent structures depending on the Reynolds number, according to Kolmogorov Theory (KOLMOGOROV, 1941b). For a three-dimensional flow, the relationship between the characteristic lengths of the largest and the smallest swirling structures depends on the Reynolds value according to the expression:

$$\left(\frac{\ell_I}{\eta}\right)^3 = Re_{\ell_I}^{9/4}, \tag{3.3}$$

in which ℓ_I is the integral scale of turbulence, with which the order of magnitude of the size of the largest swirling structures of the flow is expressed. With the η scale, an order of magnitude of the smallest turbulent structures, called the Kolmogorov Scale, is obtained.

With the expression (3.3), we have the number of degrees of freedom of a dynamic system represented by a turbulent flow. Besides, it indicates the order of magnitude of the number of possible swirling structures, per volume unit ℓ_I^3, present in a turbulent flow.

It is also known that the differential model used for the simulation of fluid dynamics flows can only be solved using numerical methods, which, for the most part, require a mesh composed of finite volumes and that the physical volume that encompasses the problem must be discretized in its entirety. Also, for the correct description of a swirling structure of a characteristic size ℓ, a minimum of 4 to 120 finite volumes are required, depending on the method. Thus, the number of cells required to resolve all scales of a turbulent flow varies between 4 and 120 multiplied by $(ndf/m^3) \cdot (eulerianvolume)$, in which ndf = number of degrees of freedom.

Thus, considering that most engineering and industrial problems with turbulent flows involve high Reynolds numbers, the use of Direct Numerical Simulation is not feasible depending on the computational capacity available, given the need for a large number of finite volumes for the resolution of the smallest scales of turbulence.

To elucidate the difficulty of using the *DNS* methodology, one can consider the project of the present work, regarding a turbulent simulation inside an industrial cyclonic boiler. To simplify this example, the presence of immersed boundaries is disregarded so that refinements are not accounted for due to the presence of these structures and it is considered the use of only one fluid (air) to be drained into the boiler. Knowing that the Reynolds number of air flowing into the boiler is approximately $545,550$, the number of degrees of freedom present in the problem would be 8.10^{12}. Considering the volume of the Eulerian domain of approximately $770m^2$ and 8 cells to resolve all scales, the number of cells requested would be approximately 5.10^{16}, which would be unfeasible with the available computational resources. Also, considering a problem with hypotheses of a Newtonian fluid, incompressible, no thermal effects, LES as turbulence model, one chemical substance and with the Fractional Step method for the solution of the pressure-velocity coupling problem, there are four equations to be solved by volume, three related to the *momentum* for x, y and z coordinates and one for pressure. Thus, 2.10^{17} equations would be solved simultaneously.

As a curiosity, considering a good estimate of the *characteristic size* or *full scale* of the cyclonic swirling structure inside the boiler as the dimension of the base edge, of 8,584 m, the Kolmogorov's length scale would be on the order of 0.4 mm.

To circumvent the problem of the high computational cost for the solution of partial differential equations in a turbulent flow with a high Reynolds number, Boussinesq (1877) and Reynolds (1883), independently, proposed the decomposition of the flows into *mean flows* and *field fluctuations* in relation to their averages. Thus, the Boussinesq-Reynolds Averaged Equations are obtained.

3.2 Boussinesq-Reynolds' Averaged Equations

Boussinesq and Reynolds proposed the application of a *time-averaging* operator to the continuity and Navier-Stokes equations, represented here by the symbol $\langle\,\rangle$. Assuming a

solenoidal velocity field and a hypothesis of constant ρ for simplification, we have:

$$\frac{\partial \langle u_i \rangle}{x_i} = 0, \tag{3.4}$$

$$\frac{\partial}{\partial x_j}\left(\langle u_i u_j \rangle\right) = -\frac{1}{\rho_0}\frac{\partial \langle p \rangle}{\partial x_i} + \frac{\partial}{\partial x_j}\left[\nu\left(\frac{\partial \langle u_i \rangle}{\partial x_j} + \frac{\partial \langle u_j \rangle}{\partial x_i}\right)\right] + \frac{\langle f_i \rangle}{\rho_0}, \tag{3.5}$$

Were it not for the nonlinear term $\langle u_i u_j \rangle$, the equation (3.5) would already be able to be solved. The transported and unknown variables of the equations are $\langle u_i \rangle$ and the average pressure field $\langle p \rangle$. Thus, these equations cannot be solved, since it would be necessary to know the variable u_i using the *DNS* methodology (*Direct Numerical Simulation*). If in place of this nonlinear term, there was the term $\langle u_i \rangle \langle u_j \rangle$, the problem would already be solved. A mathematical device proposed by Boussinesq and Reynolds is to decompose the total velocity fields into mean and floating parts:

$$u_i = \langle u_i \rangle + u_i', \tag{3.6}$$

. As the mean of the pressure field appears in isolation in the equation (3.5), it does not require decomposition. Substituting the equation (3.6) in (3.5), we get:

$$\frac{\partial}{\partial x_j}\left(\left\langle \langle u_i \rangle \langle u_j \rangle \right\rangle + \left\langle u_i' \langle u_j \rangle \right\rangle + \left\langle \langle u_i \rangle u_j' \right\rangle + \langle u_i' u_j' \rangle\right) = \\ -\frac{1}{\rho_0}\frac{\partial \langle p \rangle}{\partial x_i} + \frac{\partial}{\partial x_j}\left[\nu\left(\frac{\partial \langle u_i \rangle}{\partial x_j} + \frac{\partial \langle u_j \rangle}{\partial x_i}\right)\right] + \frac{\langle f_i \rangle}{\rho_0}, \tag{3.7}$$

The following properties associated with the Time-averaging Operator are valid:

$$\langle u_i \rangle = \text{constant in time}, \tag{3.8}$$

$$\langle u_i' \rangle = \langle u_i \rangle - \left\langle \langle u_i \rangle \right\rangle = \langle u_i \rangle - \langle u_i \rangle = 0, \tag{3.9}$$

$$\left\langle \langle u_j \rangle \langle u_j \rangle \right\rangle = \langle u_j \rangle \langle u_j \rangle, \tag{3.10}$$

$$\left\langle u_i' \langle u_j \rangle + \langle u_i \rangle u_j' \right\rangle = \langle u_i' \rangle \langle u_j \rangle + \langle u_j' \rangle \langle u_i \rangle = 0. \tag{3.11}$$

According to the properties from (3.8) to (3.11), the equation (3.7) results in:

$$\frac{\partial}{\partial x_j}\left(\langle u_i\rangle\langle u_j\rangle + \langle u_i' u_j'\rangle\right) = -\frac{1}{\rho_0}\frac{\partial\langle p\rangle}{\partial x_i} + \frac{\partial}{\partial x_j}\left[\nu\left(\frac{\partial\langle u_i\rangle}{\partial x_j} + \frac{\partial\langle u_j\rangle}{\partial x_i}\right)\right] + \frac{\langle f_i\rangle}{\rho_0}, \tag{3.12}$$

Thus, the appearance of the Boussinesq-Reynolds $\langle u_i' u_j'\rangle$ Tensor is observed, which represents six additional unknowns due to the correlations between the speed fluctuations relative to the three coordinated directions. The tensor represents the entire change in the *momentum* between the middle part and the floating part of the turbulent flow.

With the appearance of this term, there is a need to model the transfer of information (*momentum*), which is non-linear by nature. This term represents non-linear information transfer processes of an advective-turbulent nature. However, for the sake of modeling and analogy to the information transfer process by molecular dynamics, they will be modeled as turbulent diffusive processes.

To exemplify such an analogy, one can consider a region of a flow with two fluids that flow at different speeds. The molecules of the fluid with the highest velocity transport the amount of momentum to the slowest region and it is this *momentum* transfer that is responsible for the acceleration of the region of the lowest speed. This liquid movement over the plane between the two regions of the flow is translated by viscous shear stress, modeled with the concept of molecular viscosity of the fluid.

Similarly, considering two regions of a flow with different levels of turbulent agitation, there is the presence of net flux of *momentum* over an imaginary plane. In an averaged flow, this flux will be modeled as turbulent stress, expressed by the Boussinesq-Reynolds Tensor.

The viscous stress tensor that appears in the Cauchy Equations was modeled by Stokes using the concept of molecular viscosity. In analogy to this model, Boussinesq proposed the modeling of the Boussinesq-Reynolds Tensor with the concept of turbulent viscosity (BOUSSINESQ, 1877).

Employing this analogy, the Boussinesq-Reynolds Tensor is transported from left to right in the equation (3.12) and incorporated into the molecular diffusion term for the *momentum*, this

equation is rewritten as:

$$\frac{\partial}{\partial x_j}\left(\langle u_i\rangle\langle u_j\rangle\right) = -\frac{1}{\rho_0}\frac{\partial\langle p\rangle}{\partial x_i} + \frac{\partial}{\partial x_j}\left[\nu\left(\frac{\partial\langle u_i\rangle}{\partial x_j} + \frac{\partial\langle u_j\rangle}{\partial x_i}\right) - \langle u_i' u_j'\rangle\right] + \frac{\langle f_i\rangle}{\rho_0}, \tag{3.13}$$

The equation (3.13) is called the *Reynols Averaged Navier-Stokes* (*RANS*). In addition to the continuity equation, it composes a model for obtaining an averaged behavior of a turbulent flow, without considering thermal effects in this context. However, additional closing models are required, as the term $\langle u_i' u_j'\rangle$ adds six unknowns, respectively, to be resolved.

3.3 Filtered Equations

The mean turbulence equations are useful for the solution of some engineering applications and situations with stationary fluid dynamics, however, the vast majority of problems remain insoluble, since they present a transient behavior. Examples are problems of fluid-structure interaction, calculations for climatic prediction, reactive combustion flows, among others. Thus, the decomposition of the flow into a mean and a floating part is still not enough to solve transient problems.

Smagorinsky (1963) proposed the decomposition of turbulent flows in lower and higher frequency bands. Signal filtering consists of using a cut-off frequency (f_c) to remove a filtered part $bar\phi(\vec{x},t)$ from information of a complete signal $\phi(\vec{x},t)$. Thus, the difference between the complete signal and the filtered part results in the fluctuating information:

$$\phi(\vec{x},t) = \bar{\phi}(\vec{x},t) + \phi'(\vec{x},t) \tag{3.14}$$

where the spectrum of the function $\phi(\vec{x},t)$ covers the entire possible frequency band.

The lowest frequencies band ($f < f_c$) is called the large structures or large scales band, while the highest frequencies band ($f \geq f_c$) is known as the small structures/scales band or sub-mesh scales band. The name *sub-mesh* comes from the fact that the cutoff frequency, f_c, is determined by the time step calculation and the cutoff wave number, k_c, by the size of the cells that make up the spatial discretization mesh. Thus, the cut-off frequency depends on the integration time Δt through the relationship $f_c = 2\pi/\Delta t$, while the integration volume ΔV helps

in determining the cutoff wave number through the relation $\vec{k}_c = 2\pi\left(\frac{1}{\Delta x}, \frac{1}{\Delta y}, \frac{1}{\Delta z}\right)$, according to mathematical formalism.

The procedure for filtering the equations is presented by:

$$\frac{\partial \bar{u}_i}{\partial x_i} = 0, \tag{3.15}$$

$$\frac{\partial \bar{u}_i}{\partial t} + \frac{\partial}{\partial x_j}(\overline{u_i u_j}) = -\frac{1}{\rho_0}\frac{\partial \bar{p}}{\partial x_i} + \frac{\partial}{\partial x_j}\left[\nu\left(\frac{\partial \bar{u}_i}{\partial x_j} + \frac{\partial \bar{u}_j}{\partial x_i}\right)\right] + \frac{\bar{f}_i}{\rho_0}, \tag{3.16}$$

These equations cannot be solved due to the term $\overline{u_i u_j}$, requiring the decomposition of the turbulence scales through the relation (3.14), resulting in the equation:

$$\frac{\partial \bar{u}_i}{\partial t} + \frac{\partial}{\partial x_j}(\overline{\bar{u}_i \bar{u}_j} + \overline{u_i' u_j'} + \overline{u_i' \bar{u}_j} + \overline{\bar{u}_i u_j'}) = -\frac{1}{\rho_0}\frac{\partial \bar{p}}{\partial x_i} + \frac{\partial}{\partial x_j}\left[\nu\left(\frac{\partial \bar{u}_i}{\partial x_j} + \frac{\partial \bar{u}_j}{\partial x_i}\right)\right] + \frac{\bar{f}_i}{\rho_0}, \tag{3.17}$$

This result, except for the presence of the transient terms, is the same obtained with the averaging process in the equation (3.7). In addition to the transient terms, what differentiates them is the difference between the properties of the filtering process and those of the averaging process. In the case of filtering, all statistical moments are different from zero, since the filtering of a fluctuation is not null, a filtered function is not a constant, and the filtering of the product of two filtered functions is different from the product of the two filtered variables. Thus, the following expressions are valid: $\overline{u_i' u_j'} \neq 0$, $\overline{u_i' \bar{u}_j} \neq 0$, $\overline{\bar{u}_i u_j'} \neq 0$, $\overline{\bar{u}_i \bar{u}_j} \neq \bar{u}_i \bar{u}_j$. Therefore, there is a higher number of unknowns compared to the averaging process, which also characterizes a turbulence closure problem.

The statistical moment $\overline{u_i' u_j'}$ is called the Boussinesq-Reynolds sub-mesh tensor. The term $\overline{u_i' \bar{u}_j} + \overline{\bar{u}_i u_j'}$ is the crossed sub-mesh tensor. These two terms must be modeled.

However, even with modeling, the term $\overline{\bar{u}_i \bar{u}_j}$ is still present in the equation (3.17), preventing its resolution. Thus, to obtain the term $\bar{u}_i \bar{u}_j$, Leonard et al. (1974) proposed the definitions:

$$L_{ij} = \overline{\bar{u}_i \bar{u}_j} - \bar{u}_i \bar{u}_j, \tag{3.18}$$

which defines Leonard's tensor. A term, proposed by Ferziger and Reynolds (1979), was also designed to make up the cross-correlations:

$$C_{ij} = \overline{u_i' \bar{u}_j} + \overline{\bar{u}_i u_j'}, \tag{3.19}$$

Substituting the equations of (3.18) to (3.19) in the equation (3.17), we obtain:

$$\frac{\partial \bar{u}_i}{\partial t} + \frac{\partial}{\partial x_j}(\bar{u}_i \bar{u}_j) = -\frac{1}{\rho_0}\frac{\partial \bar{p}}{\partial x_i} + \frac{\partial}{\partial x_j}\left[\nu\left(\frac{\partial \bar{u}_i}{\partial x_j} + \frac{\partial \bar{u}_j}{\partial x_i}\right) - \overline{u_i' u_j'} - C_{ij} - L_{ij}\right] + \frac{\bar{f}_i}{\rho_0}, \tag{3.20}$$

which represents the filtered function, but still not closed.

Germano (1986) defined the global sub-mesh tensor, which encompasses, in a τ_{ij} tensor, the Boussinesq-Reynolds $\overline{u_i' u_j'}$ tensor and the Crossed C_{ij} and Leonard's L_{ij} tensors.

The author proposed rewriting the tensor $\overline{u_i u_j}$, present in the equation (3.16), in order to obtain the term $\bar{u}_i \bar{u}_j$, by means of the relation:

$$\tau_{ij} = \overline{u_i u_j} - \bar{u}_i \bar{u}_j, \tag{3.21}$$

With the replacement of the equation (3.21) in (3.16), including the continuity equation, we have:

$$\frac{\partial \bar{u}_i}{\partial x_i} = 0, \tag{3.22}$$

$$\frac{\partial \bar{u}_i}{\partial t} + \frac{\partial}{\partial x_j}(\bar{u}_i \bar{u}_j) = -\frac{1}{\rho_0}\frac{\partial \bar{p}}{\partial x_i} + \frac{\partial}{\partial x_j}\left[\nu\left(\frac{\partial \bar{u}_i}{\partial x_j} + \frac{\partial \bar{u}_j}{\partial x_i}\right) - \tau_{ij}\right] + \frac{\bar{f}_i}{\rho_0}, \tag{3.23}$$

It is noteworthy that the Average Operator is the extreme of the filtering operator, in which all frequencies are filtered, resulting in an average behavior of the filtered signal.

These processes of averaging and filtering the equations are a mere mathematical formalism that results in the turbulence closure problem. However, at no time are they explicitly applied. The filtering process is carried out implicitly through space-time discretization, using a mesh of spatial volumes and a sequence of time steps. It is known that the variables within a discretization volume are considered constant and that the temporal evolution in the numerical-computational solution is obtained discretely. Thus, wavelengths, relative to the physical process, that are

smaller than the size of the cells, are not captured, as well as the characteristic times shorter than the time step.

Thus, when a differential equation is discretized, the discrete solution is filtered by the spatial grid and time step used.

When the limit of the filtering time tends to the total sampling time, we have the average Boussinesq-Reynolds equations. When this limit tends to the Kolmogorov Time Scale, the filtered equations tend to the Navier-Stokes equations, which require a direct numerical solution (DNS). Thus, it is concluded that the equations (3.22) and (3.23) are the most general forms for modeling turbulence. In this way, they can be used both for the URANS methodology (*Unsteady Reynolds Averaged Navier-Stokes*), as well as for the LES methodology (*Large Eddy Simulation*) and even for DNS.

Summarising, the URANS methodology is useful when looking for the transient behavior of turbulent flows, which can only be obtained with the use of the term τ_{ij}, modeling the transfer of *momentum*. It is a methodology that may be of difficult numerical-computational stability, but with the advantage of being able to be used with coarse spatial discretization meshes.

DNS methodology, on the other hand, is used when aiming at solving the entire spectrum of turbulent structures, from Integral Scales to Kolmogorov scales, to determine the complete velocity fields, density, and pressure. It is a methodology of a very refined spatial discretization mesh and very small time steps, determined by the Reynolds Number. Thus, it is limited, depending on the available computational resource, to flows with a low Re number.

Finally, in the LES methodology, large swirl structures are calculated directly, while the interaction between large and small structures is modeled using sub-mesh models. The more refined the spatial mesh and the shorter the time step, the larger the resolved band with fewer model interactions. For the convergence rate, it requires methods of spatial and temporal discretization of at least second order. The use of this methodology is sought when details of the solution are desired without being restricted to low Reynolds Number values.

3.4 URANS methodology and closure models

It is known that the equations of (3.22) and (3.23) are sufficient to model laminar or turbulent flows, for any value of the Reynolds Number and that, by being deduced by means of the filtering process, contain the global Boussinesq-Reynolds tensor, $\tau_{ij} = [\overline{u_i u_j} - \bar{u}_i \bar{u}_j][m^2/s^2]$. This term results in 6 more unknowns in the filtered equations, which characterizes an opened problem.

To solve this problem, Boussinesq (1877) proposed to close the system of filtered equations by modeling the Boussinesq-Reynolds tensor with the concept of turbulent viscosity $\nu_t(\vec{x}, t)$.

Therefore, by analogy to Stokes' model for viscous molecular stresses, Boussinesq proposed the following closure model for filtered equations:

$$-\tau_{ij} = \nu_t \left(\frac{\partial \bar{u}_i}{\partial x_j} + \frac{\partial \bar{u}_j}{\partial x_i} \right) - \frac{2}{3} k \delta_{ij}, \tag{3.24}$$

where

$$k \equiv \frac{1}{2}\tau_{ij} = \frac{1}{2}(\tau_{11} + \tau_{22} + \tau_{33}), \tag{3.25}$$

is the turbulent kinetic energy. Considering the predominance of the sub-mesh Boussinesq-Reynolds tensor, $\overline{u_i' u_j'}$, over the crossed tensor C_{ij} and the Leonard tensor L_{ij}, we have that $\tau_{ij} = \overline{u_i' u_j'}$, which makes k return to its classic definition:

$$k \equiv \frac{1}{2}\overline{u_i' u_j'} = \frac{1}{2}(\overline{u'^2} + \overline{v'^2} + \overline{w'^2}), \tag{3.26}$$

As turbulent kinematic viscosity is an inherent characteristic of flow, rather than fluid, it is more difficult to assess. The turbulent kinetic energy k is also unknown, but because it depends only on the Boussinesq-Reynolds tensor trace, it has a similar nature to pressure and, therefore, can be incorporated into its gradient.

With the replacement of the equation (3.24) in the equation (3.23), we have the Navier-Stokes equation prepared for the closing modeling:

$$\frac{\partial \bar{u}_i}{\partial t} + \frac{\partial}{\partial x_j}(\bar{u}_i \bar{u}_j) = -\frac{1}{\rho_0}\frac{\partial \bar{p}}{\partial x_i} + \frac{\partial}{\partial x_j}\left[(\nu + \nu_t)\left(\frac{\partial \bar{u}_i}{\partial x_j} + \frac{\partial \bar{u}_j}{\partial x_i}\right) - \frac{2}{3}k\delta_{ij}\right], \tag{3.27}$$

As the divergent of $\frac{2}{3}k\delta_{ij}$ is the gradient of this information,

$$\frac{\partial}{\partial x_j}\left(\frac{2}{3}k\delta_{ij}\right) = \frac{2}{3}\frac{\partial k}{\partial x_i}, \tag{3.28}$$

this term can be incorporated into the pressure, leading to:

$$\bar{p^*} = \bar{p} + \frac{2}{3}\rho_0 k, \tag{3.29}$$

$$\frac{\partial \bar{u}_i}{\partial t} + \frac{\partial}{\partial x_j}(\bar{u}_i \bar{u}_j) = -\frac{1}{\rho_0}\frac{\partial \bar{p}*}{\partial x_i} + \frac{\partial}{\partial x_j}\left[(\nu + \nu_t)\left(\frac{\partial \bar{u}_i}{\partial x_j} + \frac{\partial \bar{u}_j}{\partial x_i}\right)\right], \tag{3.30}$$

Were it not for the presence of ν_t, the equation would be closed. For the recovery of the true static pressure field, it is also necessary to model the turbulent kinetic energy, which must be done simultaneously with the calculation of the turbulent viscosity.

For the modeling of these terms, an analogy between molecular diffusion and turbulent diffusion processes is used. Through the kinetic theory of gases and the proposed analogy, $\nu_t \approx UL$ is considered, where U refers to the Transport Velocity Scale of the turbulent structures and L is the Scale Length of the turbulent structures. Also, the turbulent viscosity is considered to be an isotropic quantity, which does not match the characteristic of the turbulence of presenting high levels of anisotropy for large scales, but which can be realistic in modeling interactions with the smallest scales.

The turbulence closure models are classified according to the direct or indirect dependence on the concepts of turbulent viscosity and diffusivity.

The models that depend directly on the turbulent viscosity and diffusivity are models with zero balance equations, models with one balance equation, and models with two balance

equations. The models that independently or indirectly depend on these concepts are algebraic models and transport models of the components of the Boussinesq-Reynolds tensor or *Reynolds Stress Equation Model* (*RSM*).

Among the cited turbulent models, those which will be used following the URANS approach to solving the equations of the industrial problematic in this work are the standard $k-\varepsilon$, the modified $k-\varepsilon$ and the realizable $k-\varepsilon$, all being two-equation models.

3.4.1 k-ϵ Turbulence Models

Zero-equation and one-equation models are dependent on flow information besides initial and boundary conditions. Some examples are the Prandtl's Mixing Length Model, which requires the characteristic length of the flow to be known, varying for each case. Bradshaw (1974) presents a discussion about the possible origin of Prandtl's model, which is uncertain and possibly from 1925, including the first mentions to him and some difficulties that may be noted after some observations of experimental results. Also, there is the Prandtl-Reichardt model (PRANDTL, 1942), which has an empirical constant χ as a parameter. Seeking to circumvent the need for an empirical parameter and looking for a better model, Kolmogorov (1941a) proposed, in addition to the transport equation for turbulent kinetic energy k by Prandtl (1945), a transport equation for the Kolmogorov frequency scale ω_K. Following his idea, Chou (1945), Davydov (1961) and Harlow and Nakayama (1968) worked on the deduction of a transport equation, additional to k $[m^2/s^2]$, for the dissipation rate ε $[m^3/s^2]$, thus creating the $k-\varepsilon$ turbulence model. In a general way, the transport equations for k and ε may be written as:

$$\frac{\partial(\rho k)}{\partial t}+\frac{\partial(\rho\bar{u}_j k)}{\partial x_j}=\frac{\partial}{\partial x_j}\left[\left(\mu+\frac{\mu_t}{\sigma_k}\right)\frac{\partial k}{\partial x_j}\right]+f_k, \tag{3.31}$$

and

$$\frac{\partial(\rho\varepsilon)}{\partial t}+\frac{\partial(\rho\bar{u}_j \varepsilon)}{\partial x_j}=\frac{\partial}{\partial x_j}\left[\left(\mu+\frac{\mu_t}{\sigma_\varepsilon}\right)\frac{\partial \varepsilon}{\partial x_j}\right]+f_\varepsilon, \tag{3.32}$$

where f_k represents the ensemble of terms relative to the transformations of the turbulent kinetic

energy and f_ε concerns the terms relative to transformations of ε, while σ_k and σ_ε are constants of the URANS $k-\varepsilon$ model.

The turbulent dynamic viscosity as a function of k and ε is given by:

$$\mu_t = \rho \frac{C_\mu k^2}{\varepsilon}, \tag{3.33}$$

where C_μ is a parameter that may be constant or dynamic depending on the $k-\varepsilon$ model employed.

Hereafter, the parameters and transport equations will be detailed for the specific $k-\varepsilon$ models employed in this work.

3.4.1.1 Standard k-ε Turbulence Model

The standard $k-\varepsilon$ model was initially proposed by Launder and Spalding (1972). As time passed by, some modifications appeared, but they did not change significantly the process of deduction of the transport equations, keeping the original nomenclature. However, new variations of the original model were done related to the deduction of k and ε.

The standard $k-\varepsilon$ model consists of a semi-empirical model, capable of treating industrial problems with less computational effort, but in a robust manner and with reasonable accuracy. Therefore, the k and ε equations are obtained through empirical considerations. Mohammadi and Pironneau (1993) presented the necessary hypothesis for the demonstration of the equations.

Among the advantages of the standard $k-\varepsilon$ model, it can be said that its implementation is relatively simple, it does not demand a significant computational cost, its predictions are relatively good for a diversity of flows and the solutions are stable and converge easily.

However, some disadvantages are that it is not suitable for flows with high Reynolds numbers and it is inaccurate for swirling flows, jets, rapidly deformed flows, and fully developed flows in non-circular ducts. Besides, it requires the implementation of wall laws when the objective is to simulate near-wall flows (the k and ε equations are not valid in the internal region of the boundary layer) (MAGALHÃES, 2018). Also, it may be difficult to attribute boundary

conditions for k and ε, since they depend on experimental or statistical data.

The first equation of this model transports the turbulent kinetic energy, k $[m^2/s^2]$ and it is given by:

$$\frac{\partial(\rho k)}{\partial t} + \frac{\partial(\rho \bar{u}_j k)}{\partial x_j} = \frac{\partial}{\partial x_j}\left[\left(\mu + \frac{\mu_t}{\sigma_k}\right)\frac{\partial k}{\partial x_j}\right] + \mu_t S^2 - \rho\varepsilon \tag{3.34}$$

where ρ is the specific mass of the fluid, μ and μ_t are the molecular and turbulent dynamic viscosities, respectively, σ_k = 1.0 is a constant of the model and $S = \sqrt{2S_{ij}S_{ij}}$, in which S_{ij} represents the strain rate tensor components. The strain rate tensor is given by:

$$S_{ij} = \frac{1}{2}\left(\frac{\partial \bar{u}_i}{\partial x_j} + \frac{\partial \bar{u}_j}{\partial x_i}\right) \tag{3.35}$$

The second equation transports the dissipation rate, ε $[m^3/s^2]$ and it is given by:

$$\frac{\partial(\rho\varepsilon)}{\partial t} + \bar{u}_j\frac{\partial(\rho\varepsilon)}{\partial x_j} = \frac{\partial}{\partial x_j}\left[\left(\mu + \frac{\mu_t}{\sigma_\varepsilon}\right)\frac{\partial \varepsilon}{\partial x_j}\right] + C_{\varepsilon 1}\frac{\varepsilon}{k}\mu_t S^2 - \rho C_{\varepsilon 2}\frac{\varepsilon^2}{k} \tag{3.36}$$

where σ_ϵ = 1.3, $C_{\epsilon 1}$ = 1.44 and $C_{\epsilon 2}$ = 1.92 are the model constants.

From both k and ε equations, the first term represents the rate of change of k or ε in time, and the second being the transport of k or ε by advection. After the equality signal, there is the transport of k or ε by diffusion, the rate of production of k or ε minus the rate of destruction of k or ε.

The properties obtained through equations (3.34) and (3.36) are then used to calculate the turbulent dynamic viscosity, eq. (3.33).

As it can be noted, several constant parameters are used, which might not be seen as an interesting characteristic. To circumvent this issue, the realizable $k - \varepsilon$ model was proposed, which dynamically evaluates different parameters based on the velocity field of the flow. This approach enables this model to be applied in complex flows.

3.4.1.2 Realizable k-ε Turbulence Model

A new $k-\varepsilon$ model was proposed by Shih, Zhu and Lumley (1995), which consists of a new equation to model the dissipation rate and a new formulation for turbulent viscosity. The model is called realizable $k-\varepsilon$ and presents a more robust calculus of the Reynolds stress tensor compared to the Standard $k-\varepsilon$ model.

The new equation to model ε is based on the dynamic equation for vorticity fluctuation. The model coefficients were obtained through canonical flows, such as free shear flows and internal flows in channels.

The standard $k-\varepsilon$ is not suitable for flows with a high shear rate or adverse pressure gradient since it does not predict the turbulent viscosity accurately in these cases. Therefore, Shih, Zhu and Lumley (1995) mentions that this new model presents this improvement when compared to the standard one. From the authors' results, it may be noticed that the realizable model has a good performance in modeling complex turbulent flows, such as confined jets and flows over a step, and still presents the advantages of low computational cost need and robustness.

The equations for the realizable $k-\varepsilon$ model in an isothermal and incompressible context can be described by:

$$\frac{(\partial \rho k)}{\partial t} + \frac{(\rho \bar{u}_j k)}{\partial x_j} = \frac{\partial}{\partial x_j}\left[\left(\mu + \frac{\mu_t}{\sigma_k}\right)\frac{\partial k}{\partial x_j}\right] + \mu_t S^2 - \rho\varepsilon, \tag{3.37}$$

$$\frac{(\partial \rho \varepsilon)}{\partial t} + \frac{(\rho \bar{u}_j \varepsilon)}{\partial x_j} = \frac{\partial}{\partial x_j}\left[\left(\mu + \frac{\mu_t}{\sigma_\varepsilon}\right)\frac{\partial \varepsilon}{\partial x_j}\right] + \rho C_1 \sqrt{2} S_{ij} - \rho C_2 \frac{\varepsilon^2}{k + \sqrt{\nu\varepsilon}}, \tag{3.38}$$

where C_2 = 1.9, σ_k = 1.0 and σ_ε = 1.2.

While C_2 is a constant, C_1 is dynamically calculated through the expression:

$$C_1 = max\left[0.43, \frac{\Upsilon}{\Upsilon + 5}\right], \tag{3.39}$$

where

$$\Upsilon = S\frac{k}{\varepsilon}, \tag{3.40}$$

being $S = \sqrt{2S_{ij}S_{ij}}$.

One of the differences between the standard model and the realizable one is the approach to calculate the term C_μ. While this term is constant for the standard $k-\varepsilon$, it is dynamically valued for each time step based on other properties of the flow in the realizable model. According to Shih, Zhu and Lumley (1995), this term is calculated, then, by the expression:

$$C_\mu = \frac{1}{A_0 + A_S \cdot U^* \cdot \frac{k}{\varepsilon}}, \tag{3.41}$$

where

$$U^* = \sqrt{S_{ij}S_{ij} + \Omega_{ij}\Omega_{ij}}. \tag{3.42}$$

From the equation (3.41), A_0 = 4.04 and

$$A_S = \sqrt{6}cos(\phi_r), \tag{3.43}$$

and

$$\phi_r = \frac{1}{3}arccos(\sqrt{6}W_r). \tag{3.44}$$

The term W_r is given by:

$$W_r = \frac{S_{ij}S_{jk}S_{ki}}{\tilde{S}^3}, \tag{3.45}$$

where $\tilde{S} = \sqrt{S_{ij}S_{ij}}$, S_{ij} representing the strain rate tensor given by the eq. (3.35) and Ω_{ij} is the rotation rate tensor, given by:

$$\Omega_{ij} = \frac{1}{2}\left(\frac{\partial \bar{u}_i}{\partial x_j} - \frac{\partial \bar{u}_j}{\partial x_i}\right). \tag{3.46}$$

Therefore, one can say that the great difference between the standard $k-\varepsilon$ model and the realizable $k-\varepsilon$ model is the dynamic evaluation of the coefficients present in the transport equations of the dissipation rate and the calculus of the turbulent viscosity.

3.4.1.3 Standard k-ε for swirling flows

For swirling flows modeling, it is well-known that URANS models present some deficiencies due to Boussinesq's hypothesis. In special, some researches about the standard $k-\varepsilon$ model showed a poor performance in predicting swirling and vortex flows (ARMFIELD; FLETCHER, 1989; KAYA; KARAGOZ, 2008). For such cases, it would be more suitable to use models that consider the Reynolds tensor without the use of the concept of turbulent viscosity. Therefore, one alternative would be the Reynolds Stress Model (RSM). Despite being the most appropriate model for predicting swirling flows, it presents some disadvantages, such as a high computational cost when compared to two-equation models, due to a minimum of seven additional transport equations that have to be resolved. It should be also pointed out that the model might be unstable.

The $k-\varepsilon$ models are stable, but not accurate for rotational flows. Concerning this deficiency, some modifications have been proposed to enhance its performance (SAQR et al., 2009).

One of these modifications was presented by Durbin (1996) and has the objective of improving the calculus in stagnation regions, known as the standard $k-\varepsilon$ modified model. According to the author, there is an excessive presence of turbulent kinetic energy in the vicinity of stagnation points. Thus, it was proposed a modification of the source term of the ε equation (3.32) and the calculus of the dynamic turbulent viscosity:

$$S_\varepsilon = C_{\varepsilon 1}\mu_t S^2\frac{\varepsilon}{k} - C_{\varepsilon 2}\rho\frac{\varepsilon^2}{k} = C_{\varepsilon 1}\mu_t S^2\frac{1}{\Gamma} - C_{\varepsilon 2}\rho\frac{\varepsilon}{\Gamma} \tag{3.47}$$

$$\mu_t = C_\mu \rho \frac{k^2}{\varepsilon} = C_\mu \rho k \Gamma \tag{3.48}$$

in which $\Gamma = k/\varepsilon$.

Durbin proposed that Γ might be represented by the minimum of two relations:

$$\Gamma = min\left(\frac{k}{\varepsilon}, \frac{2}{3C_\mu}\sqrt{\frac{3}{8S^2}}\right) \tag{3.49}$$

This modification might give good representations of swirl phenomena since there is the presence of stagnation points in the center of rotational structures.

3.5 Large Eddy Simulations (LES)

It is a methodology intermediate in relation to the Direct Numerical Simulation and the RANS/URANS methodology. Its main role is to separate the scales that will be calculated, which are above the filter applied, while the smaller scales are modeled, named as subgrid scales. It is through an appropriate model that these scales will be taken into account, transferring the energy between the resolved scales and the unresolved ones. It is important to point that the large structures are responsible for characterizing the flow and transporting most of the energy, while the smallest structures are universal and isotropic.

The section 3.3, concerning filtered equations, gave an introduction to the LES methodology, letting clear the process of filtering. From this process, a filtered product of unknown variables is generated and decomposed in scales, explicit in the equation (3.17). That is when the advective term appears in function of the Boussinesq-Reynolds' subgrid tensor $\overline{u_i' u_j'}$, the Leonard's and Crossed tensors, eq. (3.18) and (3.19). Shaanan, Ferziger and Reynolds (1975) and Neto et al. (1993) proposed that the Leonard's and crossed tensors do not need to be modeled separately in situations when it is used at maximum a third order scheme for the advective term. The justificative is that the numerical value of both terms is smaller than the subgrid Reynolds tensor. Then, Germano (1986) defined the global subgrid tensor, τ_{ij}, eq. (3.21), encompassing

the Boussinesq-Reynolds', the Leonards' and the Crossed tensors. Finally, the filtered equation may be rewritten as in eq. (3.23), emphasized again in this section by the equation:

$$\frac{\partial \bar{u}_i}{\partial t} + \frac{\partial}{\partial x_j}(\bar{u}_i \bar{u}_j) = -\frac{1}{\rho_0}\frac{\partial \bar{p}}{\partial x_i} + \frac{\partial}{\partial x_j}\left[\nu\left(\frac{\partial \bar{u}_i}{\partial x_j} + \frac{\partial \bar{u}_j}{\partial x_i}\right) - \tau_{ij}\right] + \frac{\bar{f}_i}{\rho_0}, \tag{3.50}$$

In order to solve this indeterminacy, it may be used Boussinesq's hypothesis, as expressed in URANS section 3.4 by the eq. (3.24).

3.5.1 Smagorinsky Model

With the application of Boussinesq's hypothesis, the closure problem is diminished to the determination of the turbulent viscosity scalar, ν_t, as a function of the variables of the resolved field. It is related to the hypothesis of the small structures in balance with the production and dissipation of the subgrid turbulent kinetic energy. The turbulent viscosity can also be considered proportional to the subgrid characteristic length scale, Δ, and to the subgrid characteristic velocity scale, $k_{sgs}^{1/2}$. Thereby, Smagorinsky (1963) proposed an algebraic model, described by the equation:

$$\nu_t = (C_s \Delta)^2 \sqrt{2\overline{S_{ij} S_{ij}}}, \tag{3.51}$$

in which C_s is the Smagorinsky coefficient and Δ is the length scale associated with the spatial filter (grid spacing). The Smagorsinky coefficient is calibrated for each sort of flow, varying for each situation. For example, in a case for isotropic homogeneous turbulence, Lilly (1966) determined a value of $C_s = 0.18$ as acceptable, even though practical cases accept a range of $0.05 \leq C_s \leq 0.30$. Salvo, Souza and Martins (2018) used LES to simulate a swirling flow in an industrial cyclone separator with a Smagorinsky coefficient of 0.1, for example.

The Smagorinsky model proved to be a simple, robust model and free of numerical instabilities, which allows it to be applied in a diversity of situations Damasceno (2012).

3.6 Multi-component modeling

The context of a multi-component turbulent swirling flow simulation demands the approach of modeling the equation of mass conservation of species. According to Poinsot and Veynante (2005), species are characterized through their mass fractions, Y_k, for $k = 1\ to\ N$, where N means the number of species in a mixture. Then, the mass fractions are defined as:

$$Y_k = \frac{m_k}{m}, \tag{3.52}$$

where m_k is the mass of species k in a certain volume V and m is the total mass of fluid in this volume.

The mass conservation equation for species k is given by:

$$\frac{\partial \rho Y_k}{\partial t} + \frac{\partial}{\partial x_i}(\rho(u_i + V_{k,i})Y_k) = \dot{\omega}_k \quad \text{for} \quad k = 1, N, \tag{3.53}$$

where $V_{k,i}$ is the i-component of the diffusion velocity V_k of species k and $\dot{\omega}_k$ is the reaction rate of species k. For non-reactive flows, $\dot{\omega}_k = 0$, and by definition:

$$\sum_{k=1}^{N} Y_k V_{k,i} = 0 \tag{3.54}$$

The diffusion velocity $V_{k,i}$ is obtained through a simplified approach based on Fick's law:

$$V_{k,i} Y_k = -D_k \frac{\partial Y_k}{\partial x_i}, \tag{3.55}$$

where D_k is the diffusion coefficient of species k into the mixture. Then, the equation for conservation of species becomes:

$$\frac{\partial \rho Y_k}{\partial t} + \frac{\partial \rho u_i Y_k}{\partial x_i} = \frac{\partial}{\partial x_i}\left(\rho D_k \frac{\partial Y_k}{\partial x_i}\right) \tag{3.56}$$

When dealing with turbulent flows, balance equations for URANS and LES and filtering approaches may influence the equations of chemical species. When in URANS approaches, in constant density flows, Reynolds averaging induces splitting any quantity f into a mean, $\bar{f}$, and a fluctuating part, f', components ($f = \bar{f} + f'$). Using this procedure, the mass conservation equation leads to:

$$\frac{\partial \bar{\rho}}{\partial t} + \frac{\partial}{\partial x_i}(\overline{\rho u_i}) = \frac{\partial \bar{\rho}}{\partial t} + \frac{\partial}{\partial x_i}(\bar{\rho}\bar{u}_i + \overline{\rho' u_i'}) = 0 \tag{3.57}$$

The unclosed quantity $\overline{\rho' u_i'}$ related to a correlation between density and velocity fluctuations needs modeling. It is strange to think that this term acts as a mass source term for the mean flow field ($\bar{\rho}, \bar{u}_i$), showing that the average mass flow rates using Reynolds averaging may not be a conserved quantity in a steady flow (POINSOT; VEYNANTE, 2005). For variable density flows, Reynolds averaging introduces more unclosed correlations between any quantity f and density fluctuations ($\overline{\rho' f'}$). In order to avoid this complication, it might be preferred to use the mass-weighted averages or Favre averages (FAVRE, 1969):

$$\tilde{f} = \frac{\overline{\rho f}}{\bar{\rho}} \tag{3.58}$$

From this Favre average, any quantity f may be split into mean and fluctuating components as:

$$f = \tilde{f} + f'' \quad with \quad \tilde{f''} = 0 \tag{3.59}$$

When simulating a flow with different species and densities, its fluctuations have to be considered in a transient behavior during some time. With this approach, it has to be considered the conservative form of the equations of the problem and so, the averaged balance equations are described as:

- Mass conservation:

$$\frac{\partial \bar{\rho}}{\partial t} + \frac{\partial}{\partial x_i}(\bar{\rho}\tilde{u}_i) = 0 \tag{3.60}$$

- Navier-Stokes equation:

$$\frac{\partial \bar{\rho}\tilde{u}_i}{\partial t} + \frac{\partial}{\partial x_j}(\bar{\rho}\tilde{u}_i\tilde{u}_j) = -\frac{\partial \bar{p}}{\partial x_j} + \frac{\partial}{\partial x_i}\left[(\mu + \mu_t)\left(\frac{\partial \tilde{u}_i}{\partial x_j} + \frac{\partial \tilde{u}_j}{\partial x_i} - \frac{2}{3}\frac{\partial \tilde{u}_k}{\partial x_k}\delta_{ij}\right) - \frac{2}{3}\bar{\rho}k\delta_{ij}\right] \quad (3.61)$$

where k is the kinetic energy and δ_{ij} is the Kronecker symbol.

- Mass conservation of chemical species:

$$\frac{\partial(\bar{\rho}\tilde{Y}_k)}{\partial t} + \frac{\partial}{\partial x_i}(\bar{\rho}\tilde{u}_i\tilde{Y}_k) = \frac{\partial}{\partial x_i}\left(\bar{\rho}\bar{D}_k\frac{\partial \tilde{Y}_k}{\partial x_i} - \bar{\rho}\widetilde{u_i''Y_k''}\right) \quad for \quad k = 1, N \quad (3.62)$$

The flux represented by the term $\bar{\rho}\widetilde{u_i''Y_k''}$ is closed using a classical gradient assumption cited by Poinsot and Veynante (2005) :

$$\bar{\rho}\widetilde{u_i''Y_k''} = -\frac{\mu_t}{Sc_{kt}}\frac{\partial \tilde{Y}_k}{\partial x_i} \quad (3.63)$$

where Sc_{kt} is a turbulent Schmidt number for species k. This term represents the ratio of momentum diffusivity to mass diffusivity in a turbulent flow and its value may vary depending on the fluids present in the flow. No universally accepted values of this parameter have been established, but, depending on the chemical species involved, the values are much lower in the air when compared to a system in water. Gualtieri et al. (2017) presented some values of this parameter, the best fitting situated in the range from 0.1 to 1. The value used in the present work is 0.7, as well as in the work of Gonçalves, Magalhães and Vedovoto (2020).

After describing the equations that will be used to represent a turbulent swirling flow inside an industrial chamber, it is relevant to understand the numerical methods implemented in the code MFSim that make it possible to solve this system of complex equations.

Chapter 4

NUMERICAL MODELING

In the present chapter, the main numerical strategies used to solve the transport equations defined in the Mathematical Modeling chapter will be presented. The simulations of this research were conducted with the software MFSim, an in-house code developed at the Fluid Mechanics Laboratory (MFLab) at the Federal University of Uberlândia. It is a code based on discretization in finite volumes and adaptive block-structured regular and cartesian mesh which aids in reducing the computational cost. Also, the code provides solutions for simulations of fluid-structure, multi-phase, reactive, and turbulent flows with Large Eddy Simulation (LES), Unsteady Reynolds Averaged Navier-Stokes (URANS), and also hybrid methods, considering 3D domains and parallel processing (GASCHE; BARBI; VILLAR, 2012; DENNER et al., 2014; MELO et al., 2018; NETO et al., 2019). It has some temporal and advective discretization schemes and the possibility of using the SIMPLE method or Fractional Step method for the pressure-velocity coupling. The temporal integration is semi-implicit, in which the diffusive term of the equations is solved implicitly while the advective and pressure terms are treated explicitly. The linear systems resulting for velocity and transport equations for turbulence closure are solved using the multigrid-multilevel method. For the actual work, it has been highlighted the use of the immersed boundary method to account for lagrangian structures inside an eulerian domain as well as the adaptive refinement, discretization methods, pressure-velocity coupling, algorithms for upgrading physical properties of chemical species, and so on.

4.1 Spacial Discretization of Transport Equations

The transport equations described in the Mathematical Modeling chapter must be discretized in space and time in order to be solved numerically. In the present work, the discretizations concern the Navier-Stokes and scalar transport equations. The Navier-Stokes equations in the vectorial form are used to demonstrate the methodology:

$$\frac{\partial}{\partial t}\int_{\Omega}(\rho\vec{V})d\Omega + \int_{S}\rho\vec{V}(\vec{V}\cdot\vec{n})dS = \int_{S}\underline{\underline{T}}\cdot\vec{n}dS + \int_{\Omega}\rho\vec{b}d\Omega, \tag{4.1}$$

where $\vec{V}$ is the velocity vector, $\vec{n}$ denotes the vector normal to the surface where the fluid enters or leaves, $\vec{b}$ is the field force vector and $\underline{\underline{T}}$ is represents the total stress tensor, defined as:

$$\underline{\underline{T}} = \underline{\underline{\tau}} - p\underline{\underline{I}}, \tag{4.2}$$

where $\underline{\underline{\tau}}$ is the viscous stress tensor, p is the pressure over the volume of fluid and $\underline{\underline{I}}$ is the unity tensor. To demonstrate the spatial discretization of equations, it is simpler to consider the equation (4.1) in steady state, while the transient part will be explained when it is more convenient. Therefore, the equation to be discretized is:

$$\int_{S}\rho\vec{V}(\vec{V}\cdot\vec{n})dS = \int_{S}\underline{\underline{\tau}}\cdot\vec{n}dS - \int_{S}p\underline{\underline{I}}\cdot\vec{n}dS + \int_{\Omega}\rho\vec{b}d\Omega, \tag{4.3}$$

The surface integrals from equation (4.3) are the sum of the integrals over the 6 faces of a control volume:

$$\int_{S} f dS = \sum_{k=1}^{6}\int_{S_k} f dS, \tag{4.4}$$

the f being the component of a diffusive or advective flux vector in the normal direction to the face of the control volume. A control volume with the dimensions Δx, Δy and Δz is illustrated in figure (4.1). The letters in uppercase in the figure represent central positions in this volume, while the letters in lowercase are related to positions over its faces.

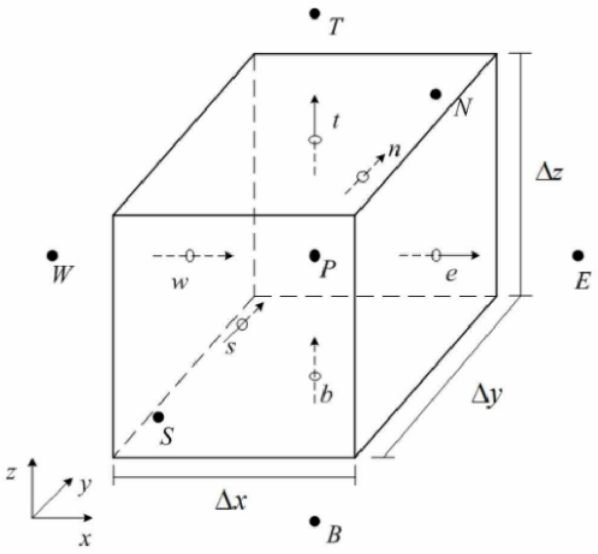

Figure 4.1 – Representation of a control volume (DAMASCENO et al., 2018)

The letters e, w, n, s, t and b as well as its representations in uppercase identify the positions *east*, *west*, *north*, *south*, *top* and *bottom* in relation to the point P, the position in the center of the volume.

Considering that only the nodal values (at the center of the control volume) are calculated, there is no information about the other positions over the surface S_k to calculate the surface integrals. Therefore, an approximation is made considering the integral as the product of the information at the center of the face and its area:

$$\int_{S_k} f dS = \bar{f}_k S_k \approx f_k S_k \tag{4.5}$$

For the volume integrals, it is considered the product between the mean value of the term being integrated and the volume of the control volume, defining the substitution as the value of the center of this volume:

$$\int_{\Omega} q d\Omega = \bar{q} \Delta\Omega \approx q_P \Delta\Omega, \tag{4.6}$$

where q is the product between the field force and the density. From the application of these methodologies, the resulting equations for the velocity u are:

$$(\rho uu|_e - \rho uu|_w)\Delta y\Delta z + (\rho vu|_n - \rho vu|_s)\Delta x\Delta z + (\rho wu|_t - \rho wu|_b)\Delta x\Delta y =$$
$$\left\{\mu\left[2\frac{\partial u}{\partial x} - \frac{2}{3}\left(\frac{\partial u}{\partial x} + \frac{\partial v}{\partial y} + \frac{\partial w}{\partial z}\right)\right]\Big|_e - \mu\left[2\frac{\partial u}{\partial x} - \frac{2}{3}\left(\frac{\partial u}{\partial x} + \frac{\partial v}{\partial y} + \frac{\partial w}{\partial z}\right)\right]\Big|_w\right\}\Delta y\Delta z$$
$$+\left[\mu\left(\frac{\partial v}{\partial x} + \frac{\partial u}{\partial y}\right)\Big|_n - \mu\left(\frac{\partial v}{\partial x} + \frac{\partial u}{\partial y}\right)\Big|_s\right]\Delta x\Delta z +$$
$$\left[\mu\left(\frac{\partial w}{\partial x} + \frac{\partial u}{\partial z}\right)\Big|_t - \mu\left(\frac{\partial w}{\partial x} + \frac{\partial u}{\partial z}\right)\Big|_b\right]\Delta x\Delta y - (p|_e - p|_w)\Delta y\Delta z + \rho b_x\Delta x\Delta y\Delta z \quad (4.7)$$

Dividing the equation by an elementary volume $(\Delta x\Delta y\Delta z)$:

$$\frac{\rho uu|_w^e}{\Delta x} + \frac{\rho vu|_s^n}{\Delta y} + \frac{\rho wu|_b^t}{\Delta z} = -\frac{p|_w^e}{\Delta x} + \frac{1}{\Delta x}\left\{\mu\left[2\frac{\partial u}{\partial x} - \frac{2}{3}\left(\frac{\partial u}{\partial x} + \frac{\partial v}{\partial y} + \frac{\partial w}{\partial z}\right)\right]\Big|_w^e\right\} +$$
$$\frac{1}{\Delta y}\left[\mu\left(\frac{\partial v}{\partial x} + \frac{\partial u}{\partial y}\right)\Big|_s^n\right] + \frac{1}{\Delta z}\left[\mu\left(\frac{\partial w}{\partial x} + \frac{\partial u}{\partial z}\right)\Big|_b^t\right] + \rho b_x \quad (4.8)$$

By analogy, the equations for v and w are described as:

$$\frac{\rho uv|_w^e}{\Delta x} + \frac{\rho vv|_s^n}{\Delta y} + \frac{\rho wv|_b^t}{\Delta z} = -\frac{p|_s^n}{\Delta y} + \frac{1}{\Delta x}\left[\mu\left(\frac{\partial u}{\partial y} + \frac{\partial v}{\partial x}\right)\Big|_w^e\right] +$$
$$\frac{1}{\Delta y}\left\{\mu\left[2\frac{\partial v}{\partial y} - \frac{2}{3}\left(\frac{\partial u}{\partial x} + \frac{\partial v}{\partial y} + \frac{\partial w}{\partial z}\right)\right]\Big|_s^n\right\} + \frac{1}{\Delta z}\left[\mu\left(\frac{\partial w}{\partial y} + \frac{\partial v}{\partial z}\right)\Big|_b^t\right] + \rho b_y \quad (4.9)$$

and

$$\frac{\rho uw|_w^e}{\Delta x} + \frac{\rho vw|_s^n}{\Delta y} + \frac{\rho ww|_b^t}{\Delta z} = -\frac{p|_b^t}{\Delta z} + \frac{1}{\Delta x}\left[\mu\left(\frac{\partial u}{\partial z} + \frac{\partial w}{\partial x}\right)\Big|_w^e\right] + \frac{1}{\Delta y}\left[\mu\left(\frac{\partial v}{\partial z} + \frac{\partial w}{\partial y}\right)\Big|_s^n\right] +$$
$$\frac{1}{\Delta z}\left\{\mu\left[2\frac{\partial w}{\partial z} - \frac{2}{3}\left(\frac{\partial u}{\partial x} + \frac{\partial v}{\partial y} + \frac{\partial w}{\partial z}\right)\right]\Big|_b^t\right\} + \rho b_z. \quad (4.10)$$

For the mass conservation equation, the discretization results in:

$$\frac{u_e - u_w}{\Delta x} + \frac{v_n - v_s}{\Delta y} + \frac{w_t - w_b}{\Delta z} = 0, \quad (4.11)$$

Through linear interpolations, the pressure and the diffusive and advection terms are determined. The obtained transported variables by the advective fluxes such as u, v, w or any scalar ϕ will be soon described.

A brief explanation of the linear interpolation can be given with the auxiliary of the figure (4.2), which illustrates a two-dimensional mesh.

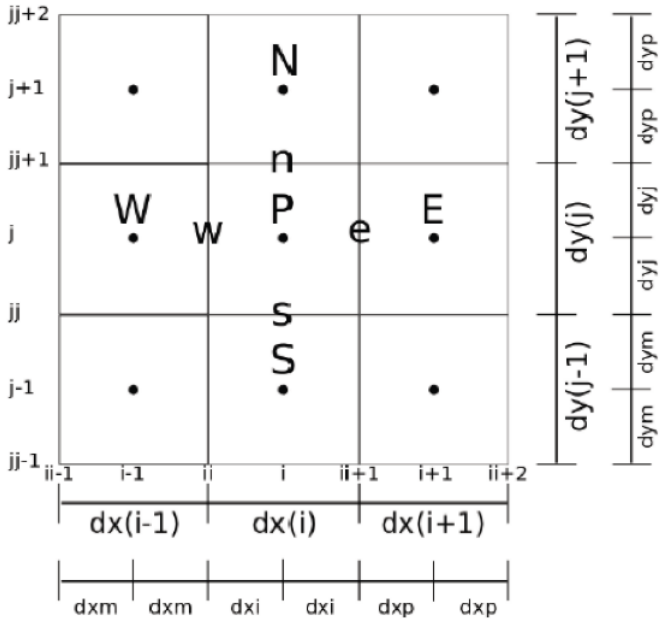

Figure 4.2 – Two-dimensional representation of a control volume mesh (DAMASCENO et al., 2018)

The calculus of the scalar ϕ (situated in the center of a control volume) through linear interpolation is given by:

$$\phi_e = \phi_E \lambda_e + \phi_P (1 - \lambda_e), \tag{4.12}$$

in which λ is a linear interpolation factor, defined as:

$$\lambda_e = \frac{x_e - x_P}{x_E - x_P} = \frac{dx_i}{dx_i + dx_p} \tag{4.13}$$

Knowing that for the simulations of this project, the applied mesh is uniform, then

$dx_i = dx_p$, resulting in:

$$\lambda_e = \frac{dx_i}{dx_i + dx_i} = \frac{1}{2} \tag{4.14}$$

Therefore,

$$\phi_e = \phi_E \frac{1}{2} + \phi_P \left(1 - \frac{1}{2}\right) = \frac{\phi_E + \phi_P}{2}. \tag{4.15}$$

Concerning the transported variables by the advective flux terms, the equation (4.16) represents a starting point in cartesian coordinates:

$$\frac{\partial}{\partial x_j}(\rho u_j \phi) = \frac{\partial}{\partial x}(\rho u \phi) + \frac{\partial}{\partial y}(\rho v \phi) + \frac{\partial}{\partial z}(\rho w \phi), \tag{4.16}$$

where ϕ is the variable to be transported (e.g. velocity, passive scalar, temperature).

The transported variable can even be normalized, according to Gaskell and Lau (1988) and Leonard (1991):

$$\hat{\phi} = \frac{\phi - \phi_U}{\phi_D - \phi_U}, \tag{4.17}$$

where U and D are related to the upstream and downstream cells in relation to the cell to be determined P. The figure (4.3) illustrates the terms and local variables described in the normalization of ϕ.

The normalized coordinates are defined as:

$$\hat{\xi_P} = \frac{\xi_P - \xi_U}{\xi_D - \xi_U} \tag{4.18}$$

and

$$\hat{\xi_f} = \frac{\xi_f - \xi_U}{\xi_D - \xi_U}. \tag{4.19}$$

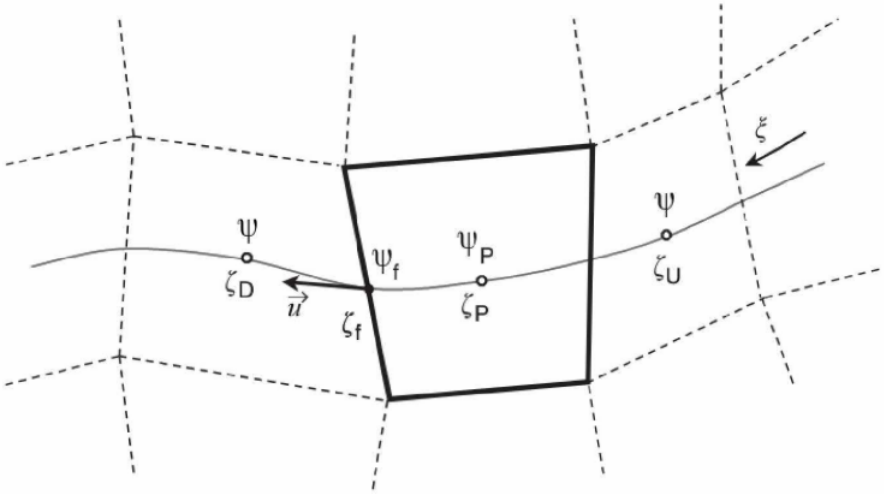

Figure 4.3 – Local variables and normalized coordinate system. Adapted from (ALVES; OLIVEIRA; PINHO, 2003)

From these definitions, the CUBISTA (*Convergent and Universally Bounded Interpolation Scheme for Treatment of Advection*) scheme, used in the actual work, may be described:

$$\hat{\phi}_f = \begin{cases} \left[1 + \frac{\hat{\xi}_f - \hat{\xi}_P}{3(1-\hat{\xi}_P)}\right] \frac{\hat{\xi}_f}{\hat{\xi}_P} \hat{\phi}_P, & 0 < \hat{\phi}_P < \frac{3}{4}\hat{\xi}_P \\ \frac{\hat{\xi}_f(1-\hat{\xi}_f)}{\hat{\xi}_P(1-\hat{\xi}_P)} \hat{\phi}_P + \frac{\hat{\xi}_f(\hat{\xi}_f - \hat{\xi}_P)}{1-\hat{\xi}_P}, & \frac{3}{4}\hat{\xi}_P \leq \hat{\phi}_P \leq \frac{1+2(\hat{\xi}_f - \hat{\xi}_P)}{2\hat{\xi}_f - \hat{\xi}_P}\hat{\xi}_P \\ 1 - \frac{1-\hat{\xi}_f}{2(1-\hat{\xi}_P)}(1 - \hat{\phi}_P), & \frac{1+2(\hat{\xi}_f - \hat{\xi}_P)}{2\hat{\xi}_f - \hat{\xi}_P}\hat{\xi}_P < \hat{\phi}_P < 1 \\ \hat{\phi}_P, & to\ the\ rest. \end{cases} \tag{4.20}$$

4.2 Temporal Integration

For the temporal integration of the equations discretized in space, it has been used the Implicit-Explicit method (IMEX) named *Semi-implicit Backward Differentiation Formula* (SBDF) presented by Ascher, Ruuth and Wetton (1995). This approach enables the advective and diffusive terms to be treated in explicit and implicit ways, respectively. It is important to treat the advective term in an explicit form in order to facilitate the solution of a non-linear system, while the implicit method for the diffusive term avoids the need for a very restricted time step.

The use of this methodology makes the time step to be based only on the advective term,

resulting in:

$$\Delta t = C \left(\frac{1}{t_{adv}} \right)^{-1}, \tag{4.21}$$

where C is the CFL condition defined between 0 and 1 (COURANT; FRIEDRICHS; LEWY, 1967) and t_{adv} is defined as:

$$t_{adv} = \frac{\Delta x}{|u|_{max}} + \frac{\Delta y}{|v|_{max}} + \frac{\Delta z}{|w|_{max}}, \tag{4.22}$$

in which Δx, Δy and Δz refer to the mesh discretization length in the directions x, y and z, respectively. $|u|_{max}$, $|v|_{max}$ and $|w|_{max}$ symbolize the maximum values of the velocities u, v and w.

The IMEX method applied in the present work is a second-order method, which implies the necessity of a three times stencil, two prior to what is seeked, t^{n-1} and t^n and the actual time t^{n+1}. Therefore, they are defined as $\Delta t^n = t^n + t^{n-1}$ and $\Delta t^{n+1} = t^{n+1} - t^n$. The following expression concerns the general second order scheme with variable time step (DAMASCENO et al., 2018):

$$\frac{\alpha_2 u^{n+1} + \alpha_1 u^n + \alpha_0 u^{n-1}}{\Delta t^{n+1}} = \theta_2 f(u)^{n+1} + \theta_1 f(u)^n + \theta_0 f(u)^{n-1} + \beta_1 g(u)^n + \beta_0 g(u)^{n-1}, \tag{4.23}$$

in which the functions g and f represent the advective and diffusive terms, respectively. The parameters α_i, β_i and θ_i are defined as:

$$\alpha_0 = \frac{(2\gamma - 1)\omega_{n+1}^2}{1 + \omega_{n+1}}, \qquad \alpha_1 = (1 - 2\gamma)\omega_{n+1} - 1, \qquad \alpha_2 = \frac{1 + 2\gamma\omega_{n+1}}{1 + \omega_{n+1}},$$
$$\beta_0 = -\gamma\omega_{n+1}, \qquad \beta_1 = 1 + \gamma\omega_{n+1}, \qquad \theta_0 = \frac{c}{2}, \qquad \theta_1 = 1 - \gamma - \left(1 + \frac{1}{\omega_{n+1}}\right)\frac{c}{2},$$
$$\theta_2 = \gamma + \frac{c}{2\omega_{n+1}}, \tag{4.24}$$

where $\omega_{n+1} = \Delta t_{n+1}/\Delta t_n$ is the relaxation between two consecutive time steps. With this structure, the parameter values for the SBDF method are: $\alpha_2 = 1.5$, $\alpha_1 = -2$, $\alpha_0 = 0.5$, $\beta_1 = 2$, $\beta_0 = -1$, $\theta_2 = 1$, $\theta_1 = 0$ and, finally, $\theta_0 = 0$. $c = 0$ and $\gamma = 1$ are constants for the SBDF method.

For an incompressible, turbulent and non-reactive case, the equation 4.23 can be reformulated as follows:

$$\frac{\alpha_2(\rho u_i)|^{n+1} + \alpha_1(\rho u_i)|^n + \alpha_0(\rho u_i)|^{n-1}}{\Delta t^{n+1}} = -\frac{\partial p}{\partial x_i}\bigg|^{n+1} + \theta_2 f(\rho u_i)|^{n+1} + \theta_1 f(\rho u_i)|^n + \theta_0 f(\rho u_i)|^{n-1} + \beta_1 g(\rho u_i)|^n + \beta_0 g(\rho u_i)|^{n-1}, \quad (4.25)$$

where the terms $f(\rho u_i)$ and $g(\rho u_i)$ are defined as:

$$f(\rho u_i) = \frac{\partial}{\partial x_j}\left[(\mu + \mu_t)\left(\frac{\partial u_j}{\partial x_i} + \frac{\partial u_i}{\partial x_j}\right) - \frac{2}{3}\rho k \delta_{ij}\right], \quad (4.26)$$

$$g(\rho u_i) = -\frac{\partial}{\partial x_j}(\rho u_j u_i). \quad (4.27)$$

The same strategy may be applied for the transport equation of mass fractions:

$$\frac{\alpha_2(\rho Y_k)|^{n+1} + \alpha_1(\rho Y_k)|^n + \alpha_0(\rho Y_k)|^{n-1}}{\Delta t^{n+1}} = \theta_2 f(\rho Y_k)|^{n+1} + \theta_1 f(\rho Y_k)|^n + \theta_0 f(\rho Y_k)|^{n-1} + \beta_1 g(\rho Y_k)|^n + \beta_0 g(\rho Y_k)|^{n-1}, \quad (4.28)$$

where $f(\rho Y_k)$ and $g(\rho Y_k)$ are defined, respectively, as:

$$f(\rho Y_k) = \frac{\partial}{\partial x_i}\left[\left(\rho D_k + \frac{\mu_t}{Sc_{kt}}\right)\frac{\partial Y_k}{\partial x_i}\right], \quad (4.29)$$

$$g(\rho Y_k) = -\frac{\partial}{\partial x_j}(\rho u_j Y_k). \quad (4.30)$$

With those equations, the discretization of the transport equations is ended and the pressure-velocity coupling may be presented.

4.3 Pressure-velocity coupling

The separated solution of the mass conservation and Navier-Stokes equations demands a method for pressure-velocity coupling. The fractional step method (CHORIN, 1968) is the chosen approach for the actual research and is based on the fact that the pressure does not play a role thermodynamically, but forces the incompressibility condition, leading the velocity and pressure to be determined in two steps. In the first, an auxiliary velocity field $\tilde{u}$ is calculated using the balance of *momentum* equations, without taking into account the incompressibility. For the second step, the auxiliary velocity field is projected into the space of vector fields with null divergent to calculate the pressure or its correction. Then, the velocity field is updated.

In the fractional step method, the equation (4.25) is reformulated, so the pressure is calculated for the time step $t = n$ and the velocity field is estimated:

$$\frac{\alpha_2(\rho u_i^*)|^{n+1} + \alpha_1(\rho u_i)|^n + \alpha_0(\rho u_i)|^{n-1}}{\Delta t^{n+1}} = -\frac{\partial p}{\partial x_i}\bigg|^n + \theta_2 f(\rho u_i)|^{n+1} + \theta_1 f(\rho u_i)|^n + \theta_0 f(\rho u_i)|^{n-1} + \beta_1 g(\rho u_i)|^n + \beta_0 g(\rho u_i)|^{n-1}, \quad (4.31)$$

where u_i^{*n+1} corresponds to the estimated velocity field. When subtracting the equations (4.31) and (4.25) and considering that $Q = p^{n+1} - p^n$, the resulting expression is:

$$\frac{\alpha_2(u_i^{*n+1} - u_i^{n+1})}{\Delta t} = \frac{1}{\rho}\frac{\partial Q}{\partial x_i}. \quad (4.32)$$

From the application of a divergent operation:

$$\frac{\alpha_2}{\Delta t}\left(\frac{\partial u_i^{*n+1}}{\partial x_i} - \frac{\partial u_i^{n+1}}{\partial x_i}\right) = \frac{\partial}{\partial x_i}\left(\frac{1}{\rho}\frac{\partial Q}{\partial x_i}\right). \quad (4.33)$$

Taking into account that the present work is incompressible, the mass conservation equation expresses that the divergent of u_i^{n+1} must be zero. Thus, the resulting equation is:

$$\frac{\alpha_2}{\Delta t}\left(\frac{\partial u_i^{*n+1}}{\partial x_i}\right) = \left(\frac{1}{\rho}\frac{\partial^2 Q}{\partial x_i \partial x_i}\right). \quad (4.34)$$

Finally, the velocity correction is obtained:

$$u_i^{n+1} = u_i^{*n+1} - \frac{1}{\rho}\left(\frac{\partial Q}{\partial x_i}\right)\frac{\Delta t}{\alpha_2}. \tag{4.35}$$

This section had the intention to present a way of coupling pressure and velocity through calculations of the discretized equations.

4.4 Immersed Boundary Method

The Immersed Boundary method consists of the use of two independent meshes in order to represent solid structures immersed in a fluid, as illustrated by the figure (4.4). The solid structures in blue, represented by Γ, are the lagrangian domain and indicates an immersed geometry inside the flow. The other domain, indicated by Ω, is the eulerian and indicates a region where fluid flows in a fixed and cartesian mesh in which the transport equations are resolved. The vector $\vec{x}$ represents the position of any point concerning the eulerian mesh, while the vector $\vec{X}$ indicates the position of any point of the Lagrangian mesh.

Besides, the figure (4.5) illustrates with more details the real eulerian and lagrangian mesh representations used in the actual work, in which it can be noted the cartesian mesh for the eulerian domain and a triangular mesh for the lagrangian.

The implemented approach in MFSim to account for the influence of the lagrangian structure as a physical geometry inside a flow domain is the Multi-Direct Forcing method based on the work of Wang, Fan and Luo (2008). The methodology consists of an iterative process of the Direct Forcing method, which will be presented. in the present section. Yet, for more details about this method, the work Vedovoto, Serfaty and Neto (2015) is indicated.

4.4.1 Direct Forcing Method

The Direct Forcing Method proposed by Uhlmann (2005) is based on the imposition of forces in the eulerian domain originated from the immersed boundary velocity. From the

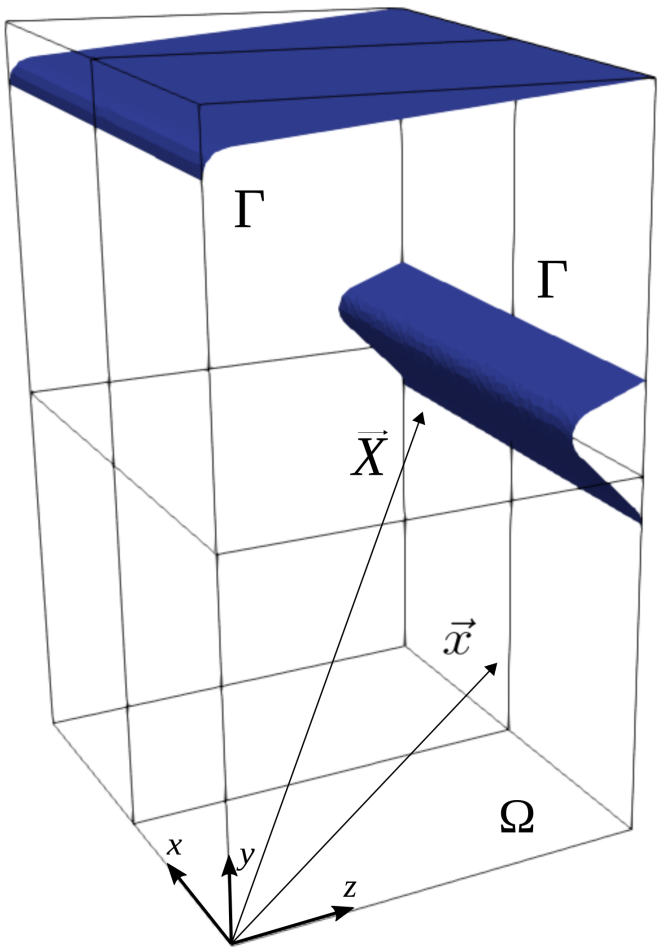

Figure 4.4 – Lagrangian and Eulerian mesh representation of the domain simulated in the present work.

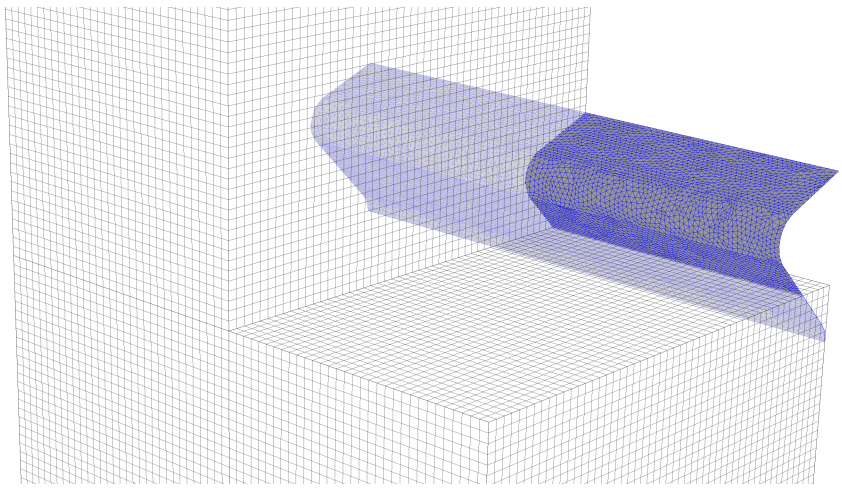

Figure 4.5 – Lagrangian and Eulerian meshes used in the actual work.

Navier-Stokes equation (3.2), when analyzing in Lagrangian points, the calculated forces in

those points can be determined:

$$F_i = \frac{\partial \rho U_i}{\partial t} + RHS_i, \tag{4.36}$$

where

$$RHS_i = \frac{\partial \rho U_i U_j}{\partial X_j} + \frac{\partial p}{\partial X_i} - \frac{\partial}{\partial X_j}\left[\mu\left(\frac{\partial U_i}{\partial X_j} + \frac{\partial U_j}{\partial X_i}\right)\right]. \tag{4.37}$$

The terms F_i, U_i, and X_i indicate the force, velocity field, and position in the lagrangian mesh elements. In contrast, the terms f_i, u_i, and x_i represent the components of force, velocity field, and position that correspond to the eulerian mesh cells.

From the temporal discretization of the equation (4.36) using a second order scheme, the result is:

$$F_i(\vec{X}, t) = \frac{\alpha_2(\rho U_i)^{n+1} - \alpha_1(\rho U_i)^n + \alpha_0(\rho U_i)^{n-1}}{\Delta t} + RHS_i^n, \tag{4.38}$$

in which α_2, α_1 and α_0 are the temporal discretization coefficients Vedovoto, Serfaty and Neto (2015). The current time step, the previous and the new are respectively indicated by the superscripts n, $n-1$ and $n+1$.

The estimated velocity field in the flow, U_i^*, is summed and subtracted in the temporal term:

$$F_i(\vec{X}, t) = \frac{\alpha_2(\rho U_i)^{n+1} - \alpha_1(\rho U_i)^n + \alpha_0(\rho U_i)^{n-1} + \alpha_2\rho U_i^* - \alpha_2\rho U_i^*}{\Delta t} + RHS_i^n. \tag{4.39}$$

From the superposition principle, the equation (4.39) is separated as follows:

$$\frac{\alpha_2\rho U_i^* - \alpha_1(\rho U_i)^n + \alpha_0(\rho U_i)^{n-1}}{\Delta t} + RHS_i^n = 0, \tag{4.40}$$

and

$$F_i(\vec{X}, t) = \frac{\alpha_2(\rho U_i)^{n+1} - \alpha_2\rho U_i^*}{\Delta t}. \tag{4.41}$$

In order to calculate the U_i^* components analyzed in the lagrangian points, an interpolation of the u_i^* components calculated in the eulerian cells close to each lagrangian points must be made:

$$U_i^*(\vec{X}) = \sum_{\Omega} D_h(\vec{x} - \vec{X}) u_i^*(\vec{x}) \Delta x \Delta y \Delta z, \tag{4.42}$$

in which D_h is an interpolation function. A hat interpolation function was used in the present work and more details are presented in Vedovoto, Serfaty and Neto (2015). Also, the u_i^* components are obtained through the solution of linear systems using the Multilevel Multigrid method (VILLAR, 2007).

Once the term U_i^{n+1} corresponds to the immersed boundary velocity, the values of the force in each lagrangian point can be obtained through the solution of the equation (4.41). If the geometry is stationary, this term is zero. Then, after the calculation of $F_i(\vec{X}, t)$ for each lagrangian point, these forces must be distributed to the eulerian cells closer to the immersed boundary:

$$f_i(\vec{x}) = \sum_{\Gamma} D_h(\vec{x} - \vec{X}) F_i(\vec{X}) \Delta \forbidden{V}_{\Gamma}, \tag{4.43}$$

where $\Delta \forbidden{V}_{\Gamma}$ is the lagrangian volume.

From the equation (4.41), taking eulerian cells into consideration, the new velocities for the eulerian cells next to the immersed boundary may be obtained:

$$f_i = \frac{\alpha_2 (\rho u_i)^{n+1} - \alpha_2 \rho u_i^*}{\Delta t} \Rightarrow u_i^{n+1} = u_i^* + \frac{f_i \Delta t}{\alpha_2 \rho}. \tag{4.44}$$

For the Multi Direct Forcing method, all the procedure described is realized iteratively, using convergence criteria. In MFSim code, this criterion is based on the convergence of the new velocity with a minimum of residue required. For every time step, the convergence is analyzed and with an iteration procedure, the calculus precision may be enhanced.

Chapter 5

VALIDATION

Since the objective of this project is to simulate a non-reactive turbulent flow inside an industrial cyclonic boiler using LES and URANS approaches and with one or several chemical species, validations that concern the Immersed Boundary Method and Multi-component Mixing are presented.

5.1 Multi-component turbulent flow

A simulation of a non-premixed multi-component non-reactive turbulent flow was realized to validate the methodology about turbulent mixing implemented in MFSim, an in-house code developed at the Fluid Mechanics Laboratory (MFLab), located at the Federal University of Uberlândia. This validation concerning a multi-component flow is crucial for the reliability of the simulation of a CO boiler with a strong mixing of substances due to a turbulent swirl.

The choice of studying non-premixed jets lies in the fact that, regarding an industrial context with reactive cases, they are simple to design, build, and safer to operate.

The simulation of combustion in transient, turbulent, and gaseous jets is a significant topic of research, knowing the industrial interest in the development of technologies involving the use of alternative and fossil fuels (WU; BUSHE; DAVY, 2010). The study of non-reactive turbulent flows in inert environments is a first step in the understanding of fuel-air mixing processes so one can have more reliable results when simulating reactive flows. Besides that, the

inert study of non-premixed flows helps to focus only on the problem of turbulence, which is one of the most influential phenomena in combustion (PAYRI et al., 2016). According to Peters (2001), turbulence increases the mixing process and enhances combustion.

The simulation was based on the experimental analysis made by Schefer (2001), who tested a non-premixed and non-reactive turbulent round jet composed of propane into a coflowing air jet. The experimental apparatus used was a forced-draft vertical wind tunnel with an axisymmetric fuel jet situated at the upstream of the test section, which has a 20-cm-square cross-section and is 200-cm long. The fuel nozzle has an inside diameter of 0.526 cm and an outer diameter of 0.90 cm. The fuel jet (bulk) velocity was 53 m/s ($\pm$ 0.1 m/s) and the coflowing air velocity was 9.2 m/s ($\pm$ 0.1 m/s).The velocity measurements showed that the maximum velocity at the centerline of the jet exit was 69 m/s and that it was consistent with a fully-developed turbulent pipe flow. Also, the temperatures of the propane jet and the coflow air were 294 K. The Reynolds number based on the jet exit diameter was 68,000.

Concerning the numerical modeling, it was used the URANS standard k-ε model which requires two more transport equations for turbulent kinetic energy and dissipation rate, besides the Navier-Stokes equations and the continuity equation.

The description of a gas mixture is represented by the equation of mass conservation of species (3.57).

For the setup of the simulation, an eulerian domain was defined with the dimensions of $40D$ x $80D$ x $40D$, where D is the diameter of the fuel jet nozzle, $D = 5.2 \times 10^{-3}\ m$. The base mesh chosen is composed of $32 \times 64 \times 32$ elements and three more physical levels with adaptive refinement, which results in, approximately, 350,000 cells at the beginning of the simulation, with the finest mesh level having an element dimension of $\delta_x = 8.124 \times 10^{-4}\ m$. This element size in the fourth physical level (finest) guarantees at least six elements along the diameter of the jet nozzle. The refinement criterion is based on density, vorticity, and turbulent viscosity gradients.

The figure (5.1) illustrates the 4 physical levels of the cartesian mesh and evidences the transition of a more refined level to a less refined by a rate of 2 (the number of cells is divided by

2 in each direction).

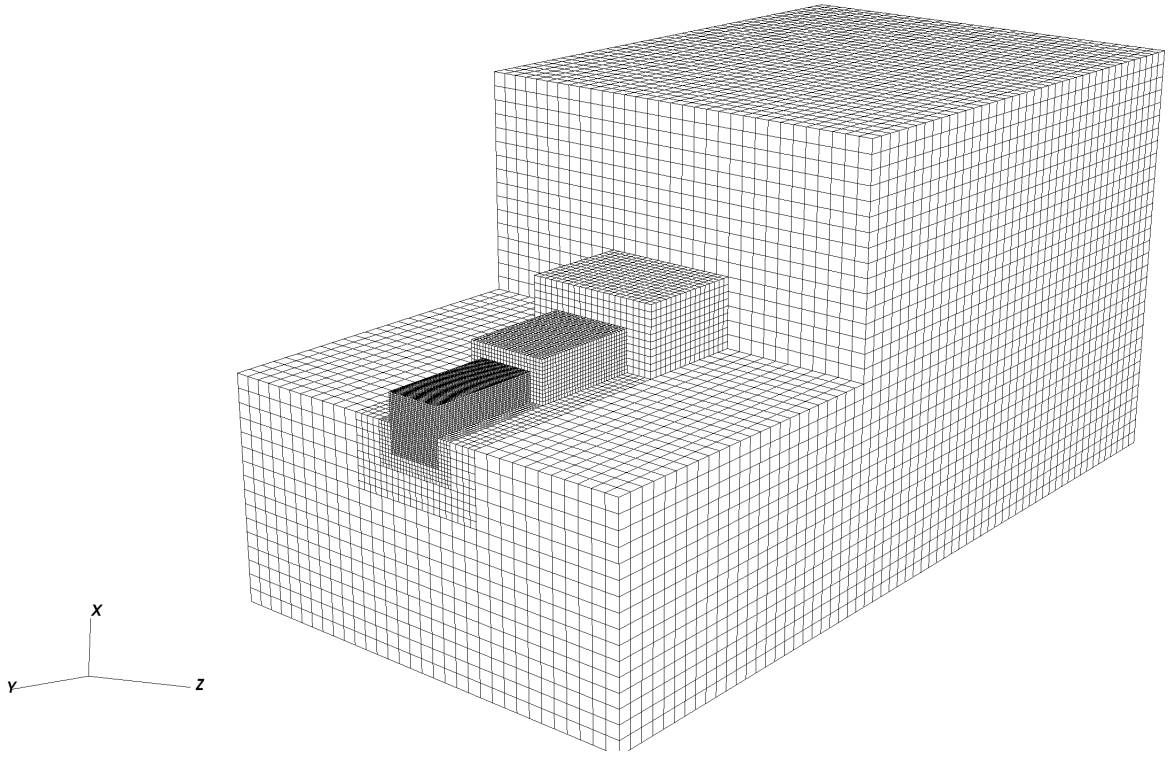

Figure 5.1 – Mesh representation of the eulerian domain containing 4 refinement levels.

Figure (5.2) shows the location of the jet circumference and the inlet velocity distribution, situated in the finest mesh level.

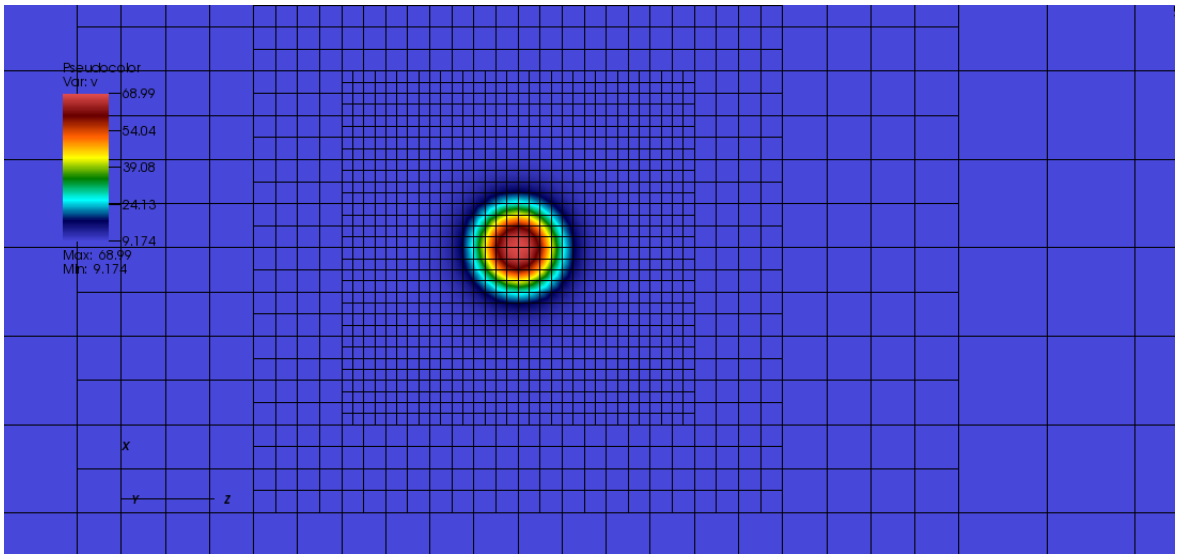

Figure 5.2 – Illustration of the block-structured refinement surrounding the jet nozzle.

The inlet conditions for the velocity are zero for velocity components in X and Z

directions. For the y-direction, the velocity profile is defined as:

$$v = \frac{1.28v_1 + v_0}{2} - \left(\frac{1.28v_1 - v_0}{2}\right) tanh\left[r_\theta\left(\frac{r_j}{r_0} - \frac{r_0}{r_j}\right)\right], \tag{5.1}$$

where $r_j = \sqrt{(x - 0.5D_1)^2 + (z - 0.5D_2)^2}$, $r_\theta = 1$ and $v_0 = 9.2\ m/s$, $v_1 = 53\ m/s$ are the coflow and main jet velocities, respectively. The r_0 is the nozzle jet radius and D_1 and D_2 are the dimensions of the computational domain in x and z directions.

The figure (5.3) illustrates the velocity profile, varying the value of r_j along the plane $x - z$.

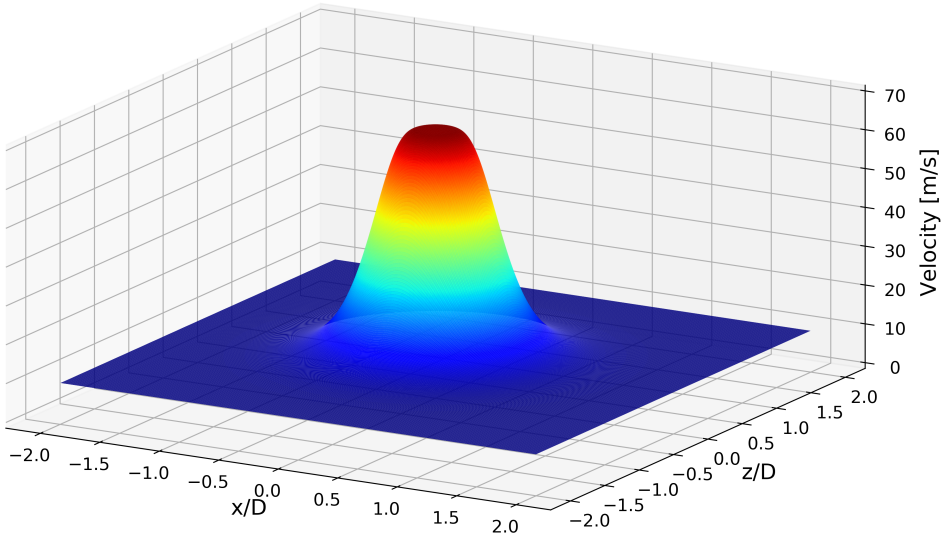

Figure 5.3 – Velocity profile used for the jet nozzle, representing a smooth transition from values distant from the center of the jet circumference.

Since there are different substances in the simulation, a hyperbolic tangential function was also used to represent density and viscosity distributions over the computational domain:

$$\rho = \frac{\rho_0 + \rho_1}{2} - \left(\frac{\rho_0 + \rho_1}{2}\right) tanh\left[r_\theta\left(\frac{r_j}{r_0} - \frac{r_0}{r_j}\right)\right], \tag{5.2}$$

$$\mu = \frac{\mu_0 + \mu_1}{2} - \left(\frac{\mu_0 + \mu_1}{2}\right) tanh\left[r_\theta\left(\frac{r_j}{r_0} - \frac{r_0}{r_j}\right)\right], \tag{5.3}$$

where ρ_0 and ρ_1 are the main jet and coflow densities, respectively, while μ_0 and μ_1 represent the main jet and coflow viscosities, respectively.

Inlet turbulent intensity of 1% was defined at the main jet exit. The pressure-velocity coupling strategy was Fractional Step and the time discretization model was the semi-implicit *SBDF*. The advection and diffusive models were *CUBISTA* and *CDS*, respectively. The CFL was set to 0.5.

For the outlet of the domain, the advection condition was chosen, while the Neumann condition was used for the rest of the walls.

The table (5.1) lists the substances and their respective mass fractions for each jet.

Table 5.1 – Mass fractions for each component of the fuel jet and coflow air.

	Substances	**Mass Fraction**
Fuel Jet	C_3H_8	1.000
Coflow	N_2	0.767
	O_2	0.233

Concerning the results of the $k - \varepsilon$ simulation, the vertical jet velocity (y direction) normal to the x direction is observed (5.4a). Also, the adaptive refinement is shown (5.4b).

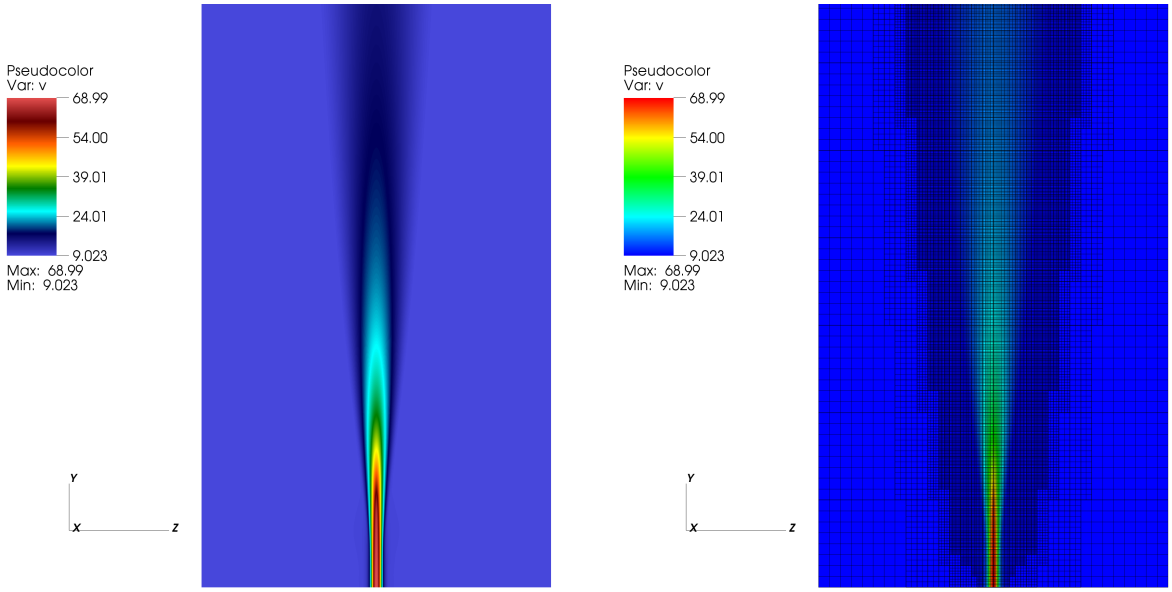

(a) Vertical jet velocity field.

(b) Adaptive refinement of the mesh in 4 levels.

Figure 5.4 – Results of the vertical velocity field and mesh distribution of the multi-component jet simulation.

According to these figures, it is visible that the mean velocity reduces in the centerline as it flows towards the exit, knowing that there is a mixture of the two gases. One could say that there is entrainment of the coflow caused by the jet flow directed to the center line and, as both

jets have different linear *momentum*, the exchange of this information might cause a velocity reduction along the Y axis.

Choosing two probes at the center of the plane $x - z$ at the positions $y/D = 15$ and $y/D = 50$, it is visible from the figure (5.5) that, for the velocity u [m/s] in the x direction, the regime achieves a permanent state after, approximately, 0.03s of simulation. The values of the velocity *v* (y direction) don't present important variations after 0.01s of simulation. Therefore, the mean values of the information analyzed for this simulation are taken after 0.03s.

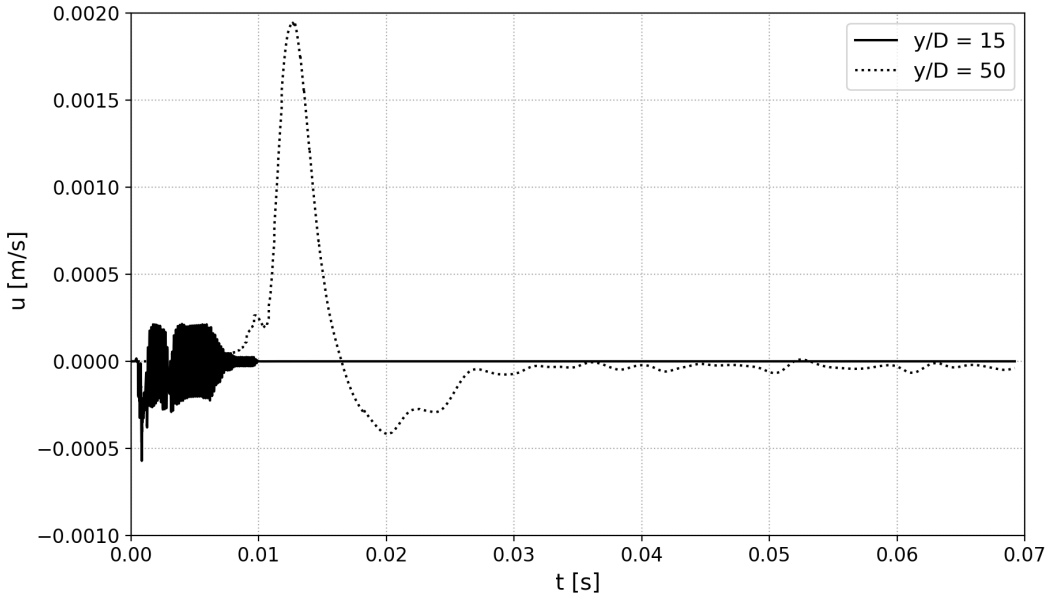

Figure 5.5 – Variation of the velocity *u* versus time for two probes in y/D = 15 and y/D =50.

A comparison of the mean velocity in the y direction (velocity v) with the data collected by Schefer (2001) is illustrated in the figure (5.6). The mean velocity values vary along the centerline of the jet towards the exit of the domain and the velocity decay data from the simulation has a good agreement with the experimental one.

It can be seen that, for the simulation data, the mean jet velocity decay happens at around $y/D = 10$, while it happens at $y/D = 5$ for the experimental data. The difference between the results might be attributed to a lack of refinement or even to an overprediction of the jet spreading rate caused by the standard $k - \varepsilon$ model. The standard $k - \varepsilon$ model with the standard constants predicts the velocity-field of a two-dimensional plane jet quite accurately, but results in

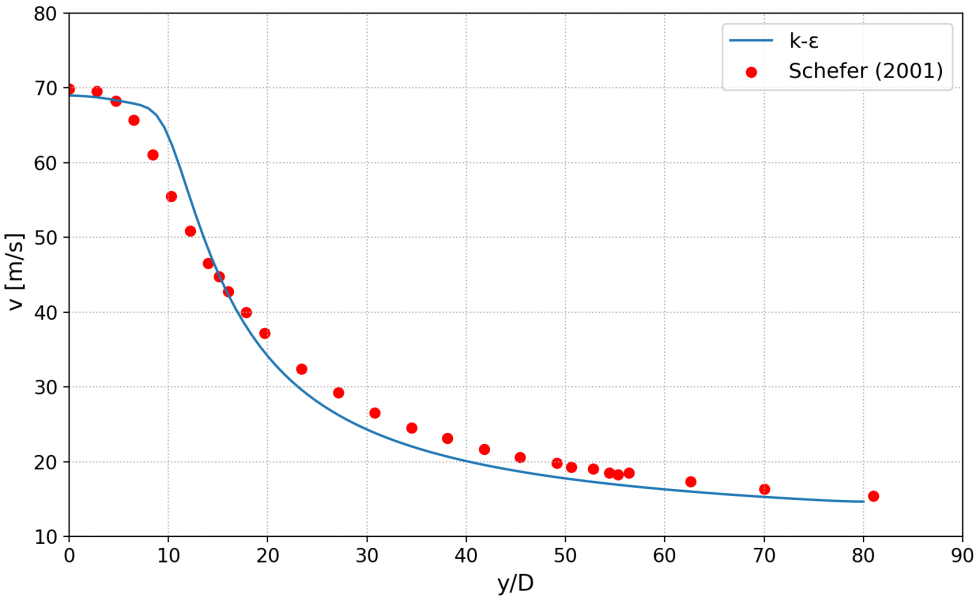

Figure 5.6 – Comparison of the mean velocity decay along the center line in the y direction with the simulation and experimental data.

large errors for axisymmetric round jets. Even though the standard $k - \varepsilon$ model is superior to the other two equations models for matching the spreading rate of round jets, it still overestimates it by 40% (SMITH et al., 2004; POPE, 1978).

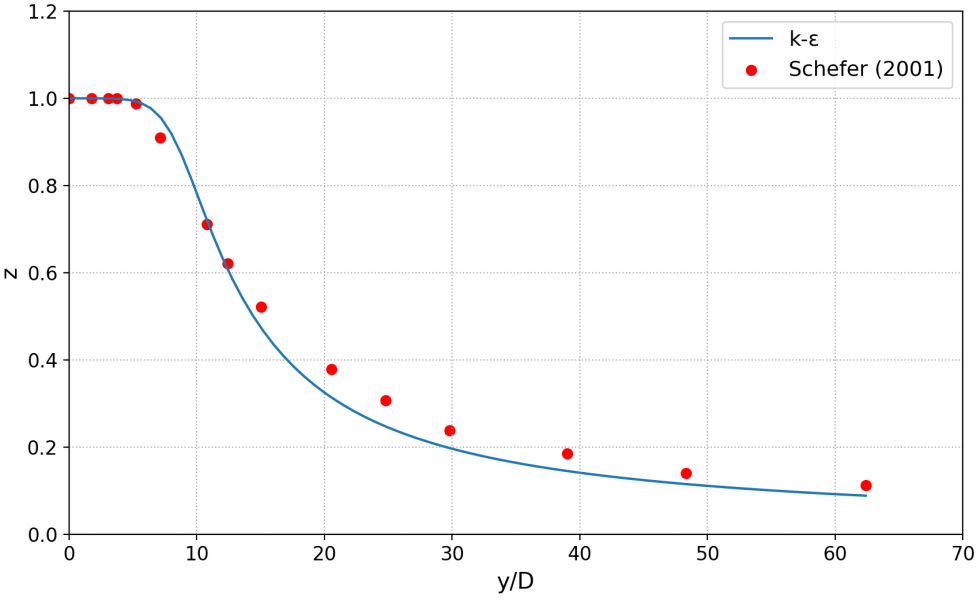

Figure 5.7 – Comparison of the mean mixture fraction along the jet centerline in the y direction between the simulation and experimental data.

Concerning the mixture fraction decay on the jet cenetline, the figure (5.7) illustrates the behavior of the numerical simulation compared to the experimental data. The mixture fraction was obtained by the expression:

$$z = \frac{sY_F - Y_O + Y_O^0}{sY_F^0 + Y_O^0} \tag{5.4}$$

where $Y_F^0 = 1.000$ and $Y_O^0 = 0.233$ represent the initial values of propane and oxygen mass fractions, respectively. The mass stoichiometric ratio, s, is equal to 3.63 for the propane combustion reaction. Near the jet nozzle exit, the experimental and numerical results agree, proving that the numerical model predicts the gas mixing well. After $y/D = 20$, the numerical results decay faster than the experimental data, but they still present satisfactory performance.

5.2 Multi-Direct Forcing validation

To test and validate the Multi-Direct Forcing method implemented in MFSim code, some simulations were done by Magalhães et al. (2019) to demonstrate the cost-benefit that IBM provides for flows around geometries. In this work, some simulations of a flow around a cylinder were accomplished, applying the Unsteady Reynolds Average Navier-Stokes (URANS) as a turbulent closure model.

It was used the standard $k - \varepsilon$ model and, for the MDF method, it is required to force a value for the turbulent kinetic energy at the body boundary. As the velocity at a wall is null, the boundary condition of the immersed boundary for the turbulent kinetic energy is also null.

To demonstrate the methodology of forcing k and ε, it was considered the turbulent kinetic energy. The first transport equation is used to estimate k, named as k^*:

$$\frac{\partial(\rho k^*)}{\partial t} + \bar{u}_j \frac{\partial \rho k^*}{\partial x_j} = \frac{\partial}{\partial x_j}\left[\left(\mu + \frac{\mu_t}{\sigma_k}\right)\frac{\partial k^*}{\partial x_j}\right] + S_k, \tag{5.5}$$

where $S_k = \mu_t S^2 - \rho\varepsilon$.

The second equation considers the turbulent kinetic energy transport equation from the URANS methodology with the addition of a force term f_k relative to MDF:

$$\frac{\partial(\rho k)}{\partial t} + \bar{u}_j \frac{\partial \rho k}{\partial x_j} = \frac{\partial}{\partial x_j}\left[\left(\mu + \frac{\mu_t}{\sigma_k}\right)\frac{\partial k}{\partial x_j}\right] + S_k + f_k, \tag{5.6}$$

Using the Euler method to discretize the temporal term at equations (5.5) and (5.6) and including a term equal to zero in eq. (5.6):

$$\frac{\rho^{(n+1)}k^{(n+1)} - \rho^{(n-1)}k^{(n-1)}}{\Delta t} + \frac{\rho^{(n+1)}}{\Delta t}(k^{*(n+1)} - k^{*(n+1)}) + \bar{u}_j \frac{\partial(\rho k)}{\partial x_j} = \frac{\partial}{\partial x_j}\left[\left(\mu + \frac{\mu_t}{\sigma_k}\right)\frac{\partial k}{\partial x_j}\right] + S_k + f_k, \tag{5.7}$$

where ρ is the density of the fluid, μ and μ_t are the molecular and turbulent dynamic viscosities, respectively, σ_k is a model constant equal to 1.0 and $S = \sqrt{S_{ij}Sij}$, in which S_{ij} represents the strain rate tensor components.

The equation (5.7) can be rearranged in two equations, one for the transport of k (eq. 5.8) and the other for the source term of the MDF (eq. 5.9).

$$\frac{\rho^{(n+1)}k^{*(n+1)} - \rho^{(n-1)}k^{(n-1)}}{\Delta t} + \bar{u}_j \frac{\partial(\rho k)}{\partial x_j} = \frac{\partial}{\partial x_j}\left[\left(\mu + \frac{\mu_t}{\sigma_k}\right)\frac{\partial k}{\partial x_j}\right] + S_k, \tag{5.8}$$

$$f_k = \frac{\rho^{(n+1)}}{\Delta t}(k^{(n+1)} - k^{*(n+1)}). \tag{5.9}$$

The steps that follow are similar to the approach applied to velocity interpolation and force calculations in Lagrangian and Eulerian points. Thus, the first step is to interpolate the values of k^* to Lagrangian points, obtaining $k^*(L)$ for each point. After, the Lagrangian force $F_{k(L)}$ is obtained by the equation:

$$F_{k(L)} = \frac{\rho^{(n+1)}}{\Delta t}(k_{(L)}^{(n+1)} - k_{(L)}^{*(n+1)}). \tag{5.10}$$

where $k_{(L)}^{(n+1)}$ is the correct value of the property at the immersed boundary in question. After calculating $F_{k(L)}$, this value is distributed to Eulerian points to obtain $f_{k(E)}$. Then, this value is used for calculating $k_{(E)}^{(n+1)}$:

$$k_{(E)}^{(n+1)} = \frac{f_{k(E)}\Delta t}{\rho^{(n+1)}} + k_{(E)}^{*(n+1)}. \tag{5.11}$$

Then, $k_{(E)}^{(n+1)}$ is used to update $k^{*(n+1)}$, which will be used in the next time step.

The boundary condition of ε was considered Dirichlet and equals to zero in the MFSim code:

$$\varepsilon = 0. \tag{5.12}$$

For the simulations, it was considered a static cylinder in a flow with Re = 200,000 in a computational domain with dimensions $60D \times 40D \times 2.5D\ m^3$, figure (5.8). They were performed with an adaptive mesh composed of five levels, with 24.576 volumes in the coarser one.

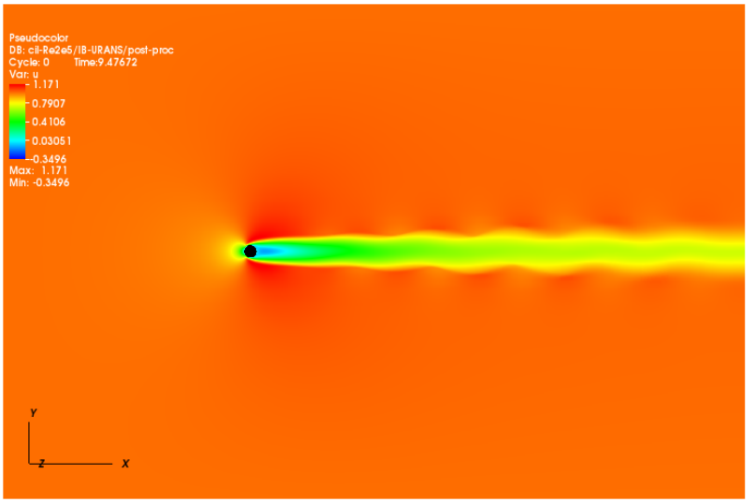

Figure 5.8 – x-Velocity field. Source: Magalhães et al. (2019)

Seeking for a validation, the drag coefficient was compared to experimental results. Schlichting and Kestin (1961) presents a drag coefficient of approximately $C_D = 1.18$ for a flow around a smooth cylinder for Re = 2×10^5. Bearman (1969) found a drag coefficient of $C_D = 1.14$ for the same Reynolds number.

Considering the work of Bearman (1969) for comparison, under these simulation settings, the resulting drag coefficient was $C_D = 1.225$, which results in an error of 7.46%.

It has been concluded that the Immersed Boundary methodology presents a good behavior with non-cartesian geometries and coarse meshes since the results are close with experimental data.

Chapter 6

RESULTS

In this chapter, it will be presented results related to a diversity of turbulence closure models applied to swirling flows and mixture fraction of species in an industrial system.

This project aims to simulate a simplified industrial CO boiler, responsible for burning gases rich in carbon monoxide produced by a Fluid Catalytic Cracking Unit in refineries. From this process, energy can be removed from these gases and a more efficient combustion process may occur, and thus, their emissions are reduced while steam is generated and energy transformed.

The simplified CO boiler structure used for simulation purposes is represented by the figure (6.1). The eulerian region is composed of structured volume cells as can be seen from the figure (6.2) and is demarcated by the lines that compose a box domain. Inside the eulerian region, it can be seen that there are three structures composed of lagrangian elements to represent three physical components able to impose restrictions to the flow, where the fluid velocity tends to zero. The first structure in the shape of a "nose" has the objective of restricting the swirling flow generated in the lowest part of the boiler. Consequently, due to this restriction, the swirling effect is affected and, thus, the fluid may be directed more easily to the outlet. Above the "nose" structure, there are five rectangular prisms that symbolize a superheater, which may induce a relevant pressure reduction and a flow organization in the outlet direction. Therefore, the fluid that had an important rotation before will tend to be symmetrically directed to the outlet, avoiding possible issues concerning the direction of vectors at the outlet region with Neumann's condition.

Still, above this structure, there is a curved plate which intention is to organize and orientate the flow to the outlet, avoiding recirculations near corners at the upper region of the boiler.

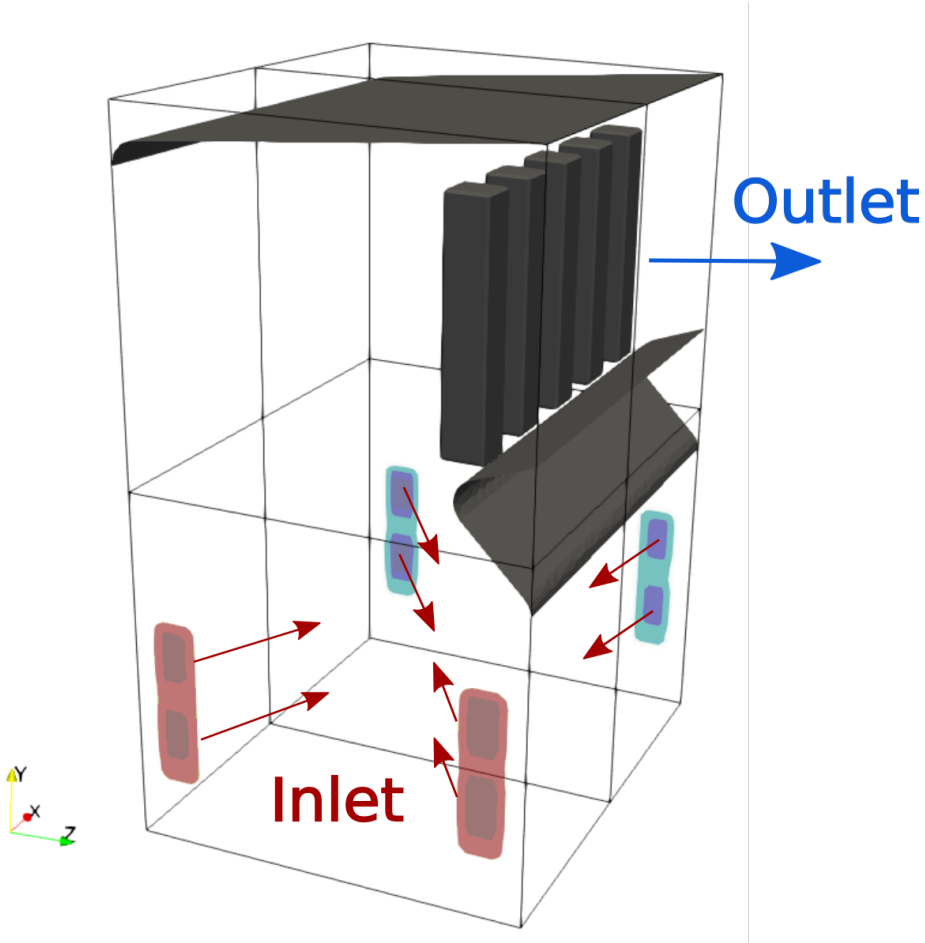

Figure 6.1 – Illustration of the industrial boiler conceived for the simulations of this project.

Still from the figure (6.1), the eulerian domain has the dimensions [8.584 x 12.64331 x 7.0857] m related to the axis x, y, and z, respectively. There are four inlets where the flow enters the domain, two are situated on the plane Y-Z where x = 0, and the other two are on the plane Y-Z at x = 8.584 m.

The eulerian mesh used is composed of, approximately, 319,488 cells, considering that the domain was divided into 64, 96, and 52 elements for the X, Y, and Z-axis, respectively. To calculate the immersed body interactions with the fluid, the lagrangian triangular mesh must be set considering that the volume of a triangular element might be similar to the volume of the eulerian cell. Therefore, the length of the lagrangian element might be obtained. In this specific case, as the eulerian element length in X direction is $\Delta x = 8.584/64 = 0.134125\ m$, from the

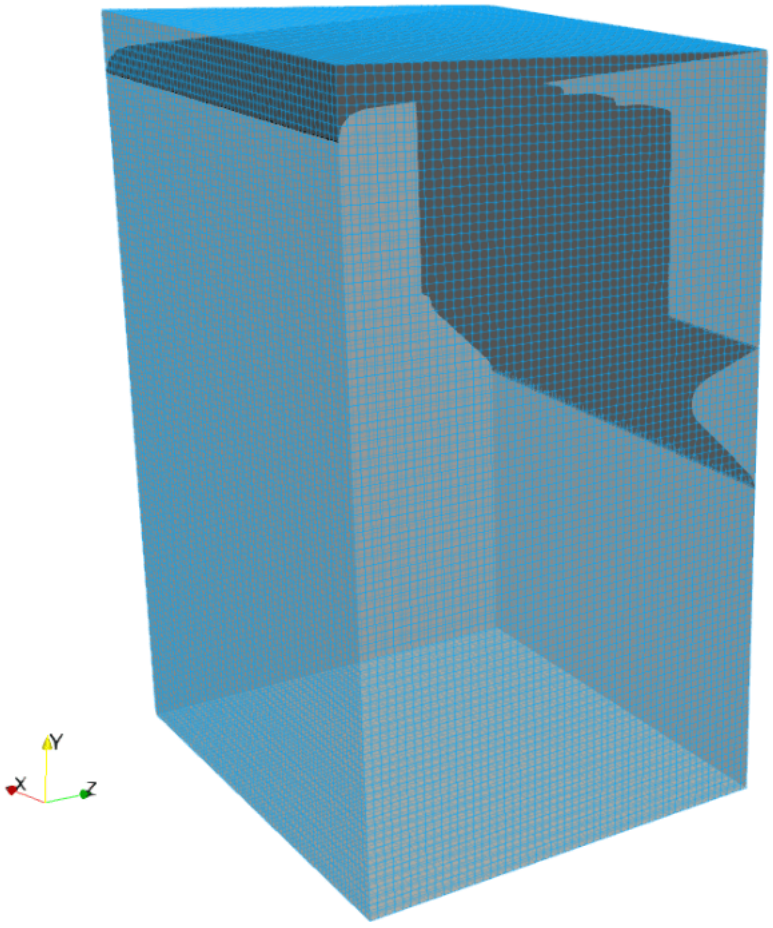

Figure 6.2 – Illustration of the eulerian mesh representing the industrial boiler.

relation $\Delta x^3 = \Delta l^3\sqrt{3}/4$, $\Delta l = 0.17728\ m$. It has been noticed, however, that immersed body effects are well predicted when the lagrangian mesh is more refined, so it was decided to divide the Δl value by two, resulting in $\Delta l = 0.0886\ m$. This value was used for all the lagrangian structures present in the simulation.

Two fluids with different velocities and physical properties flow through the rectangle inlets. In figure (6.1), the small rectangles in darker colors represent the CO gas while the zones surrounding their rectangles in lighter colors illustrate the airflow. The mass flow rates of the air and the CO gas are 31.6 kg/m^3 and 85.5 kg/m^3, respectively. For the first simulations, it will be considered only one type of fluid for both inlets, respecting the difference of velocities for each inlet, with its physical properties related to air at 650° C. Therefore, its density is $\rho =$ 0.3823 kg/m^3 and its dynamic viscosity is $\mu =$ 39.57 x 10^{-6} $kg/m.s$.

Concerning the entrance of fluids into the domain, based on a real industrial boiler, the fluid flows following an angle between the direction of the flow and the surface of the equipment (Y-Z), in the direction to the center of the domain. Each inlet at the surfaces at x=0 and x = 8.584 m has its specific angle, described in the figure (6.3). This configuration is responsible for the generation of swirls inside the CO boiler.

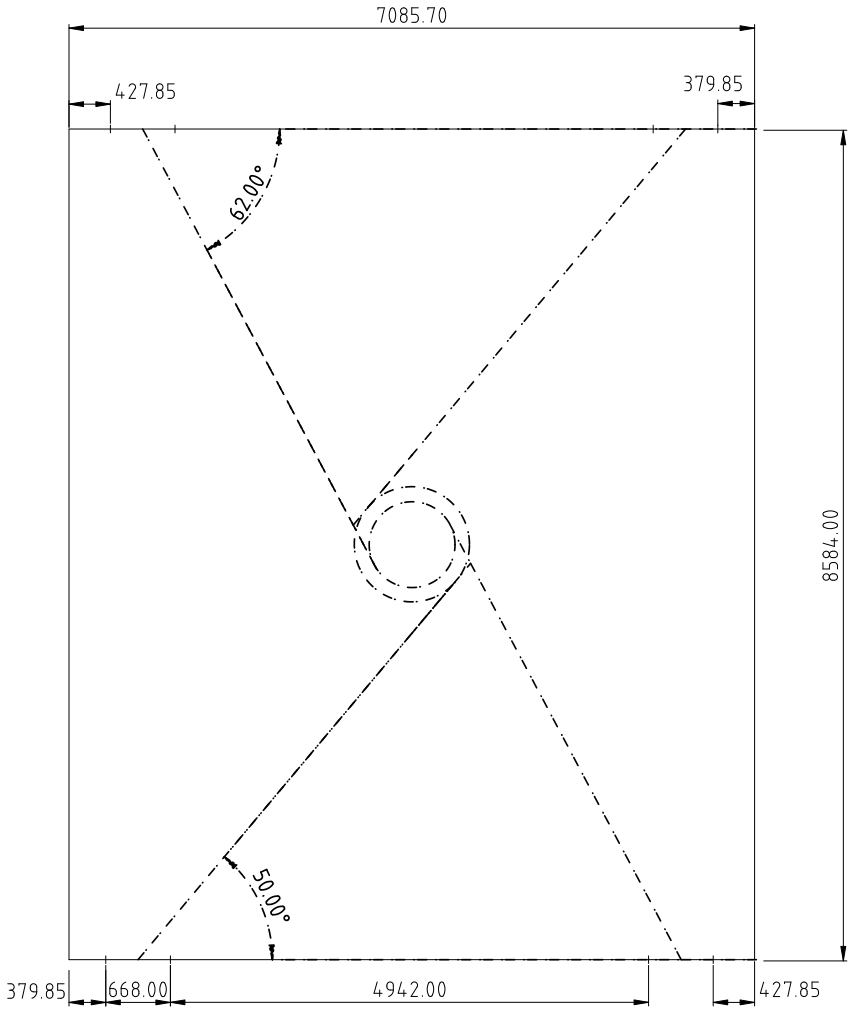

Figure 6.3 – Sketch of a technical drawing representing the boiler base on the plane X-Z evidencing the inlet angles. Dimensions in mm.

The details about the geometry of the inlets on the west (x= 0) and east (x = 8.584 m) walls are described in the figure (6.4).

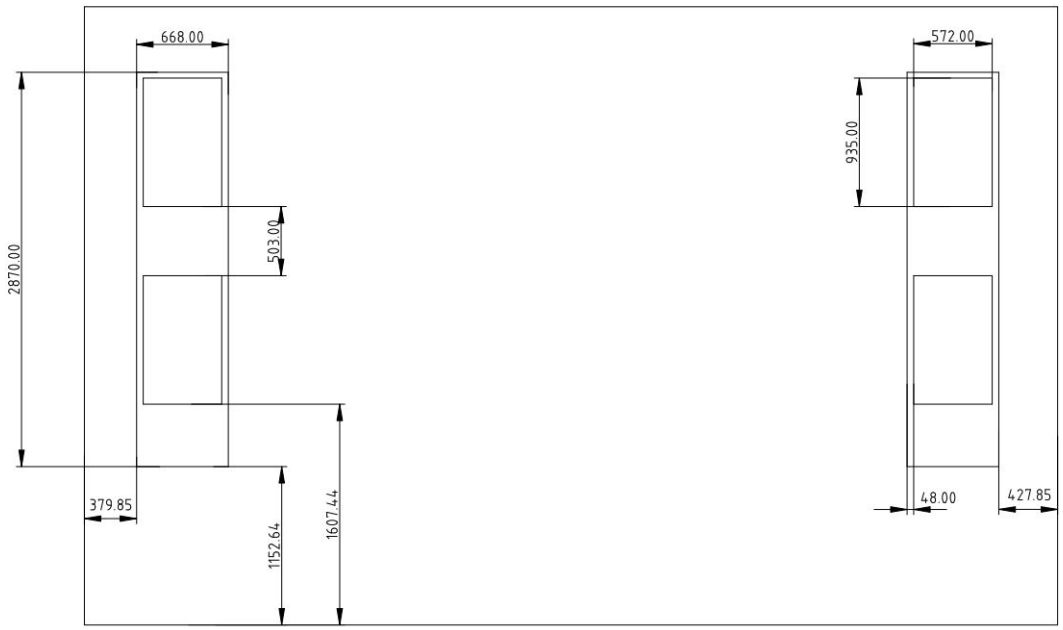

Figure 6.4 – Sketch of a technical drawing representing the inlets of the air and CO duct. Dimensions in mm.

For the first simulations, the velocities applied for the airflow and the CO gas are obtained from the relation $v = \dot{m}/\rho.A$, in which v is the velocity, $\dot{m}$ is the mass flow rate and A is the area of the rectangle inlet. The area for each airflow inlet is 0.84752 m^2, while for the CO gas is 0.53482 m^2, but, as there are two CO gas areas inside one rectangle of airflow, the total area where CO gas flows through each inlet is 1.06964 m^2. Knowing that there are four airflow inlets in total, the calculus for the velocities is then described in the table (6.1).

In this situation, the density and viscosity of the CO gas are equal to the air's because only one sort of fluid (air) is used for the first set of simulations. Their difference lies only in the velocity.

Concerning the numerical configurations for the subsequent simulations, the pressure-velocity coupling is made by the Fractional Step method and the CFL (Courant-Friedrichs-Lewy) value is set to 0.5. Also, the advection model chosen is the "CUBISTA", the diffusive model is the CDS and the temporal discretization model is semi-implicit SBDF. For the boundary and

Table 6.1 – Calculus for the velocities for each sort of fluid.

Air	CO gas
$\dot{m_{air}} = 31.6\ kg/s$	$\dot{m_{CO}} = 85.5\ kg/s$
$A_{air} = 4 \times 0.84752 = 3.39008\ m^2$	$A_{CO} = 4 \times 1.06964 = 4.2785\ m^2$
$\rho_{air} = 0.3823\ kg/m^3$	$\rho_{CO} = 0.3823\ kg/m^3$
$v_{air} = 24.38\ m/s$	$v_{CO} = 52.27\ m/s$

initial conditions, the pressure inside the eulerian domain was set as 101.000 Pa and a Dirichlet condition (velocity = 0) was set for the walls of the system (no-slip condition). The region where the flow exits the domain was set as Neumann condition for the velocities. The values of velocity for each fluid were imposed as Dirichlet (velocity = v_{ar} or v_{CO}) for the inlet regions.

To obtain velocity and pressure values at specific locations inside the eulerian domain, some probes were set in certain regions, divided into lines. From the figure (6.5), it can be seen 11 lines of probes all over the domain. The table (6.2) demonstrates some details about the number of probes and their locations in the domain.

Table 6.2 – Quantity and location for each probe line. The axis coordinates refer to a percentage of the length of the entire domain related to the respective axis.

Line nr.	Quantity of probes	X [%]	Y [%]	Z [%]
1	64	along axis	20	50
2	56	50	20	along axis
3	64	along axis	40	50
4	56	50	40	along axis
5	64	along axis	50	50
6	56	50	50	along axis
7	64	along axis	80	50
8	89	50	along axis	50
9	64	along axis	80	92
10	64	along axis	80	99
11	28	50	along axis	99

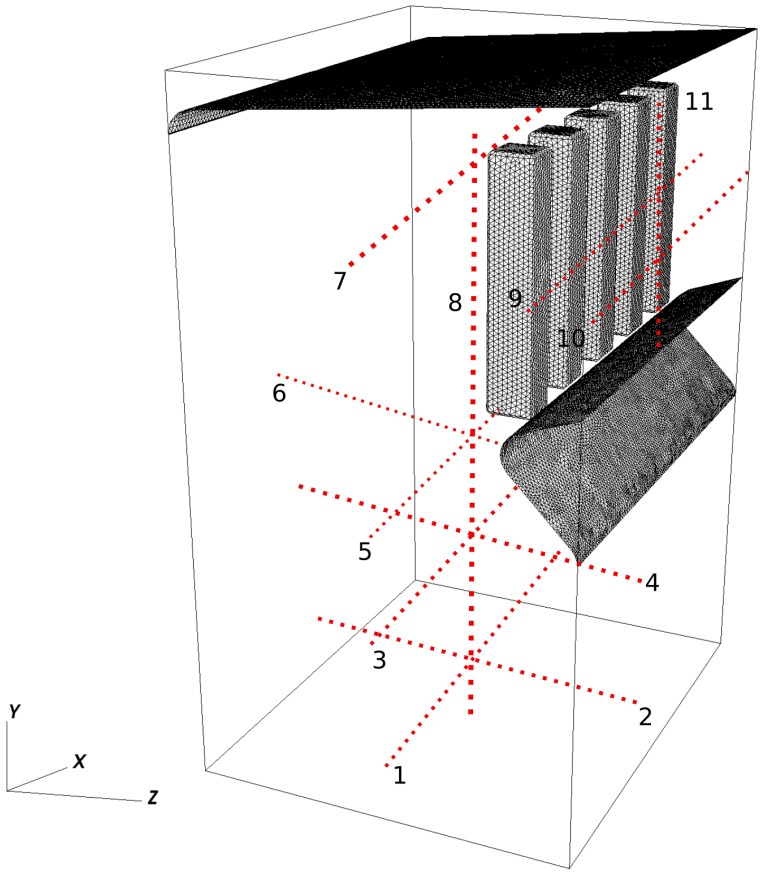

Figure 6.5 – Illustration of the probes distribution inside the eulerian domain.

6.1 Comparison between URANS standard k-ε and LES

The objective of this section is to compare the results and the computational cost between LES and URANS $k-\varepsilon$ approaches. For this reason, the same number of cells was used in the eulerian mesh domain and all parameters of the simulation were the same for both cases, except for the turbulent closure model.

Related to the LES simulation, one probe per line, at lines 2 and 9 (see table (6.2)), was analyzed, to observe results of velocities u, v, and w in relation to time. Therefore, it is possible to determine when the simulation achieves a statistically steady regime, so data could be treated in this temporal range for more accurate results. Also, for line 2, the chosen probe is situated at Z = 25%, so low-velocity values at a possible stagnation point at the center of the cyclone may be avoided. For line 9, the chosen probe is at X = 50%.

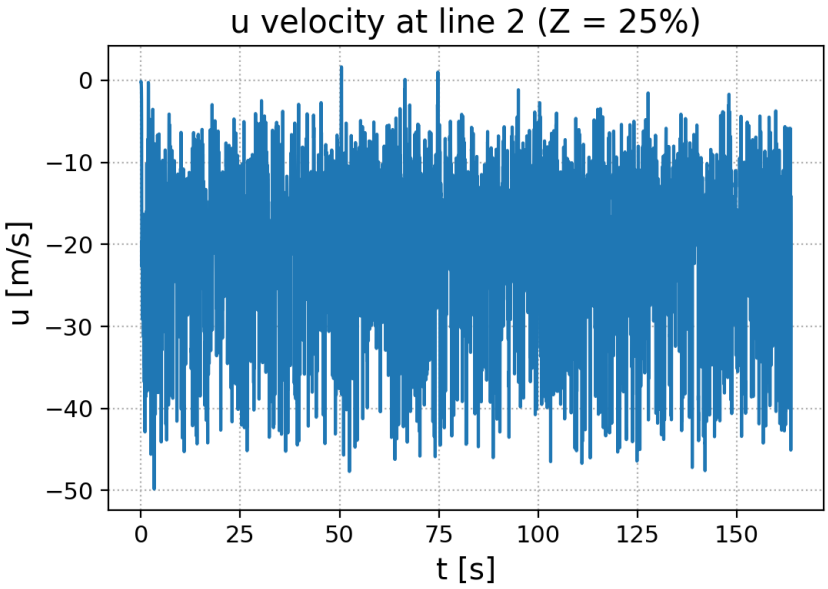

Figure 6.6 – Velocity u in relation to time at line 2.

The figure (6.6) represents how unstable the velocity results are obtained for LES simulations, since it considers velocity fluctuations in an instantaneous field due to its filtering nature. In order to analyse whether the regime is statistically steady, a cumulative mean was

realized, following the relation in a recursive way:

$$\langle\theta_i\rangle = \frac{(i-1)}{i\langle\theta_{i-1}\rangle} + \frac{\theta_i}{i}; \;\; i > 1, \tag{6.1}$$

where θ_i means the value of an array and i its index. The symbol $\langle\theta_i\rangle$ symbolizes the cumulative average from the starting i to the actual i. As the simulation considers different dt values for each time step, it might be interesting to use the relation:

$$\langle\theta_i\rangle_{\Delta t} = \frac{\langle\theta_i\rangle + \Delta t_i \theta_i}{\Delta t_i}. \tag{6.2}$$

As an example, consider Δt as a constant and an array V consisting of values from 1 to 5, $V = [1, 2, 3, 4, 5]$. Using the equation (6.1), the result is:

$$V_{c\_avg} = \left[\frac{V[i]}{i}, \frac{V[i] + V[i-1]}{i}, \frac{V[i] + V[i-1] + V[i-2]}{i}, ...\right]. \tag{6.3}$$

In which i is the index of each value in the V array ($i \geq 1$) and the result is $V_{c\_avg} = [1, 1.5, 2, 2.5, 3]$.

The figures (6.7) and (6.8) illustrate the cumulative average of the u velocity results for the probes situated at Z = 25% at lines 2 and 9. From these figures, it can be inferred that the velocity field achieves a statistically steady-state earlier at a low level of the boiler, next to the fluid inlets than after the superheater, where it approaches the outlet. Also, it can be seen that after 50s for line 2, the cumulative mean of the velocity u does not present a relevant variation (considering a tolerance of 10%), while the same occurs after 75s at line 9. Therefore, to obtain more accurate results, a temporal range from 75s to 160s has been chosen as a set for analysis.

Concerning the URANS simulation, the same probes at lines 2 and 9 were analyzed, as can be seen from the figure (6.9). It is visible that the results converge to a steady-state after a certain time and faster than LES results due to the filtering process of URANS methodology, which filters a great part of the energy spectra in order to obtain an average behavior of the velocity field, damping fluctuations in a turbulent flow. Therefore, it is considered a range of results after t = 20s for more accurate analysis.

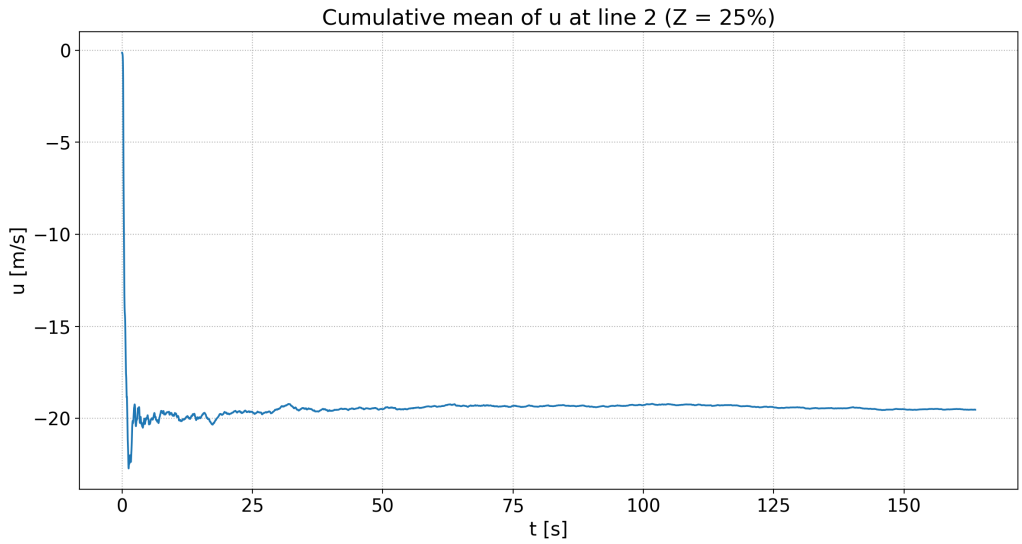

Figure 6.7 – Cumulative mean of velocity u at line 2.

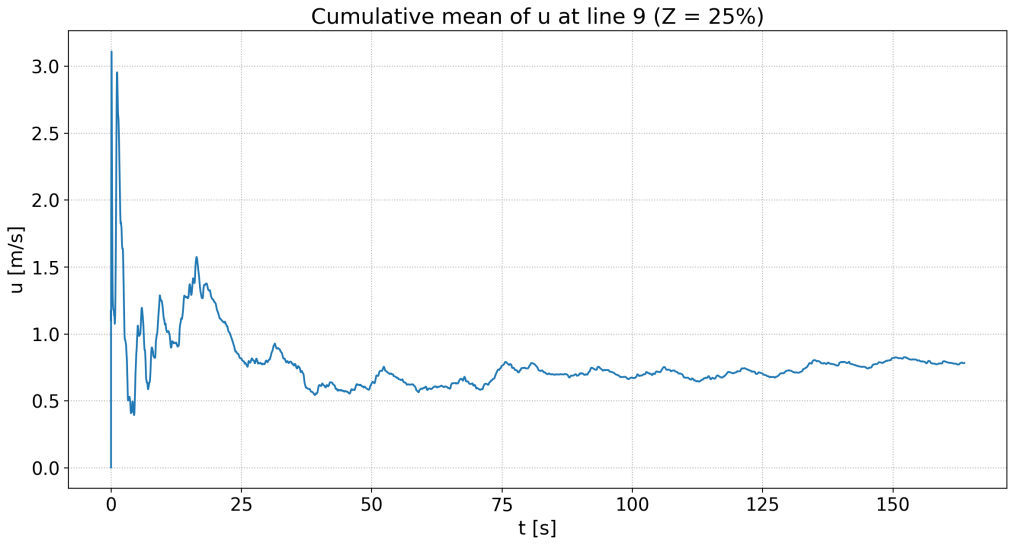

Figure 6.8 – Cumulative mean of velocity u at line 9.

When comparing LES and URANS, the LES simulation took longer to achieve results that might be considered in a statistically steady-state, while the URANS approach was much faster. Considering the LES results until 75s, the average time for each iteration is 1.49s and the total time to achieve the results is 58.78 hours. For URANS, until 20s, the average time for each iteration is 3.27s, while the total time necessary to reach steady results is 29.79h. Therefore, even though URANS presents a 119% longer iteration resolution, the simulation time needed to achieve accurate results was 49% faster, meaning a reduction of, approximately, 29 hours of

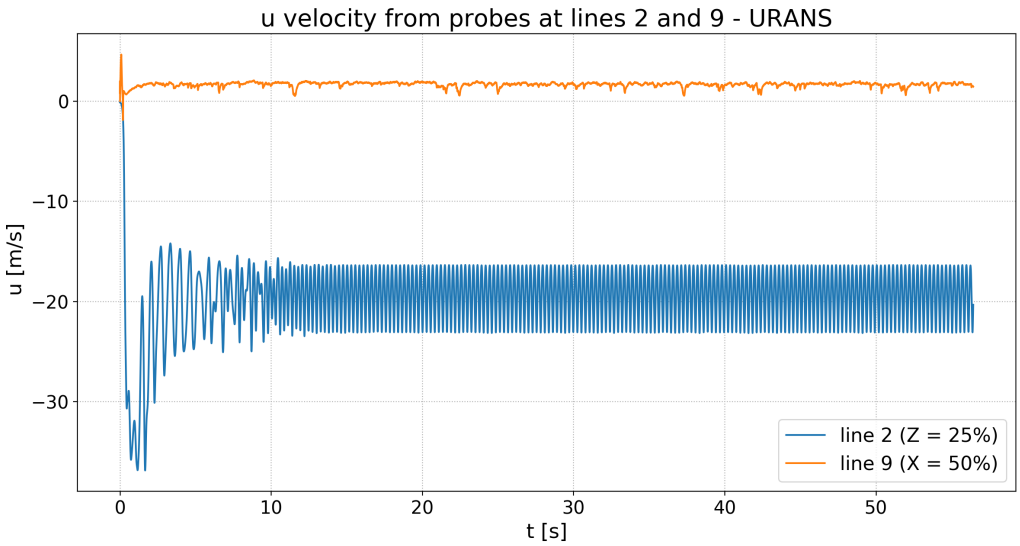

Figure 6.9 – u velocity from probes at lines 2 and 9 for the URANS simulation.

calculus.

It is important to discuss that, even though URANS standard $k - \varepsilon$ model requires two more equations to be solved, what makes its calculus take longer than LES methodology, it is a model that provides converging averaged values faster, thus, being a nice approach to be used in industrial systems where high levels of turbulence are present and the interest is concentrated on the average behavior of the fluid flow.

The figure (6.11) compares the magnitude of the averaged velocities u,v, and w for both LES and URANS simulations. The average data is similar for both methodologies and a low velocity magnitude at the center of the boiler can be pointed out as evidence of swirling effects imposed by the inlet angles. Besides that, one can notice that there might be a flow directed to the outlet in higher velocity values for LES than for URANS. The figure (6.10) illustrates the velocities v and w (Y and Z directions, respectively) along the probe line 8, at the center of the domain. Through the continuous lines, it can be seen that the velocities present a negative value, thus a contrary direction to the Y-axis, reinforcing the idea of a swirling effect and a reverse flow, with lower pressure and descending axial velocity. The dotted lines illustrate the w velocity, which has an insignificant value at the beginning of the domain since the line is centered at the boiler basis. When the flow approaches the *nose*, the swirling behavior is translated from the

center of the boiler, which makes the analyzed line placed in the region where the velocity w is negative. The *nose* structure has an objective of directing the flow to the outlet and, therefore, the velocity w achieves a positive and higher value next to the top wall of the boiler, where the main direction of the velocity w is positive, figure (6.18).

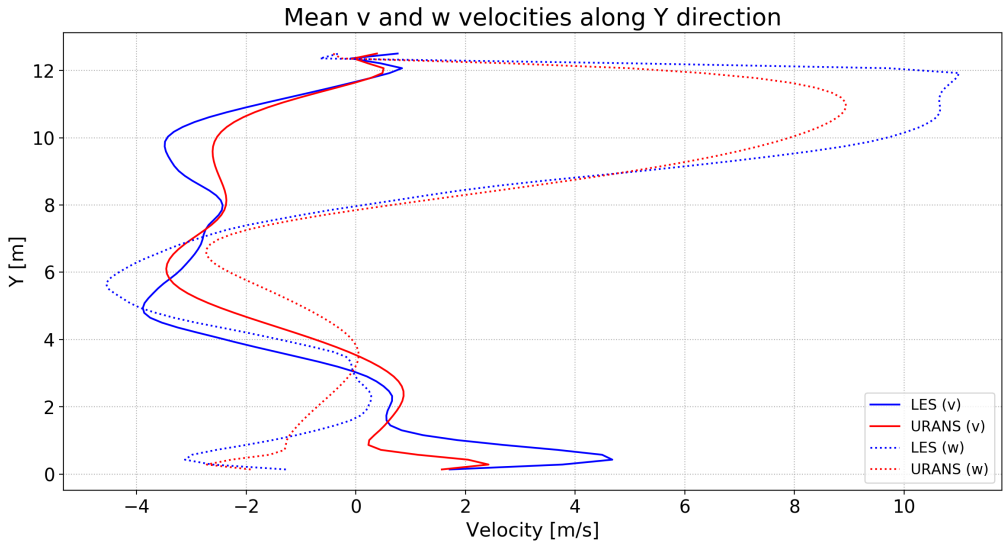

Figure 6.10 – Mean v and w velocities along the line 8, centered at the boiler domain.

It might be interesting to visualize that the velocity range is close for both simulations, with the maximum magnitude reaching, approximately, 34 m/s.

The figure (6.12) illustrates the averaged velocity v field for LES and URANS. In URANS, the region where there is a negative value or an inverted direction in relation to the Y-axis is mainly concentrated at the center with a visible gradient, representing the swirling behavior. In LES, this negative velocity at the center is present, but in less magnitude. One similarity to point out is the tendency of the ascendance of the fluid next to the wall where z = 0. Due to the presence of the *nose* structure, the fluid is forced to slow down next to this structure and to follow the angular movement. Since the *nose* forces an area reduction, the mass conservation induces the fluid to flow through this region with a high axial velocity on the opposite side of the domain, respecting the rotational tendency of the swirling flow.

The figure (6.13) demonstrates that the two turbulence approaches provide similar results when it comes to the swirl formation at Y = 20%. Even though the data is quite similar, it should

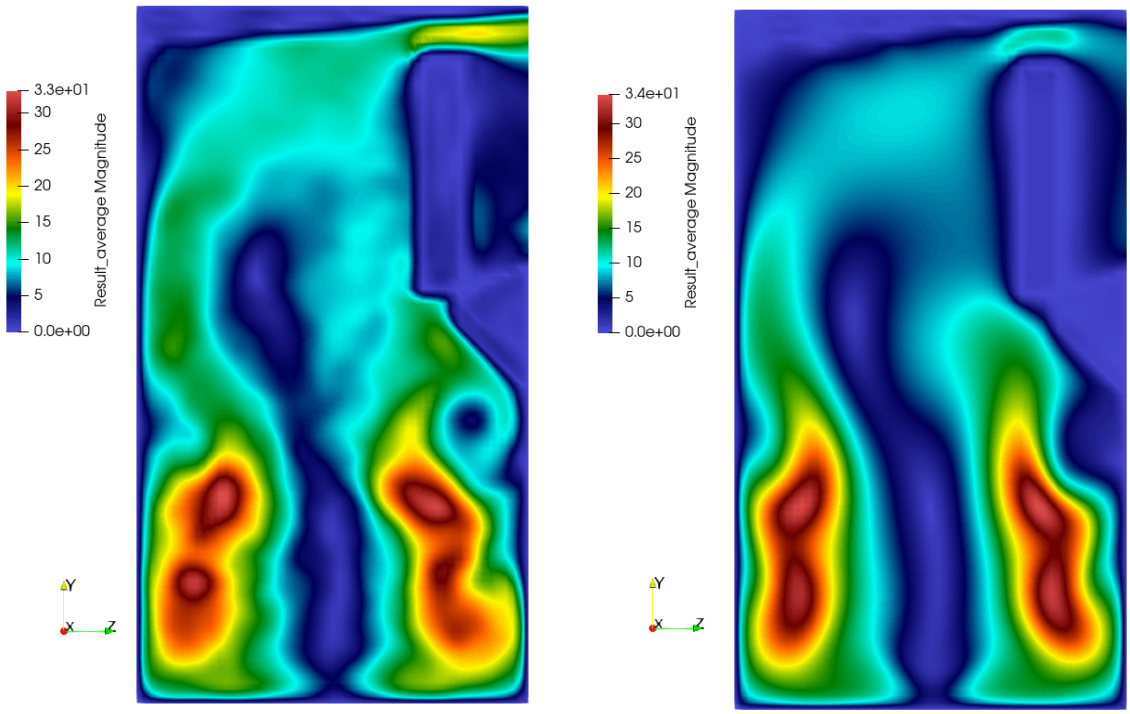

(a) LES (b) URANS

Figure 6.11 – Magnitude of velocities u,v and w [m/s] for LES and URANS simulations.

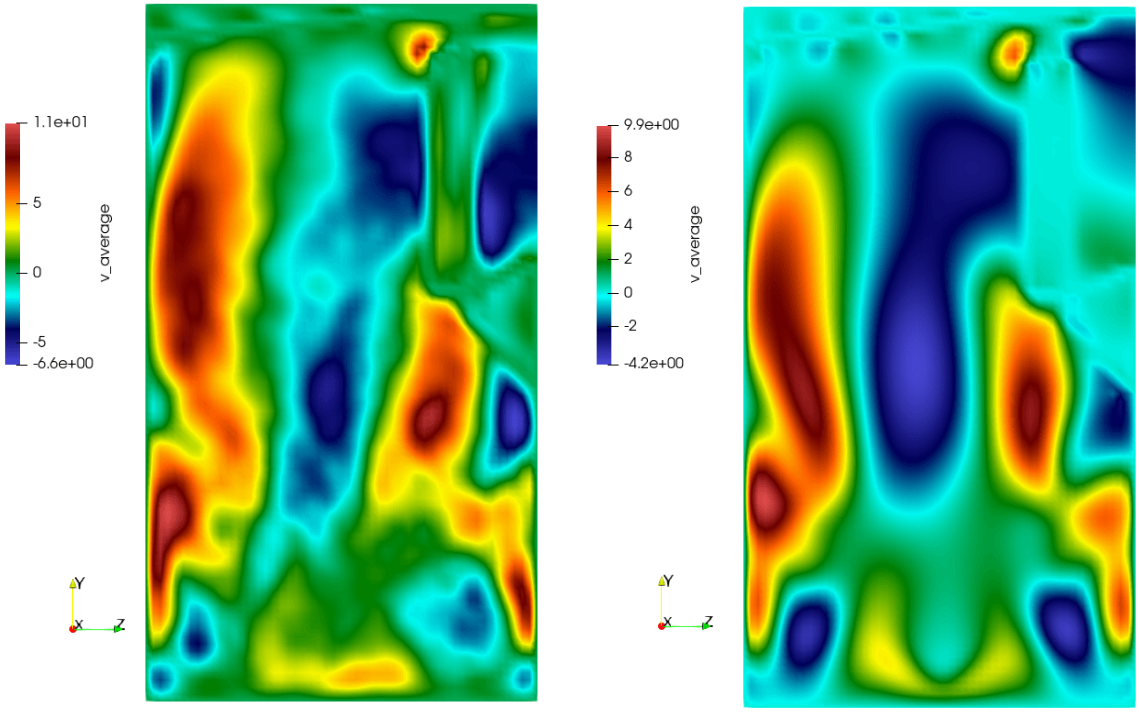

(a) LES (b) URANS

Figure 6.12 – Velocity v [m/s] for LES and URANS simulations.

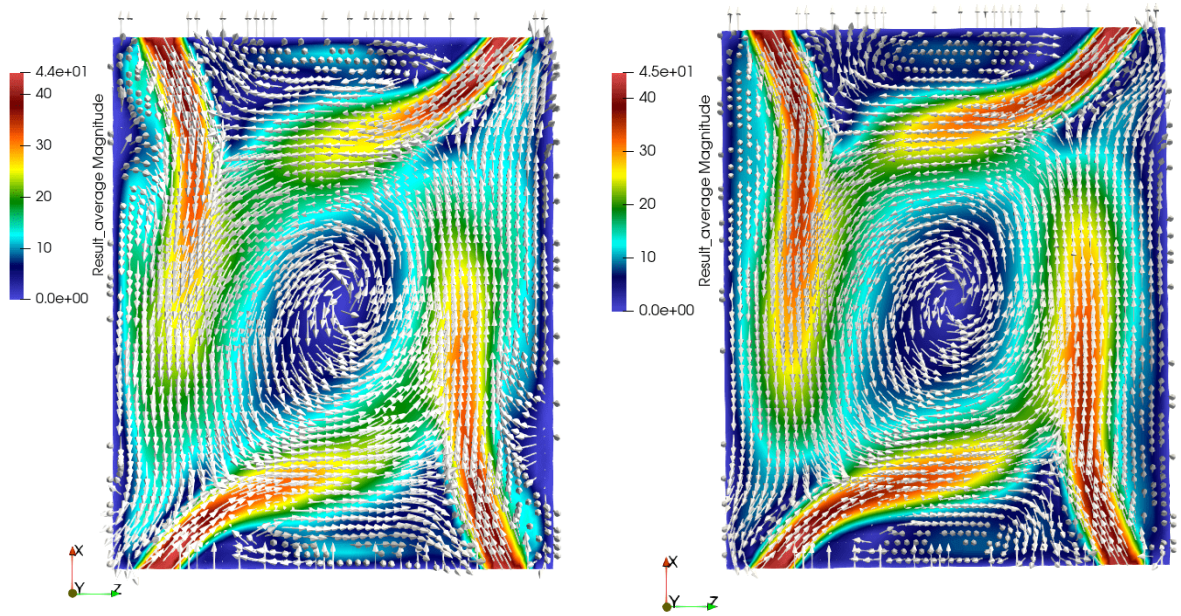

(a) LES

(b) URANS

Figure 6.13 – Magnitude of velocities u,v and w [m/s] at Y= 20% for LES and URANS simulations.

also be discussed that LES needs a well-refined mesh for accurate results, while URANS can provide reliable results with a coarser mesh grid when the interest is concentrated on the average behavior.

Next to the *nose* region, the figure (6.14) illustrates the effect of a certain compression that the structure exerts over the swirling flow, which tends to have its diameter expanded as it flows vertically. Also, it can be seen that the center of the swirling flow is translated from its origin, corresponding to what can be obtained from the data provided by the figure (6.10). Still, the rotary behavior after passing through the *nose* generates a swirl with an elliptical center. The velocity field vectors at the swirling core indicate an entrainment to the surrounding flow, causing a mass loss at the core and a pressure reduction. Due to the mass conservation law, the surrounding flow tends to fulfill the low mass region with a negative velocity direction at Y-axis.

In order to provide some data about the kinematic behavior inside the boiler, the figures (6.16) and (6.17) illustrate the axial and tangential velocities, respectively, for both URANS and LES approaches at Y = 20% and 50%. The figure (6.16) demonstrates that the data between both

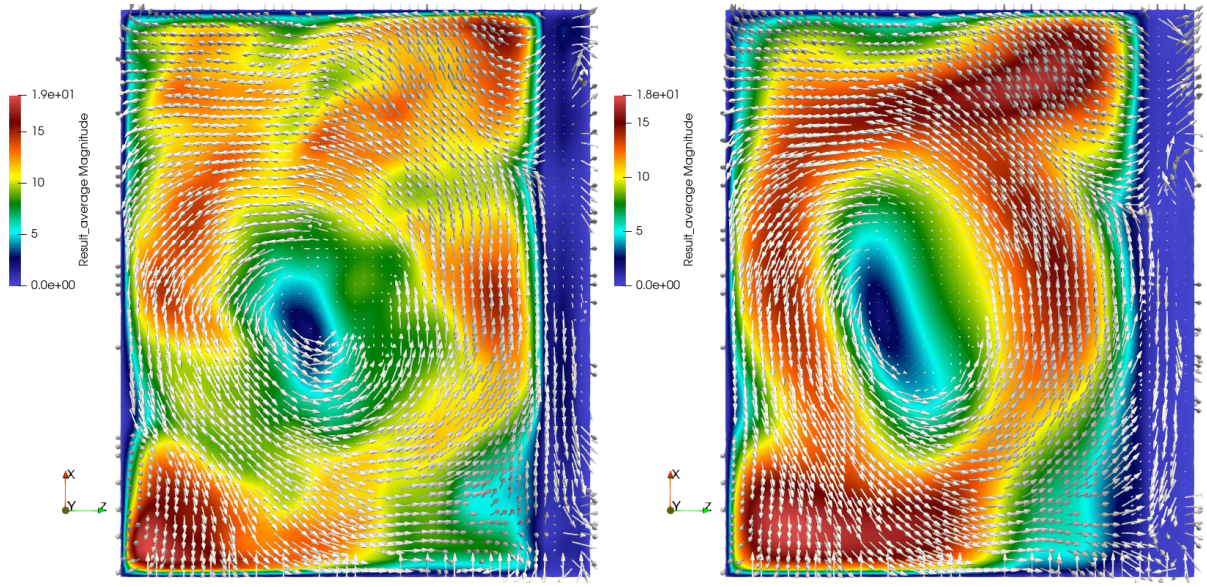

(a) LES (b) URANS

Figure 6.14 – Magnitude of velocities u,v and w [m/s] at Y= 50% for LES and URANS simulations.

approaches are close, with higher velocity values for URANS next to the walls of the domain at Y = 50%. There is also a certain asymmetry of the swirl along the X direction, more visible when the rotary behavior is more prominent next to the *nose* in contrast to the data next to the lower wall, where the cyclone is not completely formed.

From the figure (6.17), the tangential velocity is close for both cases and symmetrical, being consistent to other swirling flows studied in the literature, as those from the work of Sorrentino et al. (2015) and Grotjans (1999).

Sorrentino et al. (2015) simulated a (20 x 20 x 5 cm^3) lab-scale burner to investigate combustion and collected the tangential velocity at the centerline of the domain for different fluid inlet conditions, plotting the tangential velocity values in module, as illustrated in figure (6.15a). Differently, a cyclone separator was simulated by Grotjans (1999) using different turbulent closure models and plotting the tangential velocity at different locations at the center axis of the separator, figure (6.15b). According to the author, the $k - \varepsilon$ model provided a result of a solid-body rotation behavior. The symmetric behavior of the velocity is similar to the results of this work, with differences concerning the velocity magnitude and the locations where the maximum velocity is present, given the differences of the geometrical domains in question.

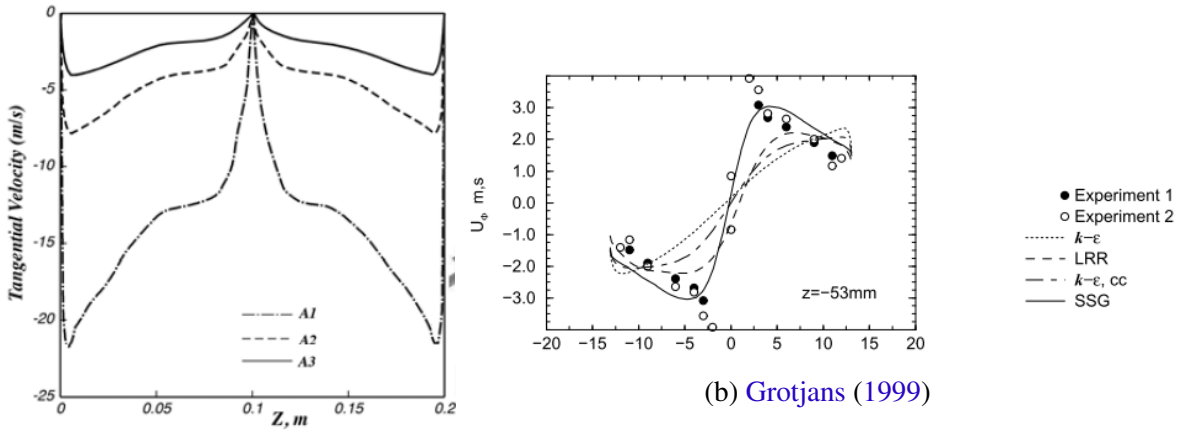

(a) Sorrentino et al. (2015)

(b) Grotjans (1999)

Figure 6.15 – Tangential velocity (m/s) in a squared lab-scale burner (a) and in a cyclone separator (b).

Opposite to was is mentioned by Grotjans (1999), the standard $k - \varepsilon$ model provided a result similar to a Rankine vortex next to the inlets, but a tendency of a solid-body rotation when Y = 50%.

It can also be concluded that when the flow approaches the *nose*, the tangential velocity decreases, especially at points far from the center of the swirl.

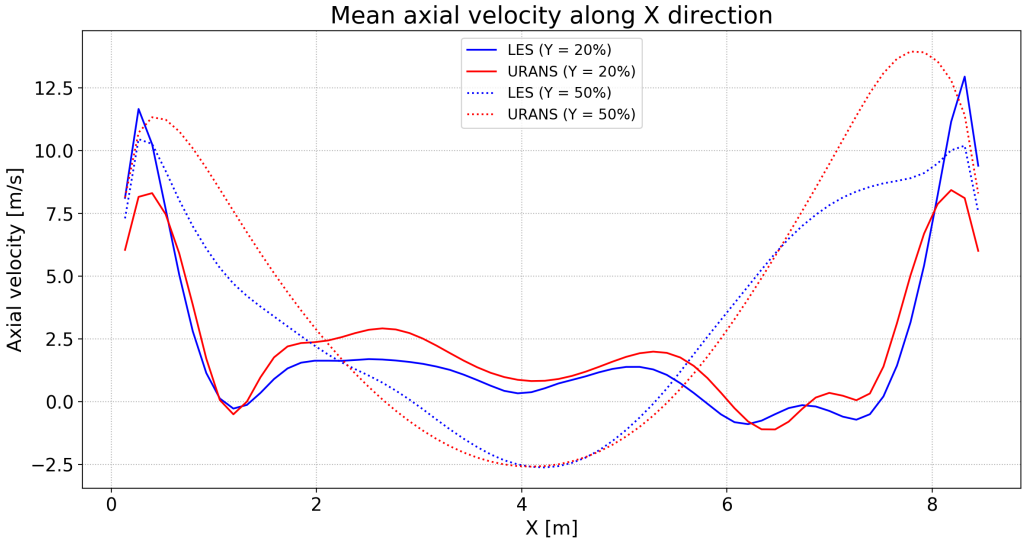

Figure 6.16 – Mean axial velocities along the lines 1 and 5 at Y = 20% and Y = 50%.

When approaching the superheater, the figure (6.18) illustrates the fluid behavior when passing through the square cylinders towards the exit. It can be noted that the velocity distribution

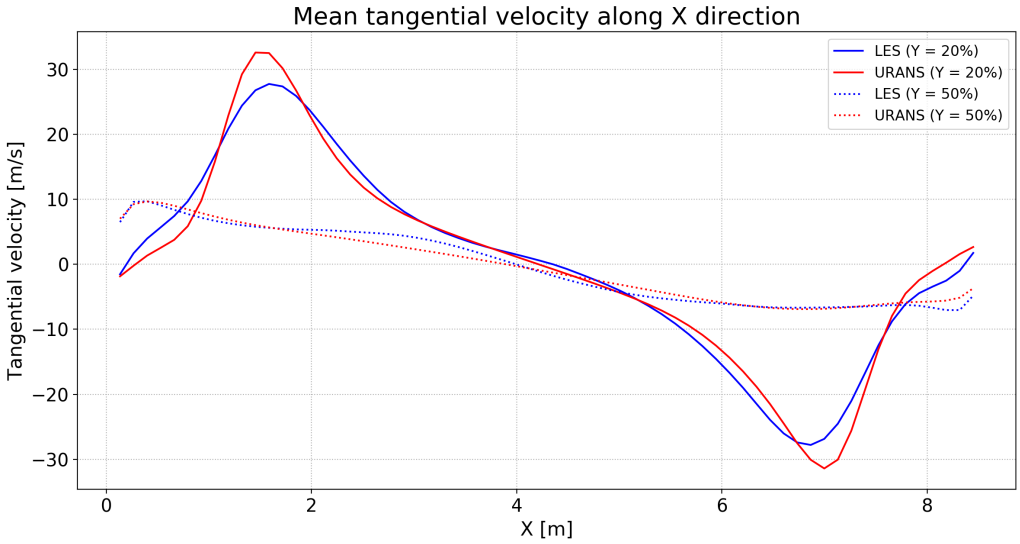

Figure 6.17 – Mean tangential velocities along the lines 1 and 5 at Y = 20% and Y = 50%.

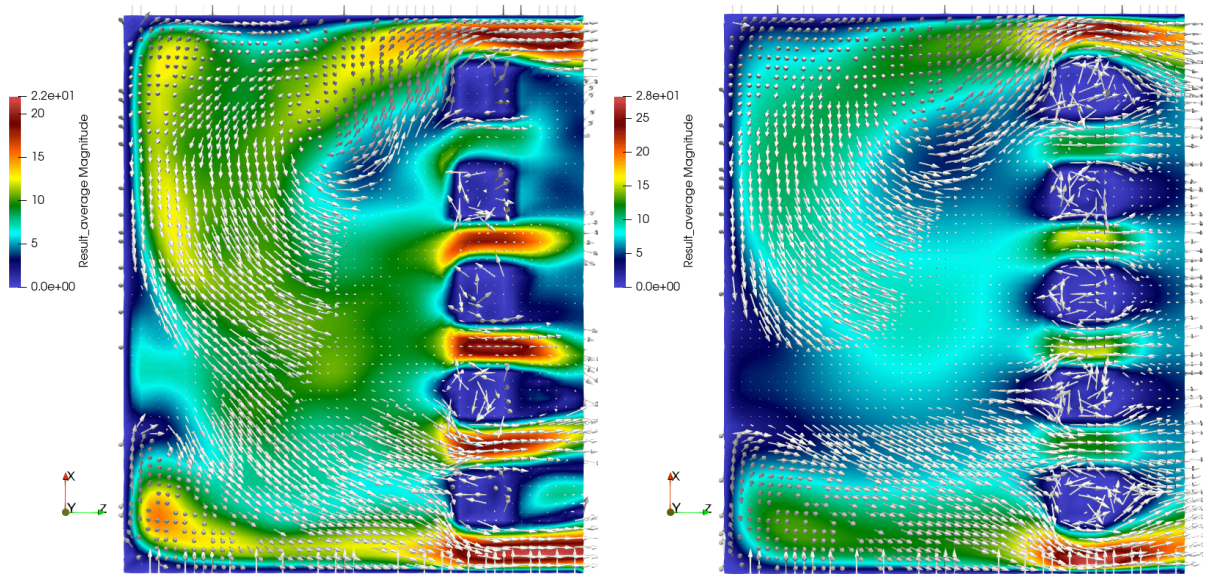

(a) LES (b) URANS

Figure 6.18 – Magnitude of velocities u,v and w [m/s] at Y= 80% for LES and URANS simulations.

between the structures is different for each simulation, with higher velocities between the rectangles and a maximum of 22 m/s for LES and lower velocities between the structures for URANS, but with higher velocities at the extremities (28 m/s). Another observation is that the vectors at the outlet are directed to the exit and normal to the surface.

The figures (6.19) and (6.20) illustrate the fluid behavior data before and after the

superheater, respectively (lines 7 and 9). At line 7, there is a slightly asymmetrical behavior of the axial velocity with higher values at the end of the domain through the X-axis, while the tangential velocity indicates that there would be a contrary rotation at the end of the domain (X-axis) for LES results, while for URANS there would be a low-velocity region, but with no contrary rotation. Except for this specific region, the data values of both approaches approximate.

At line 9, the velocities at the Z-axis direction oscillate due to the presence of the square cylinders, evidencing maximum velocities at the extremities of the domain and small peaks at the regions between the cylinders. It can also be seen that the URANS data is symmetrical, while LES presents a tendency of decreasing velocity through the X-axis direction. The velocity v (Y-axis) presents higher values at the extremities for LES simulation and negative values close to the exit, while this velocity is approximately zero for URANS, representing that the velocity vectors are straight to the exit and normal to cell surfaces.

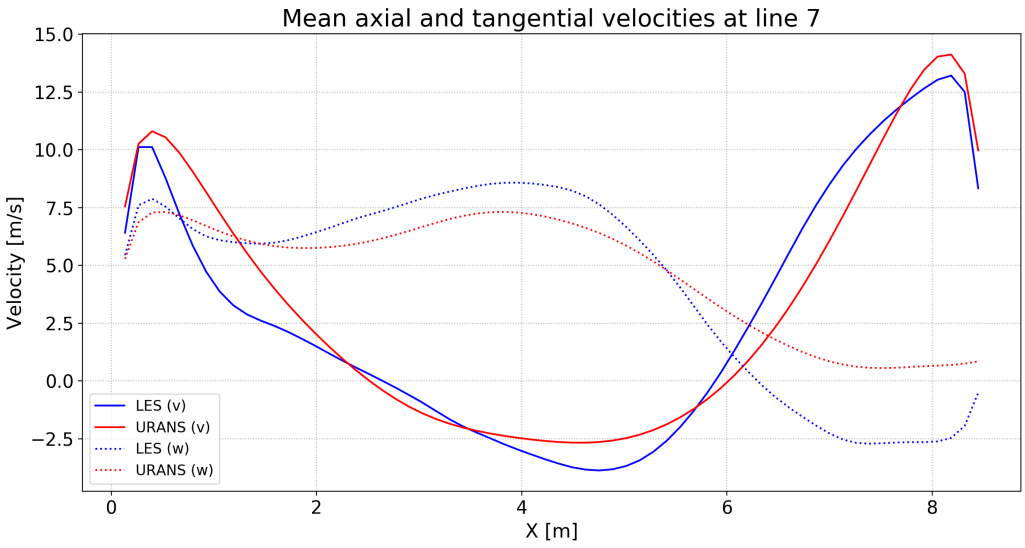

Figure 6.19 – Mean v and w velocities along the line 7 at Y = 80%.

In resume, it could be stated that velocity data concerning both turbulence model approaches are close, except for more relevant deviations close to the outlet. Even though the results were similar, it has been demonstrated that URANS data can be obtained more accurately with a coarser grid and less time when averaged results are considered. Those are important parameters to be considered in a high Reynolds number simulation in industry, depending on the

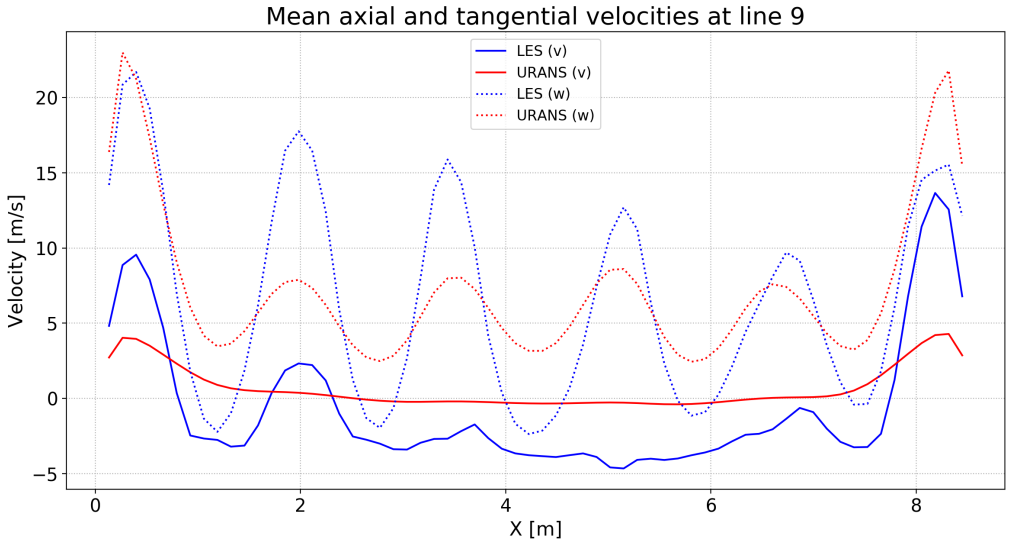

Figure 6.20 – Mean v and w velocities along the line 9 at Y = 80%.

computational capacity available. About the mesh grid, to have comparable results with more accuracy with LES methodology, a more refined mesh would be necessary, which is not viable in the actual project, giving reasons to choose URANS approaches.

Therefore, after these comparisons between LES and URANS, the latter provided good results with an interesting cost-benefit in an industrial context, being chosen to be used in the subsequent simulations.

6.2 Comparison between URANS standard k-ε, URANS k-ε modified and URANS k-ε realizable

Since the URANS Standard $k-\varepsilon$ closure model was chosen for the following investigations of the swirling flow in the studied CO boiler, it was considered important to analyze the difference that other URANS closure models would make for comparison. The models chosen for comparison are the modified $k-\varepsilon$ and realizable $k-\varepsilon$. It is highlighted that, even though these models are implemented in MFSim software, they were not tested for swirling flows, but the URANS standard $k-\varepsilon$ and the URANS realizable $k-\varepsilon$ provided accurate results for jet plane simulations (MAGALHÃES, 2018).

From the chapter 2, it has been mentioned that the standard $k-\varepsilon$ model is not recommended for elevated Reynolds numbers (MAGALHÃES, 2018) and could present a lack of accuracy for swirling flows (ARMFIELD; FLETCHER, 1989; KAYA; KARAGOZ, 2008; SAQR et al., 2009), high shear stresses, and adverse pressure gradients, since the turbulent viscosity is not well predicted for these cases (SHIH; ZHU; LUMLEY, 1995). Furthermore, as it is a semi-empirical closure model with imposed constant parameters, it might not represent with acceptable accuracy a diversity of engineering conditions.

The realizable $k-\varepsilon$ was cited as a model capable of providing better predictions of the turbulent viscosity for high shear stresses and adverse pressure gradients (SHIH; ZHU; LUMLEY, 1995). The constant parameters present in the k and ε equations of the standard $k-\varepsilon$ model are dynamically analyzed based on the velocity field, allowing its application in complex flows.

Discussing the modified $k-\varepsilon$ model, it is meant to improve calculus in stagnation regions (DURBIN, 1996). The modifications concern the calculus of μ_t and ε.

To analyze when the flow reaches a statistically steady-state for each closure model, the velocity u (X-direction) from two probes at lines 2 and 9 (see figure (6.5)) is illustrated in the figures (6.21) and (6.22).

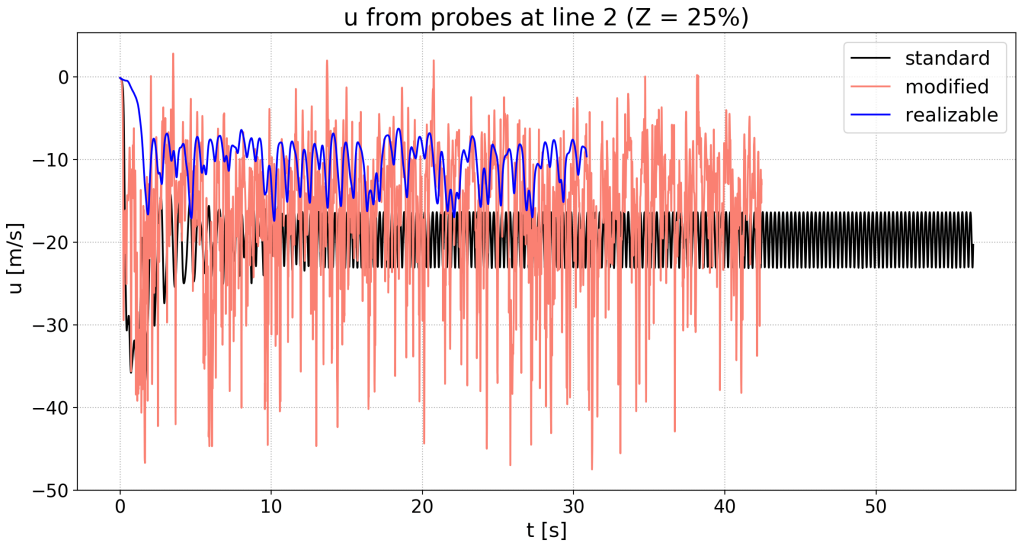

Figure 6.21 – u velocity at probe line 2 for standard, modified and realizable URANS $k-\varepsilon$.

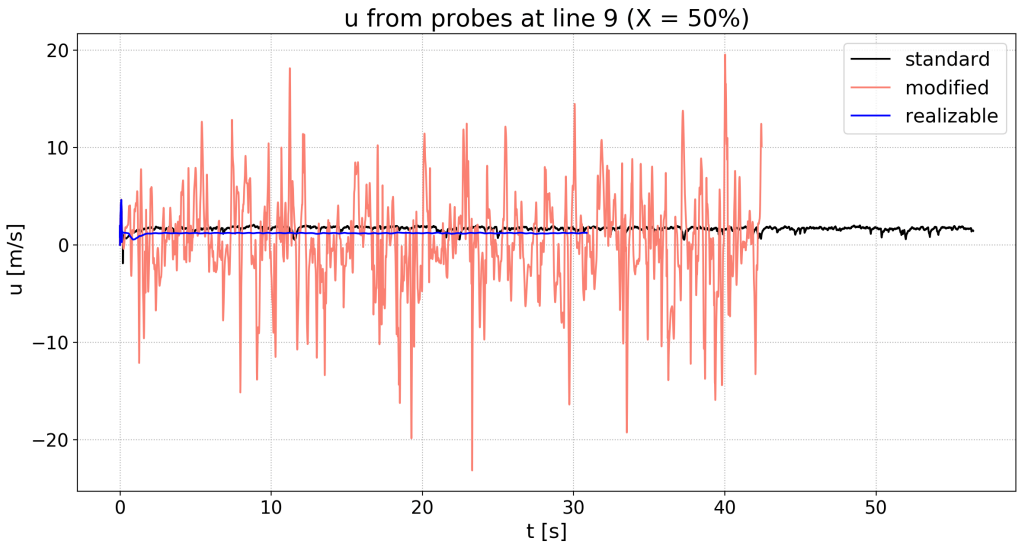

Figure 6.22 – u velocity at probe line 9 for standard, modified and realizable URANS $k - \varepsilon$.

It is visible that the modified model presents fluctuations around an average value, similar to instantaneous behaviors of a LES simulation, which requires a high level of mesh refinement for assertive results. This might be attributed to a low consideration of turbulent viscosity, which plays a role in damping fluctuations (see figure 6.24). The mean and standard deviation of u velocity for lines 2 and 9 are presented in the table (6.3).

Table 6.3 – Mean and standard deviation of the velocity u

	Line 2		Line 9	
	Mean [m/s]	Std [m/s]	Mean [m/s]	Std [m/s]
Standard	-19.29	2.32	1.66	0.21
Modified	-15.97	7.97	-0.044	5.06
Realizable	-10.82	2.69	1.20	0.026

For line 2, when compared to the standard model, the mean values differ 17.21% for the modified model and 43.9% for the realizable model. When it comes to line 9, the differences are reduced when comparing the standard and realizable. For both lines, the standard deviations of the modified model were much higher in relation to the other models.

Also, it could be stated after 20s of simulation that the mean values do not vary expressively for all closure models, being chosen as a starting point for mean velocity analysis in some

regions of the domain. About the computational cost for the simulation to reach 20 seconds, URANS standard model took 29.79 hours, while the modified and realizable took 23.62h and 24.99h, respectively.

An analysis of the specific turbulent kinetic energy was realized, obtained from the balance equations, visible in the figure (6.23). From the figure, it is seen that the specific turbulent kinetic energy at line 2 for the realizable model is higher than the other two, while for line 9, the situation inverts, with a higher value for the standard model. The modified model presented values close to zero for both cases, which implies that the model presents an instantaneous behavior and the modeled part of k is insignificant, being necessary to calculate the turbulent kinetic energy from the velocity field fluctuations. With a non-relevant modeled part of k, the turbulent viscosity also tends to zero, avoiding the damping of instabilities.

Considering URANS statistics, a more complete approach would be to consider data from the balance equations and the velocity field, even if it is known that the most part of the spectra is modeled. Taking the modified model as an example, it presents an LES-like behavior, in which the largest structures containing the most part of the energy in the spectra are calculated, while modeling the rest. This could happen due to a low μ_t considered in its calculations, which plays a role in damping instabilities. Therefore, if instabilities are not dampered and knowing that $\mu_t = C_\mu \frac{k^2}{\varepsilon}, C_\mu = 0.09$, the modeled k has low values, while the k provided by velocity field fluctuations is higher, thus, being necessary the analysis of both calculus.

The table (6.4) represents the total turbulent kinetic energy from the modeled and calculated part. Therefore, using this approach, the k values of the Standard and Modified tend to be closer, while the Realizable provided a much higher value.

Table 6.4 – Values for the modeled and calculated part of k

	k (modeled)	k (vel. field)	k total
Standard	50.409	8.012	58.421
Modified	1.212	62.738	63.95
Realizable	127.956	5.537	133.49

The figure (6.24) illustrates the turbulent viscosity from a probe at line 2 and its results

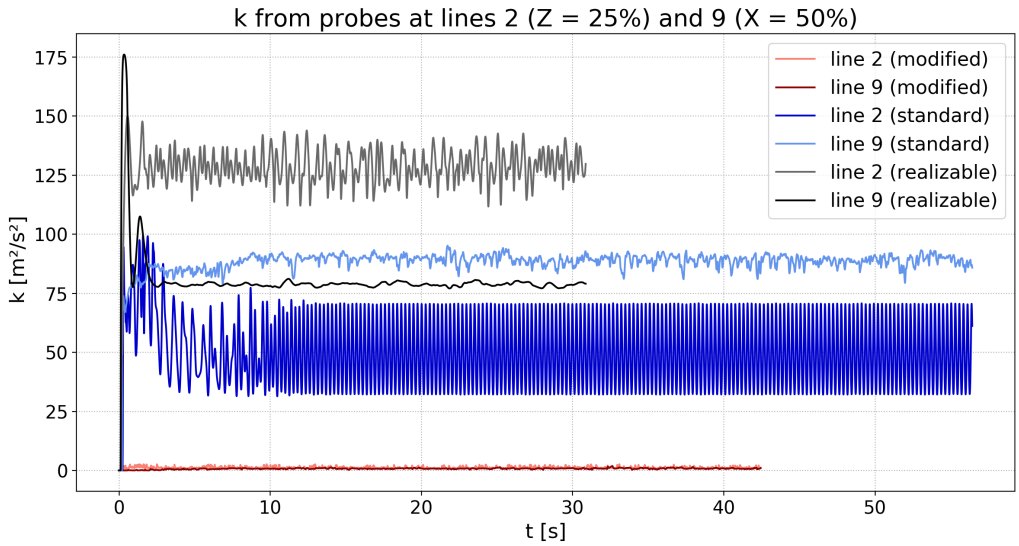

Figure 6.23 – Turbulent kinetic energy at probe lines 2 and 9 for standard, modified and realizable URANS $k - \varepsilon$.

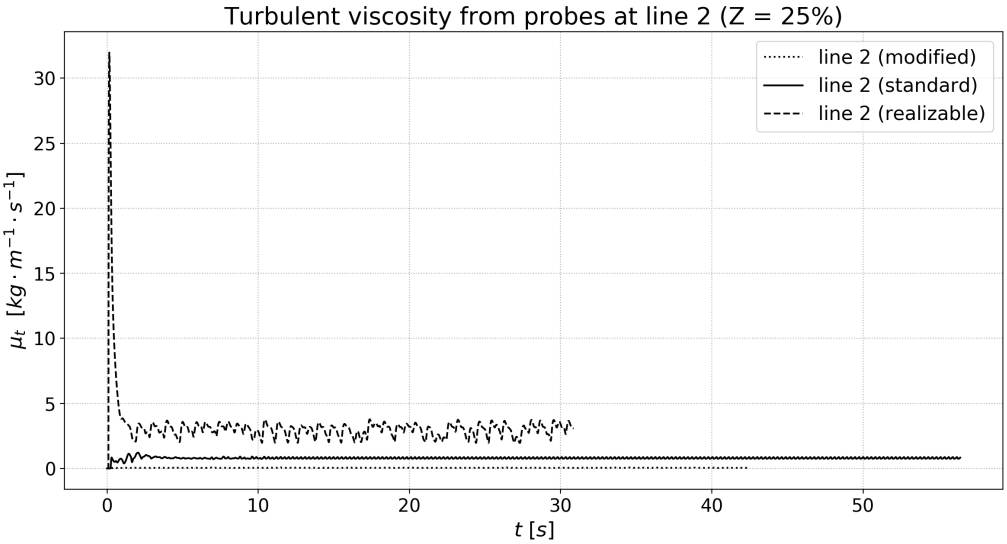

Figure 6.24 – Turbulent viscosity at probe line 2 for standard, modified and realizable URANS $k - \varepsilon$.

corroborates with the discussion concerning the turbulent kinetic energy of the three URANS models analyzed.

When comparing the magnitude of velocities at a slice where Y = 20%, the figure (6.25) demonstrates that both modified and realizable models present the formation of a swirling effect, but with different intensities. It is visible that, for the realizable, the inlet velocities are quickly

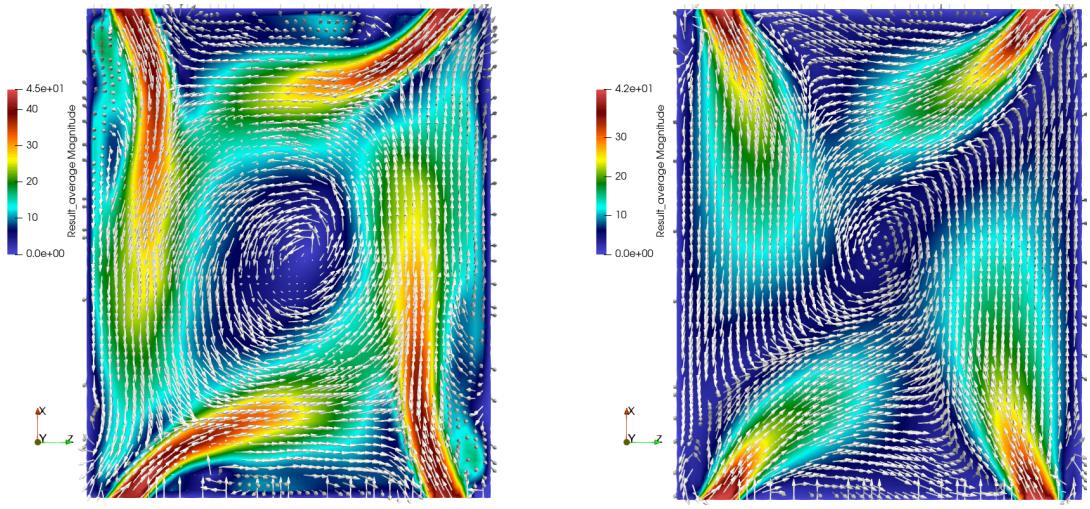

(a) Modified (b) Realizable

Figure 6.25 – Magnitude of velocities u,v and w [m/s] at Y= 20% for URANS modified and realizable simulations.

reduced towards the center, which may imply a reduced rotation velocity when compared to the modified and standard models.

At the same vertical location (Y = 20%), the axial and tangential velocities were analyzed from the probes at line 1, comparing URANS standard, modified, and realizable models (figure (6.26)). In relation to the axial velocity, the curves of standard and modified models present the same tendency, but with lower velocity values for the latter. The realizable model differs in value and curve shape from the other two models and does not present higher velocity values close to the walls as the others. The tangential velocity illustrates the same tendency for all 3 models, but different values when approaching the velocity peaks of the real vortex, with close values between standard and modified models and reduced values for the realizable, reflecting the low swirling intensity as discussed for the figure (6.25).

At Y = 50%, the figure (6.27) illustrates the swirling behavior when the fluid passes through the compression generated by the *nose* structure. While the modified model presents a result similar to LES and standard simulations, in which the swirl is visible with a lower magnitude velocity at the center, the realizable presents a large amount of fluid with unified velocity values in a large region, but without evidencing a central low-velocity region that would take place in a swirling flow. Also, higher velocity values are present in the modified result.

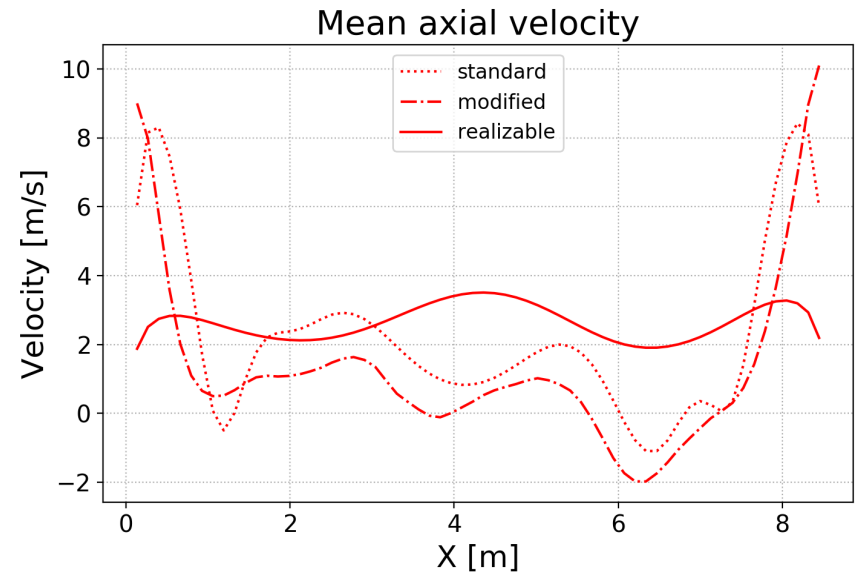

(a) Axial velocity (v)

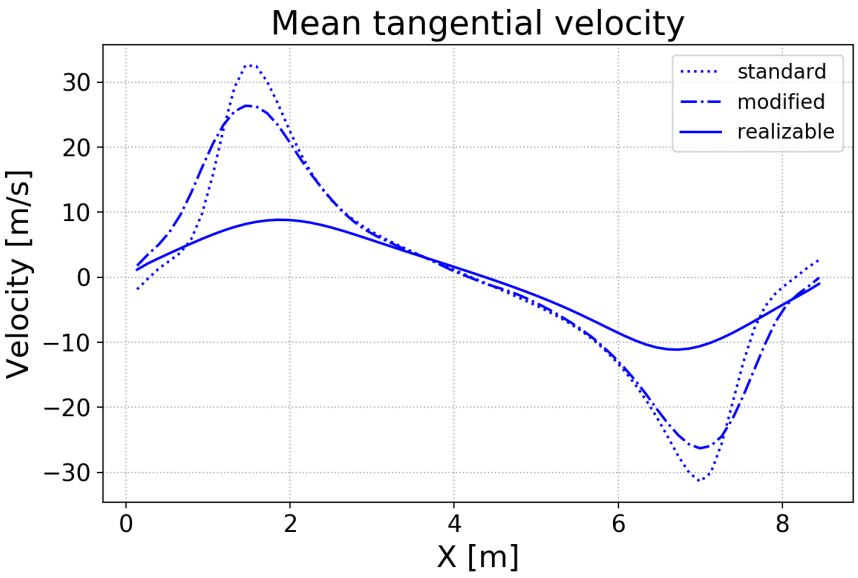

(b) Tangential velocity (w)

Figure 6.26 – Mean axial and tangential velocities at line 1 for URANS standard, modified and realizable.

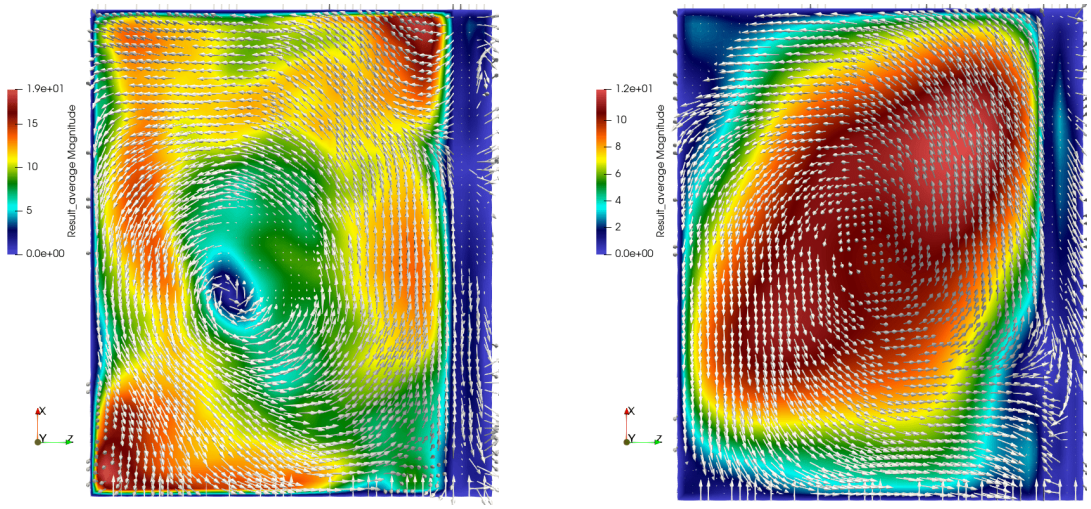

(a) Modified (b) Realizable

Figure 6.27 – Magnitude of velocities u,v and w [m/s] at Y= 50% for URANS modified and realizable simulations.

The axial and tangential velocities along line 5 are plotted in the figure (6.28). From the axial results, it is visible the discrepancy of the realizable behavior in comparison to the others, as it presents higher velocity values at the center of the swirl. The tangential result shows a similar behavior of the fluid for all 3 models, with opposite velocity directions following the rotational sense and a tendency of a solid-body rotation profile, but with distant values when comparing the realizable model to the others.

Following the exit of the domain, the figure (6.29) illustrates the magnitude of the velocity field at a slice where Y = 80%.

From this figure, the modified results still present a velocity distribution similar to LES and standard URANS, while the realizable result indicates a more equally distributed velocity to the exit between the structures that compose the superheater, which is a reflection of the lower swirling intensity present in the top region of the domain.

The axial velocity at the probe at line 9, close to the exit, figure (6.30), indicates values close to zero for the standard model, inferring that the vectors are aligned and normal to the exit surface. The realizable model shows some oscillating and positive values and the modified, negative ones, indicating descendant vectors. Concerning the w velocity, the waves on the graph indicate the interference of the superheater on the velocity field. The oscillation is similar for all

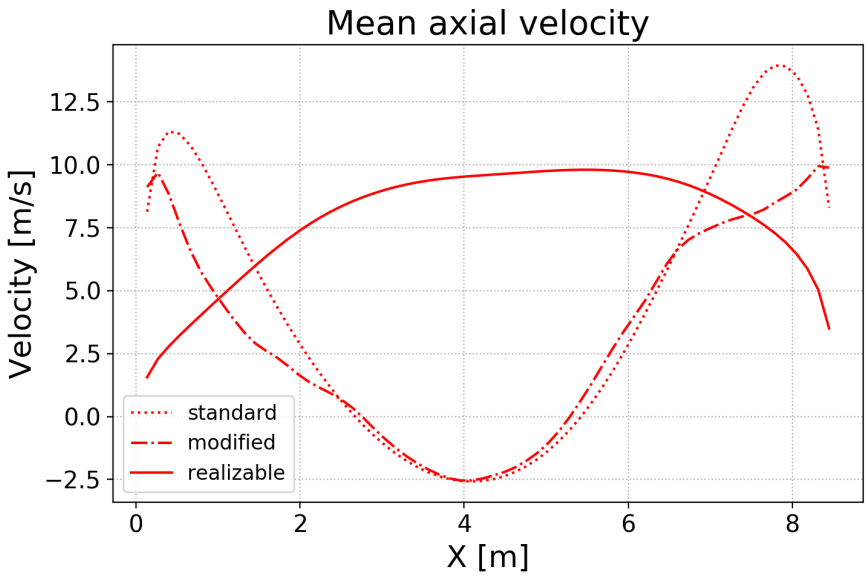

(a) Axial velocity (v)

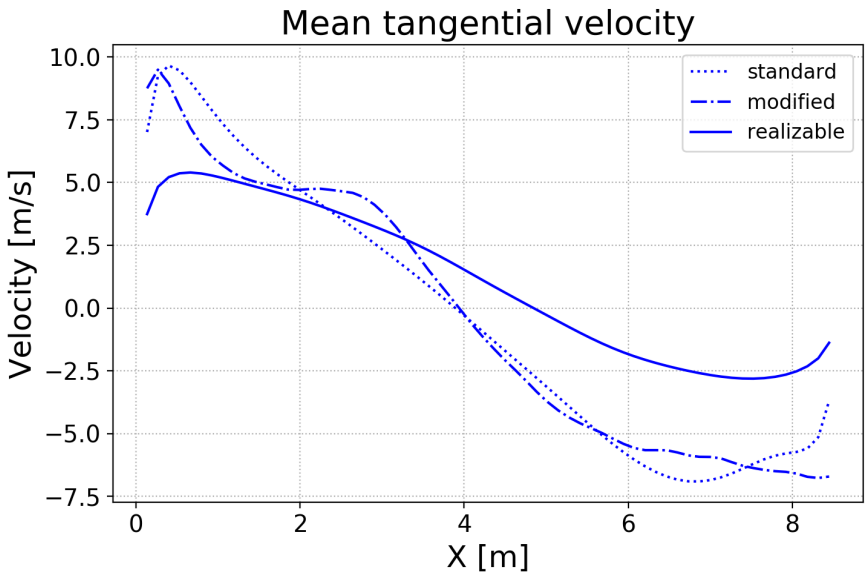

(b) Tangential velocity (w)

Figure 6.28 – Mean axial and tangential velocities at line 5 for URANS standard, modified and realizable.

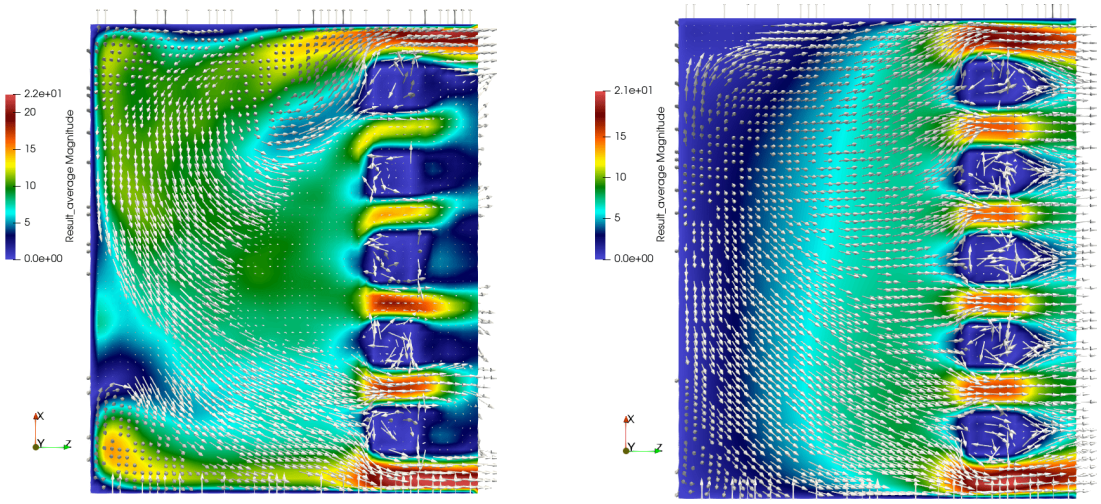

(a) Modified

(b) Realizable

Figure 6.29 – Magnitude of velocities u,v and w [m/s] at Y= 80% for URANS modified and realizable simulations.

3 models, but the standard one presents a smaller variation of the values.

This section had the objective of presenting some differences concerning the URANS standard, modified and realizable $k - \varepsilon$ models applied to a turbulent swirling flow simulation inside a conceptual CO boiler. It has been shown that the modified model presented an instantaneous velocity field similar to LES behavior and its results were similar to those from standard URANS, including the swirl effect. The realizable results did not illustrate a swirling behavior, due to the fact that the mean velocity graphs presented relevant differences in relation to the other models and higher values at the center of the swirl, which is not consistent with the tendency of a reversed flow. Therefore, even though the URANS standard closure model implemented in MFSim code had similar results compared to the modified, it was chosen as the model to be used in the non-reactive simulation with different chemical species in the following section.

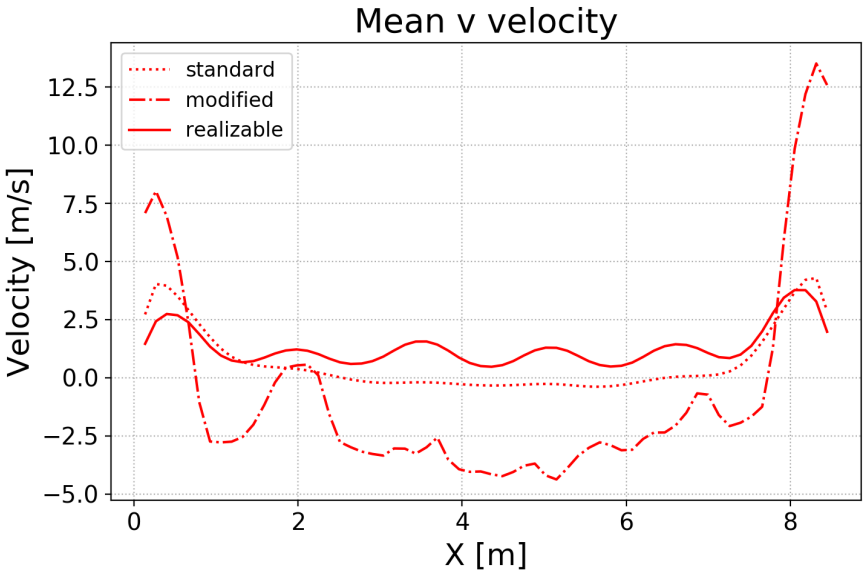

(a) Axial velocity (v)

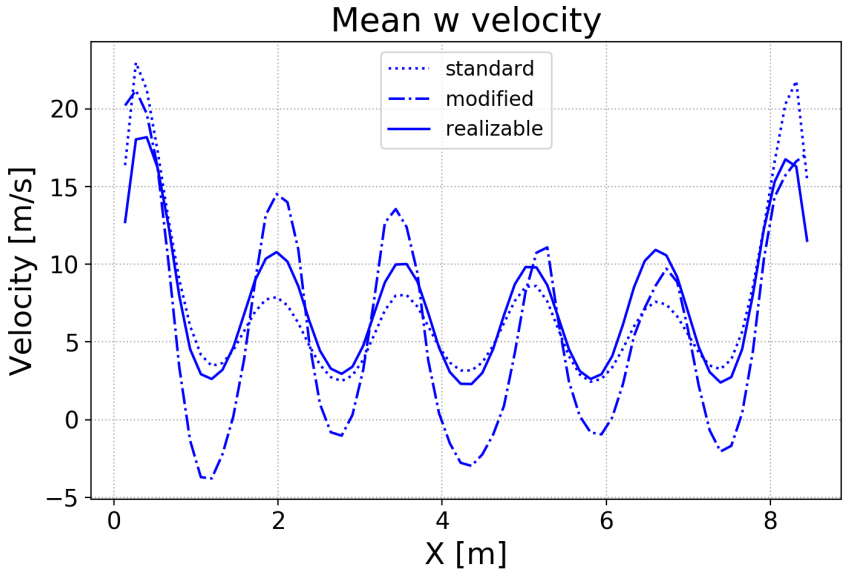

(b) Tangential velocity (w)

Figure 6.30 – Mean axial and tangential velocities at line 9 for URANS standard, modified and realizable.

6.3 Multi-component simulation using URANS standard k-ε

This section has the objective of presenting the influence that different chemical species may bring on to the already known URANS standard $k-\varepsilon$ simulation inside a conceptual CO boiler. Knowing that there will be no reaction among the substances and the temperature inside the domain is considered constant of value $T = 923\ K$, it is expected a possible influence of the diversity of diffusivity and density of each species on the overall flow kinematics.

For the inlet flow conditions, the figure (6.31) illustrates the main jet and coflow zones, in red and light blue, respectively, of a specific inlet region of the domain. The main jet is composed of a mixture of CO gas, O_2, N_2, CO_2 and H_2O, while the coflow is air (O_2 and N_2). The table (6.5) indicates the substances and their respective mass fractions for each jet composition. The density of the main jet is $0.376197\ kg/m^3$, while the density of the coflow is $0.380923\ kg/m^3$.

Figure 6.31 – Main jet (red) and coflow inlets (light blue) on the surface on plane Y-Z.

Table 6.5 – Mass fraction for each substance present in the main jet and coflow.

Jet	O_2	N_2	CO	CO_2	H_2O
Main Jet	0.003	0.693	0.097	0.143	0.064
Coflow	0.233	0.767	—	—	—

The inlet conditions from previous simulations, such as velocities and angles, mesh grid, boundary conditions, among others, are maintained.

In order to compare the results of this simulation in relation to a standard URANS $k - \varepsilon$ simulation without chemical species, it was analyzed, at first, the velocity u (X-direction) in relation to time from probes at lines 2 and 9, to find out the time required for achieving a statistically steady-state, figure (6.32).

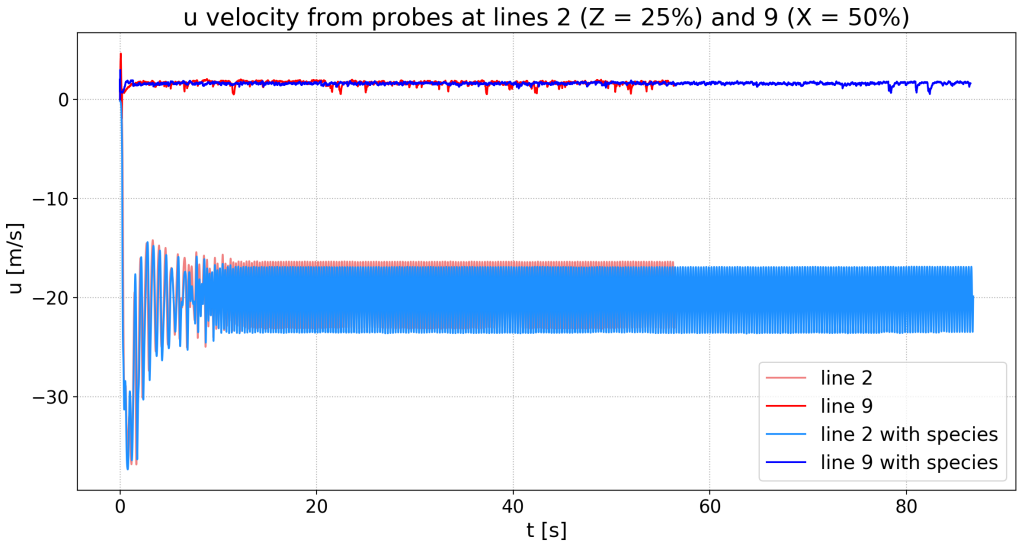

Figure 6.32 – Comparison of u velocity in relation to time for URANS $k - \varepsilon$ with and without multiple species.

From the figure, it can be seen that the data is close for both situations and the oscillations are stable, with a constant average after 15 seconds of simulation. For accuracy, the data considered for average analysis is chosen after 20 seconds of simulation.

In relation to the velocity field behavior, the figures (6.33, 6.34, 6.35) demonstrate that there is no significant difference of axial (v) and tangential (w) velocities when URANS $k - \varepsilon$ standard with and without species are compared. This fact may be explained by the irrelevant difference of densities involved.

The density of the fluid of the simulation without different species was constant, with a value of $0.3823 kg/m^3$. The simulation with species had no significant difference of density between the main jet and the coflow, with respective values of $0.376197 kg/m^3$ and $0.380923 kg/m^3$.

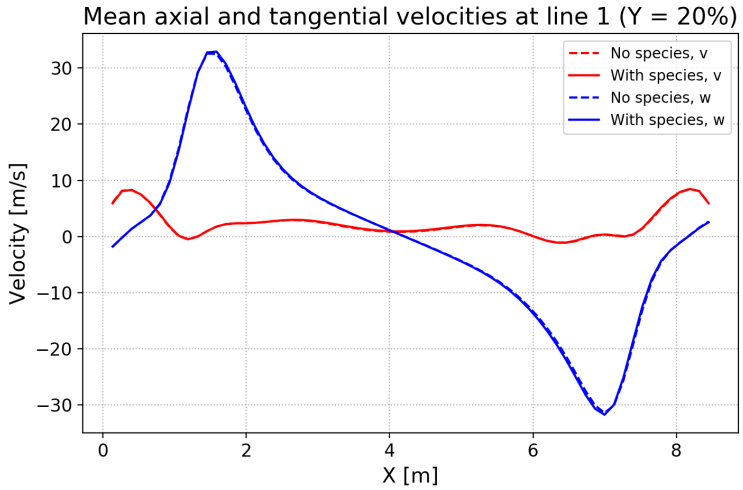

Figure 6.33 – Comparison of mean axial (v) and tangential (w) velocities in relation to time for URANS $k - \varepsilon$ with and without multiple species at line 1 (Y = 20%).

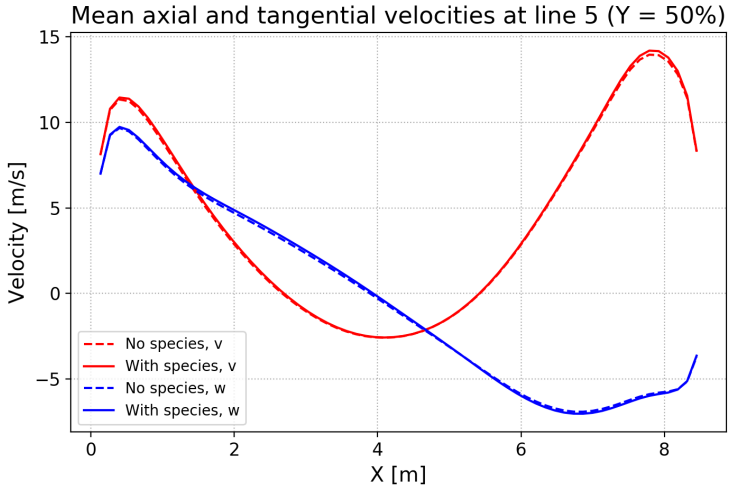

Figure 6.34 – Comparison of mean axial (v) and tangential (w) velocities in relation to time for URANS $k - \varepsilon$ with and without multiple species at line 5 (Y = 50%).

The figure (6.36) illustrates the density field and highlights that the maximum and minimum values of the domain are close. Regions in blue contrasting with the rest of the domain, represent the main jet, which has a lower density value.

Concerning the mass fractions of some species of interest, like CO and O_2, their distribution over the domain, after 20s of simulation, can be illustrated by the figures (6.37a) and (6.37b).

Knowing that coflow species were set as an initial condition all over the domain, the

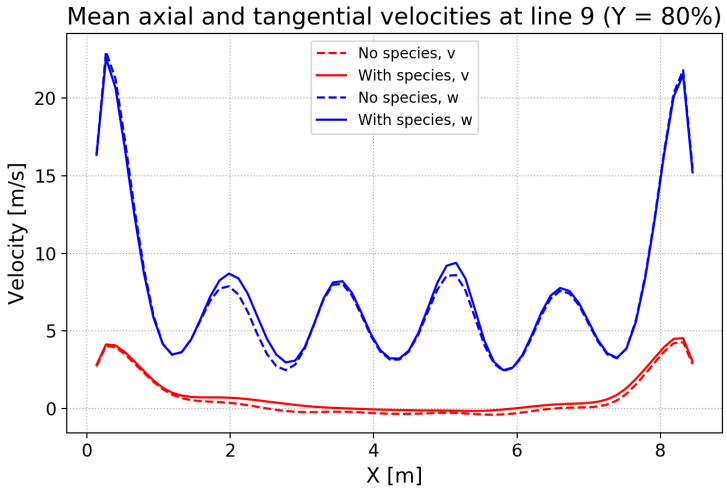

Figure 6.35 – Comparison of mean axial (v) and tangential (w) velocities in relation to time for URANS $k - \varepsilon$ with and without multiple species at line 9 (Y = 80%).

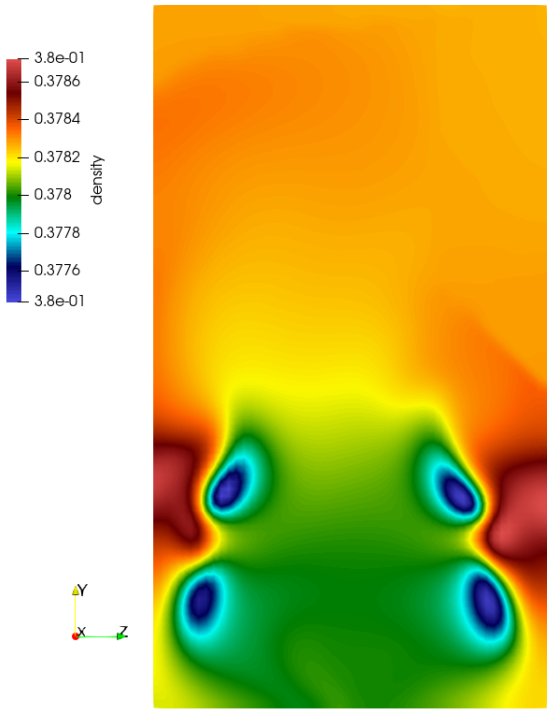

Figure 6.36 – Density field on the plane Y-Z where X = 50%.

contrast generated by the main jet is visible. The highest mass fractions of CO are present in red zones in figure (6.37a), where the main jet inlet is situated, whereas the outer zones in green and blue represent the domain occupied by the coflow jet and the initial conditions. In the center, a yellow zone still illustrates a strong presence of CO, but also indicates its mass fraction decay due to the start of the mixing process with other substances present in the coflow. Advancing

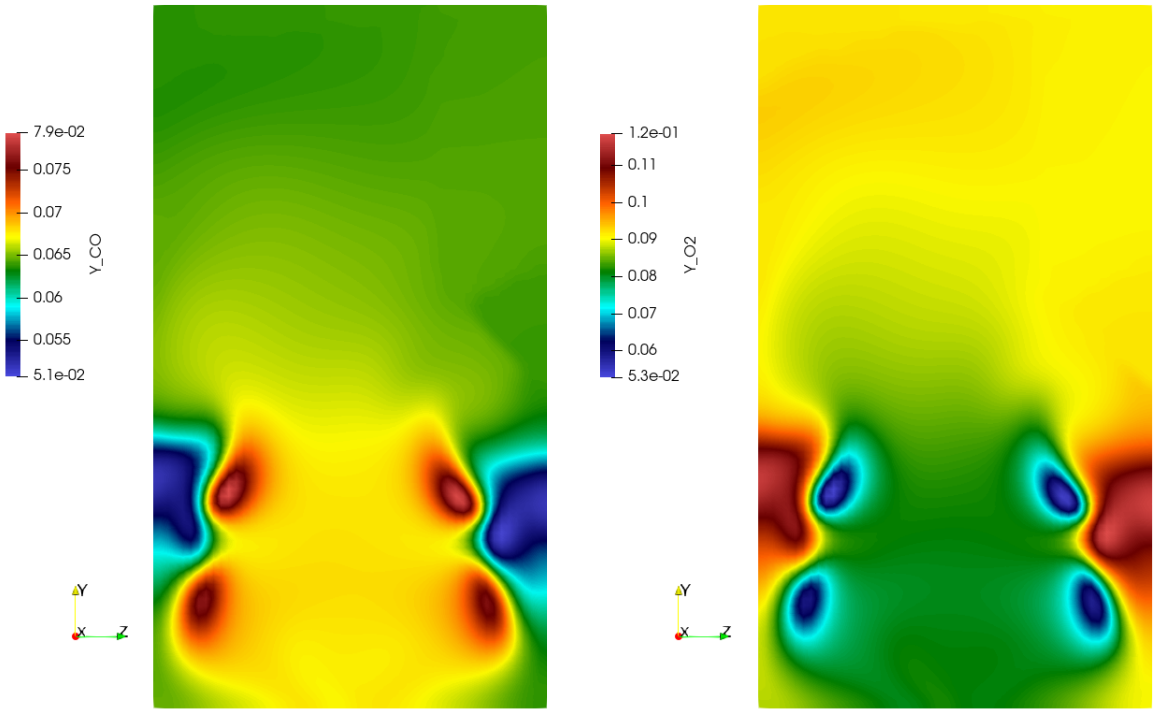

(a) CO (b) O_2

Figure 6.37 – Mass fractions fields of CO and O_2 at a domain slice at X = 50% on the plane Y-Z.

vertically, the CO mass fraction field turns to green, at around $Y_{CO} = 0.065$, which means that its mass fraction achieved a certain mixture level of convergence.

As the mass fraction of O_2 present in the main jet is 0.003 and in the coflow is 0.233, it is expected that lower values should be present in the main jet zone, figure (6.37b). The swirl zone in green represents the region with the highest mixture level, justifying the low mass fraction of O_2 after some time of simulation. The red zones are spots where the mixing effect of the swirl is not effective. Out of the highest mixing influence, there is still a mixing phenomenon represented by the yellow region, but less intense.

The figure (6.38) indicates the mixing process in relation to time for the probes at lines 2 and 9. It took approximately 10s for the mass fractions oscillations to stabilize and it can be seen that the domain was initialized with a certain amount of O_2, but its mass fraction decreased rapidly after the insertion of the main jet, composed initially by a CO mass fraction of 0.097. The mass fraction values for both substances approximate, indicating a mixing process and a certain amount of O_2 is maintained due to its higher mass fraction and coflow influence.

When comparing lines 2 and 9, it is remarkable that the substances at line 9 took longer to achieve a stable behavior, since they are situated close to the outlet and the mixing fluid would demand more time, related to the residence time, to flow through the outlet. Also, it is interesting to notice that the mass fraction values for O_2 are 12.79% higher close to the outlet, while the CO values are 5.19% smaller, representing that CO tends to remain in a higher amount at the lower region of the boiler.

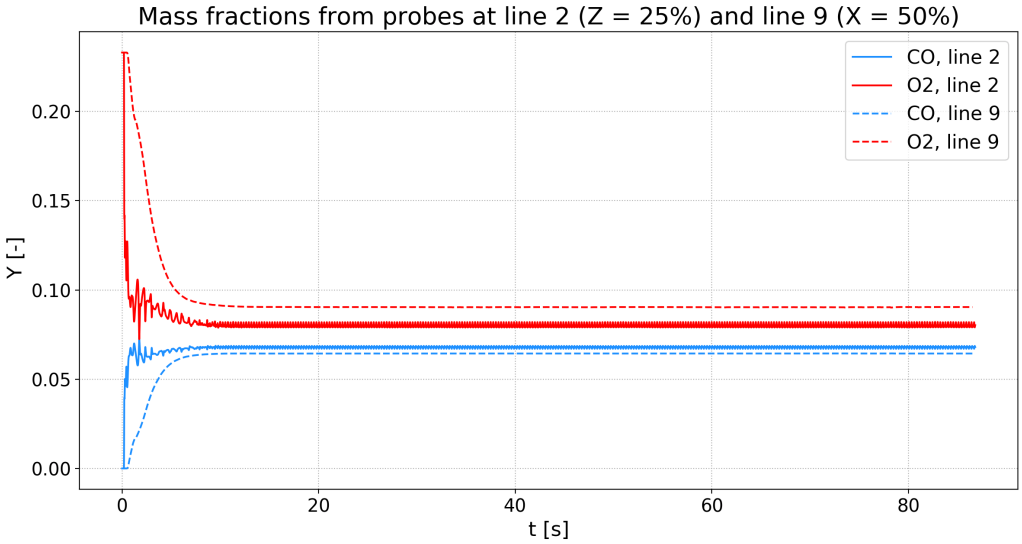

Figure 6.38 – Temporal variations of the mass fractions of CO and O_2 at lines 2 and 9.

The figure (6.39) illustrates the average mass fraction values of CO and O_2 along the line 1, where Y = 20%. As seen in figure (6.38), the mass fraction values of O_2 are always higher than CO. Also, there are peaks concerning the red line that would represent a region composed of coflow substances that do not suffer a mixing influence coming from the main jet. Therefore, one could say that this region is out of the main influence of the swirling flow. The opposite behavior can be seen for CO, which presents valleys in the regions out of the swirling influence. The mass fraction values tend to approximate close to the center region of the boiler.

Along line 9, figure (6.40), the variations of the mass fraction values for each substance are irrelevant, maintaining the behavior of higher values for O_2.

Therefore, it can be concluded that this specific setup of different species in a non-reactive URANS $k - \varepsilon$ simulation did not affect the velocity field, since there are no relevant differences

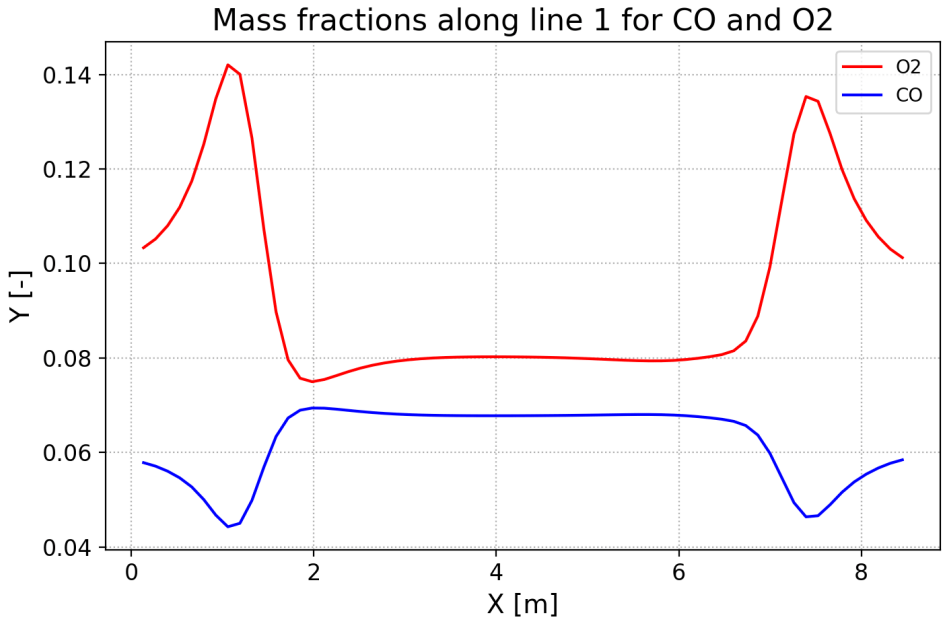

Figure 6.39 – Average mass fractions of CO and O_2 along line 1.

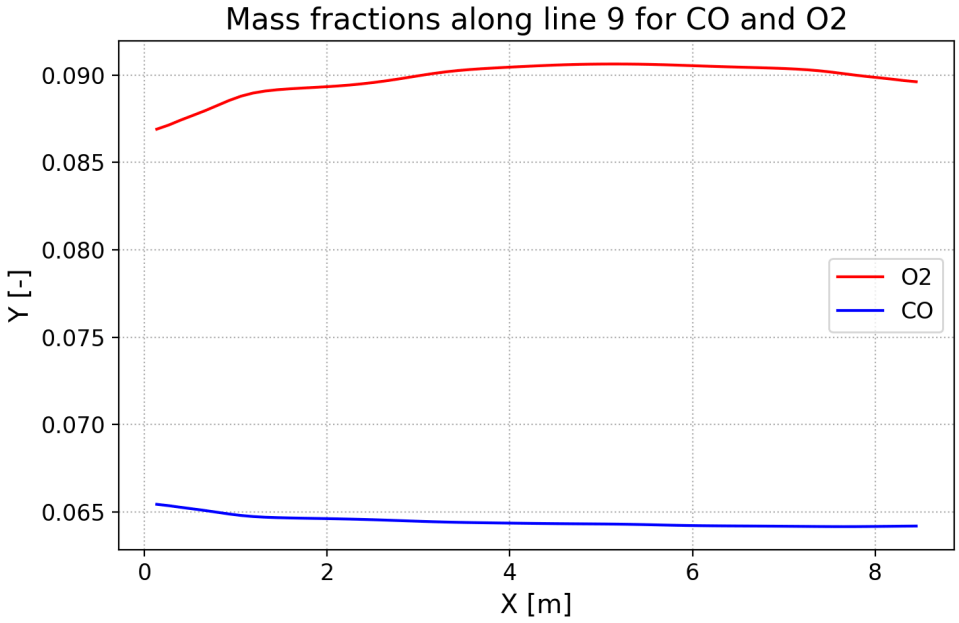

Figure 6.40 – Average mass fractions of CO and O_2 along line 9.

of density. Besides that, it has been pointed out that the region with the stronger mixing influence between the main jet and the coflow is within the swirl close to the inlet region's level. The mass fractions of substances present in the main jet and the coflow are rapidly mixed and their values tend to approximate at around 10s.

Chapter 7

CONCLUSION

This research study had the aim of investigating a non-reactive turbulent flow inside a cyclonic industrial boiler used in refineries. The application of a CO boiler in a petrochemical refinery concerns the burning of residual CO flue gas to reduce pollutant gas emissions and to use the available energy in this gas through combustion to generate superheated steam by a superheater present in the boiler structure.

Knowing that almost 80% of the energy matrix in Brazil is generated by processes involving combustion (MME, 2020) and that government regulations about NO_x emissions are becoming more and more restrict, the research about efficiency improvement of combustion processes inside a CO boiler is an engineering and environmental challenge that must be considered for studying.

In order to provide more efficient combustion processes to reduce NO_x emissions in a CO boiler, a turbulent swirling flow generated by tangential fluid inlets inside the CO boiler was proposed, based on the fact that a turbulent swirling flow enhances the mixing process (PETERS, 2010) and reduces the working temperature, which hampers the NO_x thermal formation.

Therefore, a computational fluid dynamics simulation of a non-reactive turbulent swirling flow in a simplified CO boiler structure was proposed in order to understand the swirling formation, the fluid behavior in different locations inside the domain and the distribution of some chemical species , such as CO and O_2. Besides, a diversity of turbulent closure models, such as

LES, URANS standard $k-\varepsilon$, modified $k-\varepsilon$ and realizable $k-\varepsilon$ were used, providing some data about required simulation time and velocity field variation depending on the applied model.

To provide a theoretical basis, a study of turbulence, its characteristics and LES and URANS mathematical modelling was proposed. Also, a study about turbulent mixing and swirling flows was realized. Some authors found promising results for turbulent mixing simulations applying the LES approach (WEGNER; HUAI; SADIKI, 2004; DIMOTAKIS, 2005). Also, the velocity field of a mixing simulation using URANS could be well predicted (IVANOVA; NOLL; AIGNER, 2010).

For swirling flows, the URANS $k-\varepsilon$ model presented a tendency for demonstrating a premature solid-body rotation due to its eddy viscosity assumption, causing overestimation of turbulent stresses (CHEN; LIN, 1999; GROTJANS, 1999). Reynolds Stress Models, otherwise, could present improved performance (YOUNIS; GATSKI; SPEZIALE, 1996; CHEN; LIN, 1999; GROTJANS, 1999; LU; SEMIÃO, 2003). LES also provided accurate solutions (MARE; JONES; MENZIES, 2004; ORBAY et al., 2013) and better predictions when compared to other URANS models (ĆOĆIĆ et al., 2013; ILIE, 2018). When comparing URANS standard $k-\varepsilon$ to other URANS models, some works presented better predictions for the first (ĆOĆIĆ et al., 2013; JAVADI; NILSSON, 2015; RAHMAN; ASRAR; KHAN, 2019).

Concerning swirling effects, some studies pointed out that swirling flows can reduce pollutant emissions, particularly of nitrogen oxides, by improving mixing of reactants and, therefore, decreasing flame temperature (SCHMITTEL et al., 2000; COGHE; SOLERO; SCRIBANO, 2004; BURGUETTE; COSTA, 2006; COZZI; COGHE, 2012; MERLO et al., 2013; BOUSHAKI et al., 2017).

For the proposed simulation, a mathematical modeling was presented, addressing equations for LES methodology using Smagorinsky approach, URANS $k-\varepsilon$ models, such as standard, modified and realizable, besides of mass conservation of chemical species.

Also, to solve the system of equations proposed, a numerical modeling was prepared, discussing about advective and diffusive discretization schemes, such as *CUBISTA* (Converged and Universally Bounded Interpolation Scheme for Treatment of Advection) *CDS* (*Central*

Differences Scheme), respectively. The temporal discretization discussed was the *SBDF* (Semi-Implicit Backward Differentiation Formula) and for pressure-velocity coupling, the Fractional Step method. Since there are geometries represented by lagrangian mesh inside the eulerian domain, the Immersed Boundary Method using Multi Direct Forcing had to be presented.

To illustrate the efficiency of the in-house MFSim code to simulate multi-component mixing flows, a simulation was presented and its results discussed. For the Immersed Boundary method, a work by Magalhães et al. (2019) illustrated some results capable of being obtained.

About simulation results, when comparing LES and URANS standard $k - \varepsilon$ with the same mesh refinement, the latter achieves a statistically steady regime earlier. Both models presented similar results about the velocity field, including the formation of a swirling flow phenomenon and the presence of a reverse flow at the core of the swirl. The influence of the *nose* and superheater structures in directing the flow to the outlet region was visible. A Rankine-type vortex could be visible at the lower vertical level of the domain, while a solid-body rotation with lower velocities seemed predominant next to the *nose* region.

When comparing URANS standard, modified and realizable $k - \varepsilon$ models, the realizable was the fastest model to achieve a statistically steady regime. A turbulent kinetic energy obtained from the balance equations illustrated that, at a lower level of the boiler, the realizable model had the highest values, while the modified present data close to zero. This could be visible as a case where URANS statistics would be incomplete without analysing the turbulent kinetic energy from velocity field fluctuations, since the modified presented an LES-like behavior, with large eddy structures being solved, while modeling the rest of the spectra. This was confirmed by a turbulent kinetic viscosity analysis, which illustrated a low value for the modified model, impacting in damping instabilites.

All 3 models presented a swirling behavior, with similar results between standard and modified models. The realizable illustrated a different and physically inconsistent behavior when its tangential velocity field at Y = 20% was more approximate to a solid-body rotation. Besides, the mean axial velocity did not present a reversed flow at the core of the swirl as the other two models do.

From the multi-component simulation, when adding different chemical species in the URANS standard $k - \varepsilon$ simulation, there was no relevant modification in the velocity field, stating that it was a passive mixing flow. Also, temporal and average mass fractions for CO and O_2 were illustrated, indicating that the highest mixing level was obtained in the region with the highest swirling behavior, where CO mass fractions could be increased in comparison to the rest of the domain and CO and O_2 mass fractions values were more approximate.

Therefore, the study of a non-reactive turbulent mixing flow in a cyclonic CO boiler is relevant to provide understanding of the distribution of mass fractions along the equipment to provide comprehension in mixture processes, species present in higher quantities and its locations, useful for planning a reactive process. Besides, velocity field analysis can assist in future studies about the residence time of certain compounds and the formation of rotating flow zones, relevant to the mixing process and chemical reactions. With this information, one can have more control over the temperatures resulting from the reactions and, consequently, over the thermal formation of NO_x. Then, for future works on this subject, simulations with a reactive configuration would be valuable to provide data about the influence of the combustion over the velocity field and the distribution of chemical species in the domain after chemical reactions, analyzing the thermal formation of NO_x and the temperatures involved. Besides that, it would be valuable to have a deeper study on the comparison between LES and URANS, since the first provided similar mean results in relation to URANS and fluctuations that are important to mixing analysis, even if the mesh used in both simulations was not refined enough for accurate results using LES. Also, the calculation of the swirl number and its impact on the mixing effect depending on its magnitude would be of great importance for the subject.

BIBLIOGRAPHY

ALVES, M.; OLIVEIRA, P.; PINHO, F. A convergent and universally bounded interpolation scheme for the treatment of advection. *International journal for numerical methods in fluids*, Wiley Online Library, v. 41, n. 1, p. 47–75, 2003. Cited 2 times on pages vii and 67.

ANDRADE, F. O. de. *Contribuição à Simulação das Grandes Escalas de uma Chama Turbulenta Pré-Misturada Estabilizada em um Escoamento a Alta Velocidade*. Thesis (PhD. Thesis) — PUC-RJ, 2009. Cited on page 5.

ARMFIELD, S. W.; FLETCHER, C. A. J. Comparison of $k - \varepsilon$ and algebraic reynolds stress models for swirling diffuser flow. *International Journal for Numerical Methods in Fluids*, v. 9, n. 8, p. 987–1009, 1989. Available in: <https://onlinelibrary.wiley.com/doi/abs/10.1002/fld.1650090807>. Cited 2 times on pages 55 and 105.

ASCHER, U. M.; RUUTH, S. J.; WETTON, B. T. Implicit-explicit methods for time-dependent partial differential equations. *SIAM Journal on Numerical Analysis*, SIAM, v. 32, n. 3, p. 797–823, 1995. Cited on page 67.

BALDWIN, B.; BARTH, T. A one-equation turbulence transport model for high reynolds number wall-bounded flows. In: *29th Aerospace Sciences Meeting*. [S.l.: s.n.], 1991. p. 610. Cited on page 20.

BALDWIN, B.; LOMAX, H. Thin-layer approximation and algebraic model for separated turbulent flows. In: *16th aerospace sciences meeting*. [S.l.: s.n.], 1978. p. 257. Cited on page 20.

BATCHELOR, G. Energy decay and self-preserving correlation functions in isotropic turbulence. *Quarterly of Applied Mathematics*, v. 6, n. 2, p. 97–116, 1948. Cited on page 14.

BEARMAN, P. W. On vortex shedding from a circular cylinder in the critical reynolds number regime. *Journal of Fluid Mechanics*, Cambridge University Press, v. 37, n. 3, p. 577–585, 1969. Cited 2 times on pages 84 and 85.

BOUSHAKI, T. Introductory chapter: Swirling flows and flames. In: BOUSHAKI, T. (Ed.). *Swirling Flows and Flames*. Rijeka: IntechOpen, 2019. cap. 1. Available in: <https://doi.org/10.5772/intechopen.86495>. Cited on page 27.

BOUSHAKI, T. et al. Study of pollutant emissions and dynamics of non-premixed turbulent oxygen enriched flames from a swirl burner. *Proceedings of the Combustion Institute*, Elsevier, v. 36, n. 3, p. 3959–3968, 2017. Cited 2 times on pages 38 and 123.

BOUSSINESQ, J. *Essai sur la théorie des eaux courantes*. [S.l.]: Impr. nationale, 1877. Cited 5 times on pages 11, 20, 41, 43, and 48.

BRADSHAW, P. Possible origin of prandt's mixing-length theory. *Nature*, Springer, v. 249, n. 5453, p. 135–136, 1974. Cited on page 50.

BURGERS, J. M. A mathematical model illustrating the theory of turbulence. In: *Advances in applied mechanics*. [S.l.]: Elsevier, 1948. v. 1, p. 171–199. Cited on page 14.

BURGUETTE, M.; COSTA, M. NOx emissions from unconfined swirl flames, NOx-emissionen aus unbegrenzten wirbelflammen. In: *INFUB, European Conference on Industrial Furnaces and Boilers, 7*. ;, 2006. p. 1–7. ISBN 972-99309-1-0. Available in: <https://www.tib.eu/de/suchen/id/tema%3ATEMA20070101768>. Cited 2 times on pages 38 and 123.

CHAPMAN, G. T.; TOBAK, M. Observations, theoretical ideas, and modeling of turbulent flows—past, present, and future. In: *Theoretical approaches to turbulence*. [S.l.]: Springer, 1985. p. 19–49. Cited 2 times on pages 15 and 16.

CHEN, J.; LIN, C. Computations of strongly swirling flows with second-moment closures. *International Journal for Numerical Methods in Fluids*, v. 30, n. 5, p. 493–508, 1999. Available in: <https://onlinelibrary.wiley.com/doi/abs/10.1002/%28SICI%291097-0363%2819990715%2930%3A5%3C493%3A%3AAID-FLD849%3E3.0.CO%3B2-3>. Cited 2 times on pages 32 and 123.

CHENG, B. Review of turbulent mixing models. *Acta Mathematica Scientia*, v. 29, n. 6, p. 1703 – 1720, 2009. Available in: <http://www.sciencedirect.com/science/article/pii/S0252960210600124>. Cited on page 23.

CHORIN, A. J. Numerical solution of the navier-stokes equations. *Mathematics of Computation*, American Mathematical Society, v. 22, n. 104, p. 745–762, 1968. ISSN 00255718, 10886842. Available in: <http://www.jstor.org/stable/2004575>. Cited on page 70.

CHOU, P. Y. On velocity correlations and the solutions of the equations of turbulent fluctuation. *Quarterly of Applied Mathematics*, Brown University, v. 3, n. 1, p. 38–54, 1945. ISSN 0033569X, 15524485. Available in: <http://www.jstor.org/stable/43633490>. Cited 2 times on pages 21 and 50.

COGHE, A.; SOLERO, G.; SCRIBANO, G. Recirculation phenomena in a natural gas swirl combustor. *Experimental thermal and fluid science*, Elsevier, v. 28, n. 7, p. 709–714, 2004. Cited 2 times on pages 38 and 123.

COURANT, R.; FRIEDRICHS, K.; LEWY, H. On the partial difference equations of mathematical physics. *IBM journal of Research and Development*, IBM, v. 11, n. 2, p. 215–234, 1967. Cited on page 68.

COZZI, F.; COGHE, A. Effect of air staging on a coaxial swirled natural gas flame. *Experimental thermal and fluid science*, Elsevier, v. 43, p. 32–39, 2012. Cited 2 times on pages 38 and 123.

DAMASCENO, M. M. R. *Modelagem de Condições de Contorno para Escoamentos Turbulentos Utilizando Simulações das Grandes Escalas*. Thesis (Master's Thesis) — Federal University of Uberlândia, Uberlândia, Minas Gerais, Brazil, 2012. Cited 2 times on pages 15 and 57.

DAMASCENO, M. M. R. et al. *Desenvolvimento de uma modelagem para escoamentos reativos em malhas adaptativas do tipo bloco-estruturada*. Thesis (PhD. Thesis) — Universidade Federal de Uberlândia, 2018. Cited 4 times on pages vii, 63, 65, and 68.

DAVYDOV, B. On Statistical Dynamics of an Incompressible Turbulent Fluid. *Soviet Physics Doklady*, v. 6, p. 10, jul. 1961. Cited on page 50.

DEARDORFF, J. W. et al. A numerical study of three-dimensional turbulent channel flow at large reynolds numbers. *J. Fluid Mech*, v. 41, n. 2, p. 453–480, 1970. Cited on page 15.

DENNER, F. et al. Comparative study of mass-conserving interface capturing frameworks for two-phase flows with surface tension. *International Journal of Multiphase Flow*, Elsevier, v. 61, p. 37–47, 2014. Cited on page 61.

DIMOTAKIS, P. E. Turbulent mixing. *Annual Review of Fluid Mechanics*, v. 37, n. 1, p. 329–356, 2005. Available in: <https://doi.org/10.1146/annurev.fluid.36.050802.122015>. Cited 3 times on pages 24, 25, and 123.

DURBIN, P. On the $k - \varepsilon$ stagnation point anomaly. *International Journal of Heat and Fluid Flow*, v. 17, p. 89–90, 1996. Cited 2 times on pages 55 and 105.

ECKART, C. An analysis of the stirring and mixing processes in incompressible fluids. 1948. Cited on page 24.

ELIAS, A. J. *Modelagem híbrida URANS-LES para escoamentos turbulentos*. Thesis (Master's Thesis), 2018. Cited on page 12.

FAVRE, A. Statistical equations of turbulent gases. In: *Problems of hydrodynamics and continuum mechanics*. [S.l.: s.n.], 1969. Cited on page 59.

FERZIGER, J. H. Large eddy simulation: Its role in turbulence research. In: ____. *Theoretical Approaches to Turbulence*. New York, NY: Springer New York, 1985. p. 51–72. ISBN 978-1-4612-1092-4. Available in: <https://doi.org/10.1007/978-1-4612-1092-4_3>. Cited on page 15.

FERZIGER, R. C. J.; REYNOLDS, W. Evaluation of subgrid-scale models using an accurately simulated turbulent ow. *J. Fluid Mech*, v. 91, p. 1–16, 1979. Cited on page 46.

FREIRE, A. Turbulência e seu desenvolvimento histórico. *III Escola de Primavera de Transição & Turbulência*, p. 23–27, 2002. Cited on page 12.

FRIC, T. F. Skewed shear-layer mixing within a duct. *AIAA Journal*, v. 34, n. 4, p. 847–849, 1996. Available in: <https://doi.org/10.2514/3.13150>. Cited on page 26.

GASCHE, J. L.; BARBI, F.; VILLAR, M. M. An efficient immersed boundary method for solving the unsteady flow through actual geometries of reed valves. 2012. Cited on page 61.

GASKELL, P.; LAU, A. Curvature-compensated convective transport: Smart, a new boundedness-preserving transport algorithm. *International Journal for numerical methods in fluids*, Wiley Online Library, v. 8, n. 6, p. 617–641, 1988. Cited on page 66.

GERMANO, M. A proposal for a redefinition of the turbulent stresses in the filtered navier–stokes equations. *The Physics of fluids*, American Institute of Physics, v. 29, n. 7, p. 2323–2324, 1986. Cited 3 times on pages 22, 46, and 56.

GONçALVES, V. H. P.; MAGALHãES, G. M.; VEDOVOTO, J. M. Urans simulation of turbulent non-premixed and non-reacting propane jet flow. *12th Spring School on Transition and Turbulence*, 2020. Cited on page 60.

GROTJANS, H. Application of higher order turbulence models to cyclone flows. *VDI BERICHTE*, VDI VERLAG GMBH, v. 1511, p. 175–182, 1999. Cited 5 times on pages 3, 33, 100, 101, and 123.

GUALTIERI, C. et al. On the values for the turbulent schmidt number in environmental flows. *Fluids*, Multidisciplinary Digital Publishing Institute, v. 2, n. 2, p. 17, 2017. Cited on page 60.

GUPTA, A.; LILLEY, D.; SYRED, N. *Swirl flows*. [S.l.: s.n.], 1984. Cited 4 times on pages vii, 27, 28, and 29.

HARLOW, F.; NAKAYAMA, P. I. Transport of turbulence energy decay rate. In: . [S.l.: s.n.], 1968. Cited on page 50.

HEISENBERG, W. On the theory of statistical and isotropic turbulence. *Proceedings of the Royal Society of London. Series A. Mathematical and Physical Sciences*, The Royal Society London, v. 195, n. 1042, p. 402–406, 1948. Cited on page 14.

HERNANDEZ, B. et al. Computational fluid dynamics (cfd) modeling of swirling flows in industrial counter-current spray-drying towers under fouling conditions. *Industrial & Engineering Chemistry Research*, ACS Publications, v. 57, n. 35, p. 11988–12002, 2018. Cited on page 32.

HOFFMANN, P. D. A. C.; HOFFMANN, A. C.; STEIN, L. E. *Gas cyclones and swirl tubes*. [S.l.]: Springer, 2002. Cited 2 times on pages vii and 30.

HÖGSTRÖM, U. Review of some basic characteristics of the atmospheric surface layer. *Boundary-Layer Meteorology*, Springer, v. 78, n. 3-4, p. 215–246, 1996. Cited on page 15.

ILIE, M. Numerical studies of turbulent swirling reacting flows using les and urans. *International Journal of Thermal Sciences*, Elsevier, v. 134, p. 89–100, 2018. Cited 2 times on pages 35 and 123.

IVANOVA, E. M.; NOLL, B. E.; AIGNER, M. Computational Modeling of Turbulent Mixing of a Transverse Jet. *Journal of Engineering for Gas Turbines and Power*, v. 133, n. 2, 10 2010. Available in: <https://doi.org/10.1115/1.4002015>. Cited 3 times on pages 26, 27, and 123.

JAVADI, A.; NILSSON, H. Time-accurate numerical simulations of swirling flow with rotor-stator interaction. *Flow, Turbulence and Combustion*, Springer, v. 95, n. 4, p. 755–774, 2015. Cited 2 times on pages 34 and 123.

JOHNSON, B.; ROBACK, R. Mass and momentum turbulent transport experiments with confined swirling coaxial jets. i. In: *20th Joint Propulsion Conference*. [S.l.: s.n.], 1983. p. 1380. Cited on page 35.

JONES, L. N. *Modelling of turbulent swirling flows*. Thesis (PhD. Thesis) — University of Leeds, December 2004. Available in: <http://etheses.whiterose.ac.uk/1192/>. Cited 3 times on pages vii, 30, and 31.

JONES, W.; LAUNDER, B. The prediction of laminarization with a two-equation model of turbulence. *International Journal of Heat and Mass Transfer*, v. 15, n. 2, p. 301 – 314, 1972. ISSN 0017-9310. Available in: <http://www.sciencedirect.com/science/article/pii/0017931072900762>. Cited on page 21.

KADU, P. A. et al. Numerical investigation of passive scalar transport and mixing in a turbulent unconfined coaxial swirling jet. *International Journal of Heat and Mass Transfer*, v. 142, p. 118461, 2019. ISSN 0017-9310. Available in: <http://www.sciencedirect.com/science/article/pii/S0017931019311585>. Cited on page 35.

KARMAN, T. V. Progress in the statistical theory of turbulence. *Proceedings of the National Academy of Sciences of the United States of America*, National Academy of Sciences, v. 34, n. 11, p. 530, 1948. Cited on page 14.

KAYA, F.; KARAGOZ, I. Performance analysis of numerical schemes in highly swirling turbulent flows in cyclones. *Current Science*, Temporary Publisher, v. 94, n. 10, p. 1273–1278, 2008. ISSN 00113891. Available in: <http://www.jstor.org/stable/24100235>. Cited 2 times on pages 55 and 105.

KOLMOGOROV, A. N. Equations of turbulent motion in an incompressible fluid. *Dokl. Akad. Nauk SSSR*, v. 30, n. 4, p. 299–303, 1941. Available in: <http://cds.cern.ch/record/739754>. Cited 2 times on pages 21 and 50.

KOLMOGOROV, A. N. The local structure of turbulence in incompressible viscous fluid for very large reynolds numbers. *Cr Acad. Sci. URSS*, v. 30, p. 301–305, 1941. Cited 2 times on pages 13 and 40.

KOLMOGOROV, A. N. On degeneration (decay) of isotropic turbulence in an incompressible viscous liquid. In: *Dokl. Akad. Nauk SSSR*. [S.l.: s.n.], 1941. v. 31, p. 538–540. Cited on page 13.

KRISHNA, M. *Investigation of Swirl Flows Applied to the Oil and Gas Industry*. Thesis (Master's Thesis), 2009. Cited on page 30.

LANDAU, L.; LIFSHITZ, E. *Hydrodynamics by Fluid Mechanics*. [S.l.]: Pergamon Press, Burlington, MA, 1987. Cited on page 25.

LAUNDER, B.; SHARMA, B. Application of the energy-dissipation model of turbulence to the calculation of flow near a spinning disc. *Letters in Heat and Mass Transfer*, v. 1, n. 2, p. 131 – 137, 1974. ISSN 0094-4548. Available in: <http://www.sciencedirect.com/science/article/pii/0094454874901507>. Cited on page 21.

LAUNDER, B. E.; REECE, G. J.; RODI, W. Progress in the development of a reynolds-stress turbulence closure. *Journal of fluid mechanics*, Cambridge University Press, v. 68, n. 3, p. 537–566, 1975. Cited on page 15.

LAUNDER, B. E.; SPALDING, D. B. *Mathematical models of turbulence*. [S.l.]: Academic press, 1972. Cited 2 times on pages 15 and 51.

LEFEBVRE, A. H. The Role of Fuel Preparation in Low-Emission Combustion. *Journal of Engineering for Gas Turbines and Power*, v. 117, n. 4, p. 617–654, 10 1995. ISSN 0742-4795. Available in: <https://doi.org/10.1115/1.2815449>. Cited 3 times on pages vii, 36, and 37.

LEIBOVICH, S. The structure of vortex breakdown. *Annual review of fluid mechanics*, Annual Reviews 4139 El Camino Way, PO Box 10139, Palo Alto, CA 94303-0139, USA, v. 10, n. 1, p. 221–246, 1978. Cited on page 31.

LEONARD, A. et al. Energy cascade in large-eddy simulations of turbulent fluid flows. *Adv. Geophys. A*, v. 18, n. A, p. 237–248, 1974. Cited on page 45.

LEONARD, B. The ultimate conservative difference scheme applied to unsteady one-dimensional advection. *Computer methods in applied mechanics and engineering*, North-Holland, v. 88, n. 1, p. 17–74, 1991. Cited on page 66.

LESIEUR, M.; METAIS, O. New trends in large-eddy simulations of turbulence. *Annual Review of Fluid Mechanics*, v. 28, n. 1, p. 45–82, 1996. Available in: <https://doi.org/10.1146/annurev.fl.28.010196.000401>. Cited 2 times on pages 15 and 25.

LILLY, D. K. A proposed modification of the germano subgrid-scale closure method. *Physics of Fluids A: Fluid Dynamics*, v. 4, n. 3, p. 633–635, 1992. Available in: <https://doi.org/10.1063/1.858280>. Cited on page 22.

LILLY, K. The representation of small-scale turbulence in numerical simulation experiments. In: . [S.l.: s.n.], 1966. Cited on page 57.

LIMA, R. C.; NOGUEIRA, M. F.; GUERRA, D. R. Cfd modeling of a small-scale cyclonic combustor chamber using biomass powder. *Energy Procedia*, Elsevier, v. 120, p. 556–563, 2017. Cited on page 7.

LINDNER, G.; MARKUS, D.; MODEL, R. Non-reactive free jet flow: Comparison of simulations using different turbulence models with reference measurements. In: *Proc. 5th Europ. Conf. on Comp. Fluid Dynamics*. [S.l.: s.n.], 2010. Cited on page 3.

LORENZ, E. N. Deterministic nonperiodic flow. *Journal of the atmospheric sciences*, v. 20, n. 2, p. 130–141, 1963. Cited on page 16.

LU, P.; SEMIÃO, V. A new second-moment closure approach for turbulent swirling confined flows. *International journal for numerical methods in fluids*, Wiley Online Library, v. 41, n. 2, p. 133–150, 2003. Cited 2 times on pages 32 and 123.

MAGALHÃES, G. M. *Soluções contınuas e discretas de escoamentos cisalhantes livres em regimes laminar e turbulento*. Thesis (Master's Thesis), 2018. Cited 3 times on pages 51, 104, and 105.

MAGALHãES, G. et al. Computational simulation of a plane channel with $k-\varepsilon$ and multi-direct forcing method. In: . [S.l.: s.n.], 2019. Cited 4 times on pages viii, 82, 84, and 124.

MARE, F. D.; JONES, W.; MENZIES, K. Large eddy simulation of a model gas turbine combustor. *Combustion and Flame*, Elsevier, v. 137, n. 3, p. 278–294, 2004. Cited 2 times on pages 33 and 123.

MELO, R. et al. Simulation of thermal transfer using the immersed boundary method and adaptive mesh. In: BEGEL HOUSE INC. *THMT-18. Turbulence Heat and Mass Transfer 9 Proceedings of the Ninth International Symposium On Turbulence Heat and Mass Transfer*. [S.l.], 2018. Cited on page 61.

MENEVEAU, C.; KATZ, J. Scale-invariance and turbulence models for large-eddy simulation. *Annual Review of Fluid Mechanics*, Annual Reviews 4139 El Camino Way, PO Box 10139, Palo Alto, CA 94303-0139, USA, v. 32, n. 1, p. 1–32, 2000. Cited on page 15.

MENTER, F. R. Two-equation eddy-viscosity turbulence models for engineering applications. *AIAA journal*, v. 32, n. 8, p. 1598–1605, 1994. Cited on page 21.

MERLO, N. et al. Experimental study of oxygen enrichment effects on turbulent non-premixed swirling flames. *Energy & fuels*, ACS Publications, v. 27, n. 10, p. 6191–6197, 2013. Cited 2 times on pages 38 and 123.

MI, J.; NOBES, D. S.; NATHAN, G. J. Influence of jet exit conditions on the passive scalar field of an axisymmetric free jet. *Journal of Fluid Mechanics*, Cambridge University Press, v. 432, p. 91–125, 2001. Cited on page 27.

MME, M. de Minas e E. *Linha do Tempo de Indicadores de Energia, Emissões, Demografia e Economia - 1960 a 2019*. [S.l.: s.n.], 2020. Cited 3 times on pages vii, 2, and 122.

MOHAMMADI, B.; PIRONNEAU, O. Analysis of the k-epsilon turbulence model. 1993. Cited on page 51.

MURTHY, S. *Turbulent mixing in nonreactive and reactive flows*. [S.l.]: Springer Science & Business Media, 2013. Cited on page 3.

NAVIER, C. Mémoire sur les lois du mouvement des fluides. *Mémoires de l'Académie Royale des Sciences de l'Institut de France*, v. 6, n. 1823, p. 389–440, 1823. Cited on page 11.

NETO, A. S. et al. A numerical investigation of the coherent vortices in turbulence behind a backward-facing step. *Journal of Fluid Mechanics*, Cambridge University Press, v. 256, p. 1–25, 1993. Cited on page 56.

NETO, H. R. et al. Influence of seabed proximity on the vibration responses of a pipeline accounting for fluid-structure interaction. *Mechanical Systems and Signal Processing*, Elsevier, v. 114, p. 224–238, 2019. Cited on page 61.

NÓBREGA, R. C. da. *Catalisadores para o processo de craqueamento catalítico fluido de petróleo*. Monography (TCC) — Universidade Federal de Alfenas, 2014. Cited on page 5.

ORBAY, R. et al. Swirling turbulent flows in a combustion chamber with and without heat release. *Fuel*, Elsevier, v. 104, p. 133–146, 2013. Cited 2 times on pages 34 and 123.

ORSZAG, S. A.; PATTERSON, G. Numerical simulation of turbulence. In: *Statistical models and Turbulence*. [S.l.]: Springer, 1972. p. 127–147. Cited on page 15.

PAYRI, R. et al. Effect of turbulent model closure and type of inlet boundary condition on a large eddy simulation of a non-reacting jet with co-flow stream. *International Journal of Heat and Fluid Flow*, Elsevier, v. 61, p. 545–552, 2016. Cited on page 76.

PETERS, N. *Turbulent combustion*. [S.l.]: IOP Publishing, 2001. Cited on page 76.

PETERS, N. Combustion theory. *CEFRC Summer school, Princeton, June 28th–July 2nd*, 2010. Cited 2 times on pages 7 and 122.

POINSOT, T.; VEYNANTE, D. *Theoretical and numerical combustion*. [S.l.]: RT Edwards, Inc., 2005. Cited 3 times on pages 58, 59, and 60.

POPE, S. An explanation of the turbulent round-jet/plane-jet anomaly. *AIAA journal*, v. 16, n. 3, p. 279–281, 1978. Cited on page 81.

PRANDTL, L. Über flüssigkeitsbewegung bei sehr kleiner reibung, verhandlungen des dritten internationalen mathematiker-kongresses. Heidelberg, 1904. Cited on page 12.

PRANDTL, L. Bemerkungen zur theorie der freien turbulenz . *ZAMM - Journal of Applied Mathematics and Mechanics / Zeitschrift für Angewandte Mathematik und Mechanik*, v. 22, n. 5, p. 241–243, 1942. Available in: <https://onlinelibrary.wiley.com/doi/abs/10.1002/zamm.19420220502>. Cited on page 50.

PRANDTL, L. Uber ein neues formalsystem fiir die ausgebildete turbulenz. *Nachrichten von der Akad. der Wissenschaft in Gottingen*, 1945. Cited 2 times on pages 20 and 50.

PULLIN, D. I. A vortex-based model for the subgrid flux of a passive scalar. *Physics of Fluids*, v. 12, n. 9, p. 2311–2319, 2000. Available in: <https://doi.org/10.1063/1.1287512>. Cited on page 25.

RAHMAN, T. M. R.; ASRAR, W.; KHAN, S. A. An investigation of rans simulations for swirl-stabilized isothermal turbulent flow in a gas turbine burner. *Akademia Baru*, 2019. Cited 2 times on pages 36 and 123.

REYNOLDS, O. An experimental investigation of the circumstances which determine whether the motion of water shall be direct or sinuous, and of the law of resistance in parallel channels. *Philosophical Transactions of the Royal society of London*, The Royal Society London, n. 174, p. 935–982, 1883. Cited on page 41.

REYNOLDS, O. On the dynamical theory of incompressible viscous fluids and the determination of the criterion. *PT*, 1895. Cited on page 12.

RICHARDS, J. R. *Control of Nitrogen Oxides Emissions*. [S.l.], 2000. Cited 2 times on pages 5 and 6.

ROTTA, J. Statistische theorie nichthomogener turbulenz. *Zeitschrift für Physik*, Springer, v. 129, n. 6, p. 547–572, 1951. Cited on page 21.

SALVO, R.; SOUZA, F.; MARTINS, D. Analysis of sub-grid modeling effects in the simulation of the single-phase turbulent flow in an industrial cyclone separator. *Revista de Engenharia Térmica*, v. 11, p. 44, 10 2018. Cited on page 57.

SAQR, K. M. et al. Numerical simulation of confined vortex flow using a modified k– turbulence model. *CFD letters*, v. 1, n. 2, 2009. Cited 2 times on pages 55 and 105.

SCHEFER, R. W. Data base for a turbulent, nonpremixed, nonreacting propane-jet flow. *Combustion Research Facility, Sandia National Laboratories, Livermore, CA*, 2001. Cited 2 times on pages 76 and 80.

SCHLICHTING, H.; KESTIN, J. *Boundary layer theory*. [S.l.]: Springer, 1961. v. 121. Cited on page 84.

SCHMITTEL, P. et al. Turbulent swirling flames: Experimental investigation of the flow field and formation of nitrogen oxide. *Proceedings of the Combustion Institute*, v. 28, n. 1, p. 303 – 309, 2000. ISSN 1540-7489. Available in: <http://www.sciencedirect.com/science/article/pii/S0082078400802246>. Cited 2 times on pages 38 and 123.

SCHUBAUER, G. B.; SKRAMSTAD, H. K. Laminar boundary-layer oscillations and transition on. *Journal of research of the National Bureau of Standards*, The Bureau, v. 38, p. 251, 1947. Cited on page 15.

Shaanan, S.; Ferziger, J. H.; Reynolds, W. C. *Numerical simulation of turbulence in the presence of shear*. 1975. 30476 p. NASA STI/Recon Technical Report N. Cited on page 56.

SHIH, T.-H. et al. A new $k - \varepsilon$ eddy viscosity model for high reynolds number turbulent flows. *Computers Fluids*, v. 24, n. 3, p. 227 – 238, 1995. ISSN 0045-7930. Available in: <http://www.sciencedirect.com/science/article/pii/004579309400032T>. Cited on page 21.

SHIH, T.-H.; ZHU, J.; LUMLEY, J. L. A new reynolds stress algebraic equation model. *Computer Methods in Applied Mechanics and Engineering*, v. 125, n. 1, p. 287 – 302, 1995. ISSN 0045-7825. Available in: <http://www.sciencedirect.com/science/article/pii/0045782595007964>. Cited 3 times on pages 53, 54, and 105.

SINHA, N. *Towards RANS Parameterization of Vertical Mixing by Langmuir Turbulence in Shallow Coastal Shelves*. Thesis (PhD. Thesis), 11 2013. Cited 2 times on pages vii and 14.

SMAGORINSKY, J. General circulation experiments with the primitive equations: I. the basic experiment. *Monthly weather review*, v. 91, n. 3, p. 99–164, 1963. Cited 3 times on pages 21, 44, and 57.

SMITH, A.; CEBECI, T. *Numerical solution of the turbulent-boundary-layer equations*. [S.l.], 1967. Cited on page 20.

SMITH, E. et al. Preliminary examination of a" round jet initial condition anomaly" for the k-ε turbulence model. In: *15th Australasian Fluid Mechanics Conference*. [S.l.: s.n.], 2004. p. 1–4. Cited on page 81.

SORRENTINO, G. et al. An experimental and numerical study of mild combustion in a cyclonic burner. *Energy Procedia*, v. 120, p. 649–656, 08 2017. Cited on page 34.

SORRENTINO, G. et al. Design and development of a lab-scale burner for mild/flameless combustion. *Chemical Engineering Transactions*, v. 43, 2015. Cited 2 times on pages 100 and 101.

SORRENTINO, G. et al. Distributed combustion in a cyclonic burner. In: AIP PUBLISHING LLC. *AIP Conference Proceedings*. [S.l.], 2017. v. 1906, n. 1, p. 100002. Cited on page 7.

SPALART, P.; ALLMARAS, S. A one-equation turbulence model for aerodynamic flows. In: *30th aerospace sciences meeting and exhibit*. [S.l.: s.n.], 1992. p. 439. Cited on page 20.

SREENIVASAN, K. R. Turbulent mixing: A perspective. *Proceedings of the National Academy of Sciences*, National Academy of Sciences, v. 116, n. 37, p. 18175–18183, 2019. Available in: <https://www.pnas.org/content/116/37/18175>. Cited 3 times on pages vii, 22, and 23.

TAYLOR, G. I. Statistical theory of turbulence iv-diffusion in a turbulent air stream. *Proceedings of the Royal Society of London. Series A-Mathematical and Physical Sciences*, The Royal Society London, v. 151, n. 873, p. 465–478, 1935. Cited on page 13.

TENNEKES, H.; LUMLEY, J. L. *A first course in turbulence*. [S.l.]: MIT press, 2018. Cited on page 17.

TOWNSEND, A. The measurement of double and triple correlation derivatives in isotropic turbulence. In: CAMBRIDGE UNIVERSITY PRESS. *Mathematical Proceedings of the Cambridge Philosophical Society*. [S.l.], 1947. v. 43, n. 4, p. 560–570. Cited on page 14.

TURNS, S. R. et al. *Introduction to combustion*. [S.l.]: McGraw-Hill Companies, 1996. v. 287. Cited on page 4.

UHLMANN, M. An immersed boundary method with direct forcing for the simulation of particulate flows. *Journal of Computational Physics*, v. 209, n. 2, p. 448 – 476, 2005. ISSN 0021-9991. Available in: <http://www.sciencedirect.com/science/article/pii/S0021999105001385>. Cited on page 71.

VEDOVOTO, J. A. M.; SERFATY, R.; NETO, A. D. S. Mathematical and Numerical Modeling of Turbulent Flows. *Anais da Academia Brasileira de Ciências*, scielo, v. 87, p. 1195 – 1232, 06 2015. ISSN 0001-3765. Available in: <http://www.scielo.br/scielo.php?script=sci_arttext&pid=S0001-37652015000201195&nrm=iso>. Cited 3 times on pages 71, 73, and 74.

VILLAR, M. M. *Análise numérica detalhada de escoamentos multifásicos bidimensionais*. Thesis (PhD. Thesis) — Universidade Federal de Uberlândia, 2007. Available in: <https://repositorio.ufu.br/handle/123456789/14664>. Cited 2 times on pages 9 and 74.

VOELKL, T.; PULLIN, D. I.; CHAN, D. C. A physical-space version of the stretched-vortex subgrid-stress model for large-eddy simulation. *Physics of Fluids*, v. 12, n. 7, p. 1810–1825, 2000. Available in: <https://doi.org/10.1063/1.870429>. Cited on page 25.

WANG, P. *Large eddy simulation of turbulent swirling flows and turbulent premixed combustion*. Thesis (PhD. Thesis) — Lund University, 2005. Cited 2 times on pages 32 and 37.

WANG, Z.; FAN, J.; LUO, K. Combined multi-direct forcing and immersed boundary method for simulating flows with moving particles. *International Journal of Multiphase Flow*, v. 34, n. 3, p. 283 – 302, 2008. ISSN 0301-9322. Available in: <http://www.sciencedirect.com/science/article/pii/S0301932207001474>. Cited on page 71.

WARHAFT, Z. Passive scalars in turbulent flows. *Annual Review of Fluid Mechanics*, v. 32, n. 1, p. 203–240, 2000. Available in: <https://doi.org/10.1146/annurev.fluid.32.1.203>. Cited on page 25.

WEGNER, B.; HUAI, Y.; SADIKI, A. Comparative study of turbulent mixing in jet in cross-flow configurations using les. *International Journal of Heat and Fluid Flow*, v. 25, n. 5, p. 767 – 775, 2004. Selected papers from the 4th International Symposium on Turbulence Heat and Mass Transfer. Available in: <http://www.sciencedirect.com/science/article/pii/S0142727X04000931>. Cited 3 times on pages 25, 26, and 123.

WILCOX, D. *Turbulence Modeling for CFD*. DCW Industries, 2006. (Turbulence Modeling for CFD, v. 1). ISBN 9781928729082. Available in: <https://books.google.com.br/books?id=tFNNPgAACAAJ>. Cited 2 times on pages 20 and 21.

WILCOX, D. C. Reassessment of the scale-determining equation for advanced turbulence models. *AIAA journal*, v. 26, n. 11, p. 1299–1310, 1988. Cited on page 21.

WU, N.; BUSHE, W.; DAVY, M. On the experimental validation of combustion simulations in turbulent non-premixed jets. *Combustion Theory and Modelling*, Taylor & Francis, v. 14, n. 6, p. 855–874, 2010. Cited on page 75.

YARAS, M. I.; GROSVENOR, A. D. Evaluation of one and two equation low-re turbulence models. part i—axisymmetric separating and swirling flows. *International Journal for Numerical Methods in Fluids*, v. 42, n. 12, p. 1293–1319, 2003. Available in: <https://onlinelibrary.wiley.com/doi/abs/10.1002/fld.585>. Cited on page 32.

YEH, C.; LIANG, C. Nox reduction in a carbon monoxide boiler by reburning. *Procedia Engineering*, Elsevier, v. 67, p. 378–387, 2013. Cited on page 5.

YOUNIS, B. A.; GATSKI, T. B.; SPEZIALE, C. G. Assessment of the SSG Pressure-Strain Model in Free Turbulent Jets With and Without Swirl. *Journal of Fluids Engineering*, v. 118, n. 4, p. 800–809, 12 1996. Available in: <https://doi.org/10.1115/1.2835512>. Cited 2 times on pages 32 and 123.

ĆOĆIĆ, A. et al. Numerical simulation of turbulent swirling flows. *PAMM*, v. 13, n. 1, p. 309–310, 2013. Available in: <https://onlinelibrary.wiley.com/doi/abs/10.1002/pamm.201310150>. Cited 2 times on pages 34 and 123.